Politecnico di Torino

Collegio di Ingegneria Meccanica, Aereospaziale, dell'Auoveicolo e della produzione

Corso di Laurea Magistrale in Ingegneria Meccanica

Tesi di Laurea Magistrale

Numerical and experimental analysis of ageing mechanism in lithium ion cell

Relatore:
Aurelio Somà
Corelatore:
Francesco Mocera

Candidato:
Davide Clerici
250376

Sessione di Laurea Dicembre 2019

Contents

List of Figures

Abstract

Li-ion batteries are spreading really fast in the last decade since they are a clean energy source and could replace fossil fuels in the next decades. The major weakness of this technology lies on the energy density, reliability and safety.
In this thesis the ageing mechanisms and how the cell properties decay over time are studied.
In particular the attention is focused on the mechanical analysis of the cell: the source of the stresses which arises within the cell and their effect on the cell performance are studied.
The source of mechanical stresses are charge/discharge cycles and dynamic loads. The first source is well known and extensive works, mainly based on experimental approach, can be found in literature. On the contrary, few works in literature describe the effects of dynamic loads on the cell properties.
A mathematical model which describes the stresses in the particles of the active material is derived, for what concerns the electrical cycles. Moreover a numerical analysis with FE method was carried out in order to validate the mathematical model and to simulate more complex boundary conditions which could not be implemented in the analytical model.
Finally, a set of experimental tests were carried out in order to understand the effects of the dynamic load on the cell parameters. An increasing damage level, detected by capacity fade, is supposed to be recorded according to the classical fatigue laws.

Introduction

The aim of this thesis is to describe the ageing mechanisms which occur in lithium ion cells. Over the well known electrochemical mechanisms, this research is focused on the mechanical one, related mainly to charge/discharge cycles and vibration load.
In particular the effect of vibration loads on the cell performance is still an unknown field of research.
A mathematical model is established in order to describe the mechanical stresses which arise from charge/discharge cycles. Moreover a first model is established in order to describe the stress rate induced by dynamic loads.
Vibration loads are supposed to induce a progressive damage in the cell which could produce a reduction in electric properties. Several experimental tests were carried out to verify our assumption.

In the first chapter an introduction on li-ion batteries is presented, describing the causes of the increasing spread, the working principle, materials and configuration.

In the second chapter an overview on the results found in literature about the aging mechanism and the effects of mechanical load on li-ion batteries is presented.

In the third chapter the mathematical model which describes the stress rate induced by intercalation/deintercalation of lithium ion is present. Moreover a finite elements analysis is carried out in order to validate the analytical results derived by the model and to simulate a more realistic boundary conditions. Finally a numerical model which aims to describe the stresses which result form dynamic load is presented.

In the fourth chapter the experimental method is presented. Ideas, equipment and control system which allowed to perform proper experimental tests is presented. Finally the results from experimental tests are shown.

In the fifth chapter the conclusions reached at the end of the work are presented.

Chapter 1

State of the art

Lithium-ions batteries technology is spreading very fast in several different fields of application in the last few decades. As the technology spreads, also the research about this topic is becoming greatly extensive and detailed. Hence a deep research in the literature was carried out in order to frame properly this topic.
A presentation about generalities, working principle, materials, features and critical issues of lithium-ions batteries is reported in this section.

1.1 introduction

Internal combustion engine vehicles (ICE) cause a production of harmful gas and a large amount of carbon dioxide, which concurs in the increase of the global warming. The government of several states and the Europe union have announced a plan to reduce the production of ICE vehicles in few decades. For this reason, alternative energy sources are necessary to be investigated [1].
The most promising option is to entrust the power source to electric battery, so it is likely that petrol vehicles will be replaced by electric one (EV), which are characterized by zero-carbon emissions. In fact the use of EV rather than ICE transfer the production of harmful gases (GHG) from the city to the power plants, reducing the environmental pollution in the more critical areas. Moreover several researches [2] pointed out that EV reduce up to 20% in GHG (greenhouse gasses such as carbon anhydride, methane, and nitrous oxide, NOx) emission and further up to 40% if the electricity is generated by renewable resources [2,3].
For this reason EV and HEV are quickly spreading and the offer of electric vehicles is becoming even greater. Also the hybridization of heavy-duty vehicles is increasing and may replace diesel fuel in the next decades.

Nowadays different types of energy storage system are available, as shown in figure 1.1. Each of them have particular features which make them suitable for a specific application [3].

Researches on lithium-ion batteries started around 1970's, and the current concept was already established in 1976 by Whittingham. However this type of batteries were not commercialized until 1990's in electronic market, with some problems related to short lifetime and poor safety.

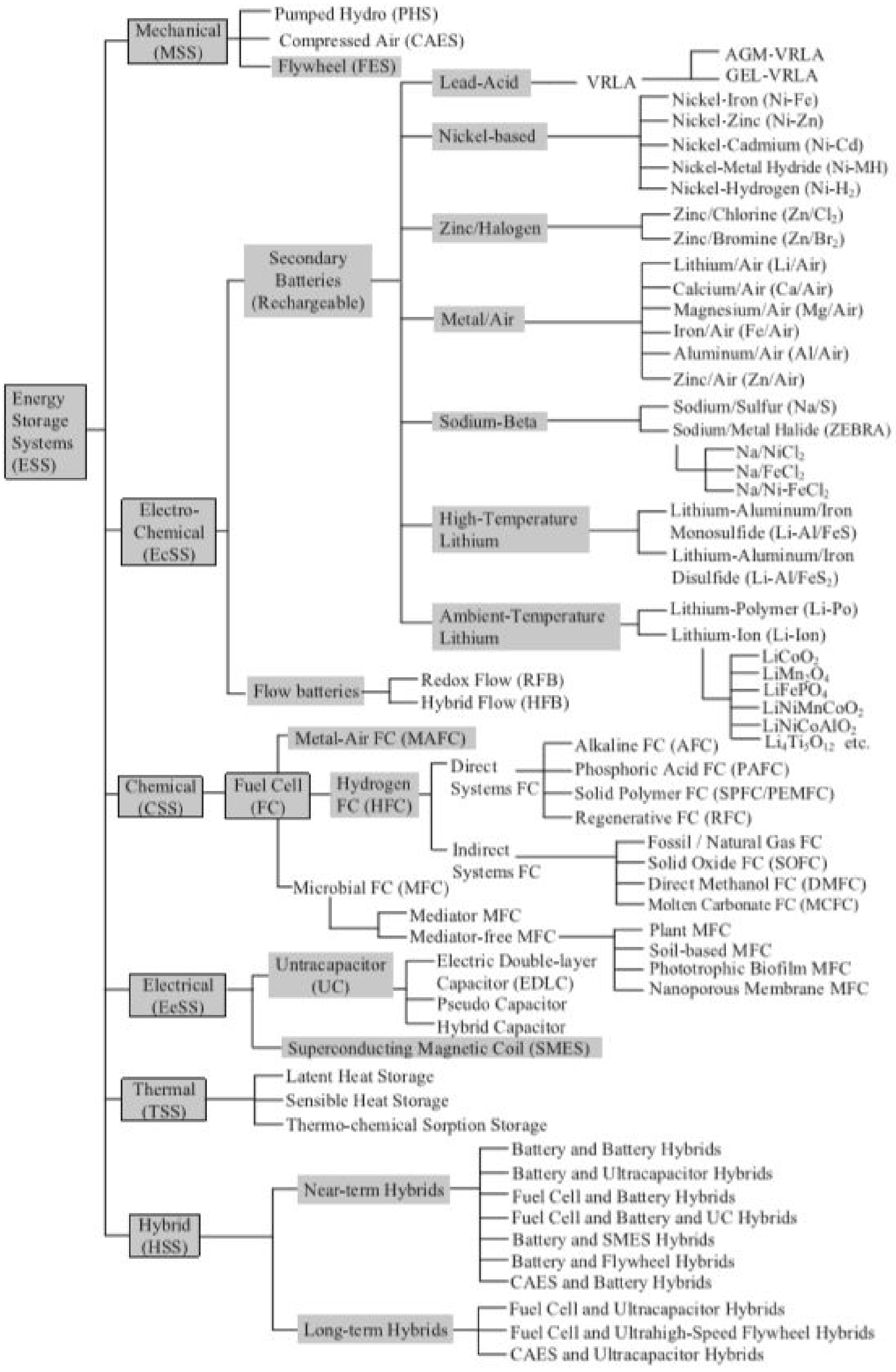

Figure 1.1: Energy storage system [3]

For what concerns EV, electrochemical batteries, such as Ni-Cd, Ni-Mh, lead

acid, lithium-ion, are the the most suitable energy storage system . In particular lithium-ion batteries, compared to the other ones, are featured by high energy density, high specific energy and power, and light weight. The power density of Li-ion batteries ranges from 500 to 2000 W/Kg. Moreover Li-ion batteries guarantee a long service life environmental friendliness, low self discharge and have lower harmful effects unlike mercury and lead batteries. [3]
The main disadvantage related to Li-ion battery is concerning their stability; in fact they need to work in a precise operating area, affected by charge rate, temperature and voltage range. Out of this area they are affected by a performance reduction and safety problems.

The so called Ragone plot in figure 1.2 relates the specific energy and the specific power for a set of different battery chemistry principle.

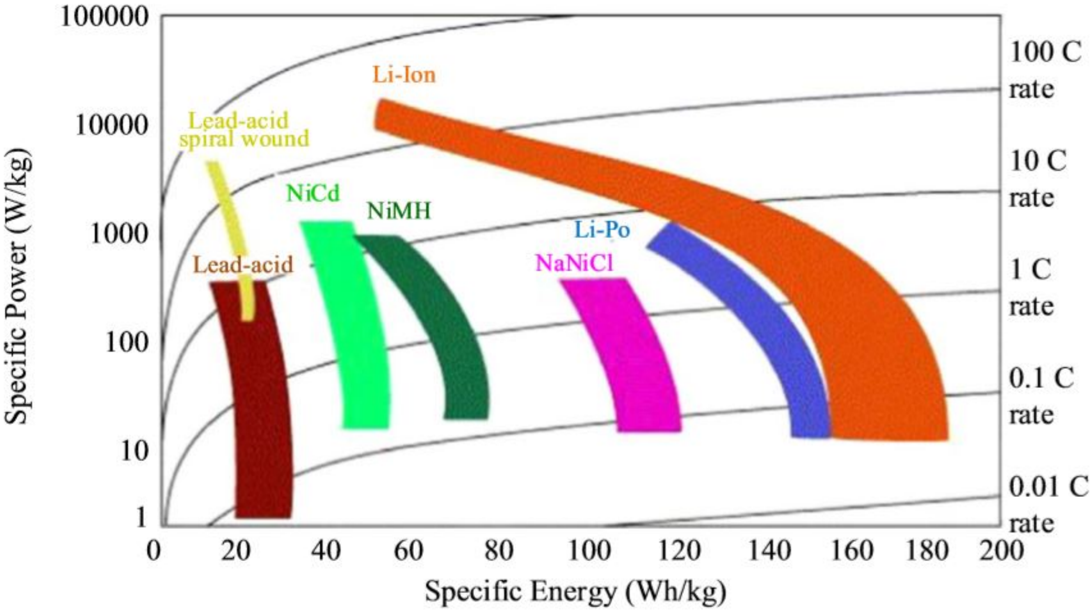

Figure 1.2: Ragone plot

1.2 Lithium-ion cell chemistry

The battery is an electrochemical accumulator which stores charge when recharged and delivers it when discharged.
The the working principle of li-ion battery is characterized by the transport of the electrons and the lithium ions stored in one electrode to the other, as illustrated in figure , creating a certain voltage difference between the two electrodes. [3]

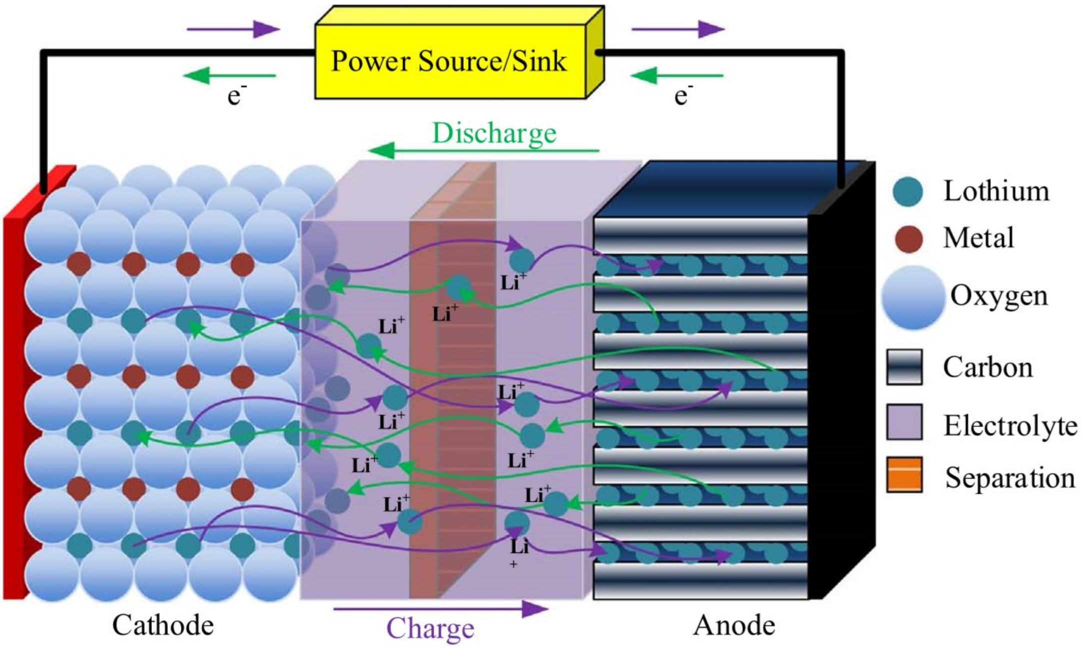

Figure 1.3: Litium-ion battery working principle [3]

During charge, lithium ions are extracted from the cathode particles, and flow through the electrolyte and the separator towards the anode. The same amount of electrons is released from the positive electrode in order to keep the electric equilibrium. The electrons are collected by the positive current collector and reach the negative electrode by means of the external circuit, determining the charging current. Finally the lithium ions are intercalated in the anode particles reacting with the electrons arrived from the cathode. This exchange is explained by the electrochemical reactions which occur in the electrodes reported in 1.1. Indeed an oxidation reaction that releases electrons and lithium ions occurs at the positive electrode and a reduction reaction that consumes electrons and lithium ions occurs at the negative electrode during charge.

$$\begin{cases} Li_{1-x}C_6 + xLi^+ + xe^- \underset{discharge}{\overset{charge}{\rightleftarrows}} LiC_6 & \text{Negative electrode} \\ LiFePO_4 \underset{discharge}{\overset{charge}{\rightleftarrows}} Li_{1-x}FePO_4 + xLi^+ + xe^- & \text{Positive electrode} \end{cases} \quad (1.1)$$

An inverse electrochemical process occurs during discharge, when the same amount of lithium ions and electrons travel from the negative electrode back to the positive one through the internal and external passage respectively.

1.2.1 Negative electrode

Anode material can be classified in three different groups according to their energy storage system: intercalation-based, conversion-reaction-based and alloying-reaction based materials. The first group of materials is the most widespread in automotive field.

The choice for anode material is not really wide, however some types of material are available for this purpose. The feature of the most widespread material are summarized in figure 1.4 and 1.5.

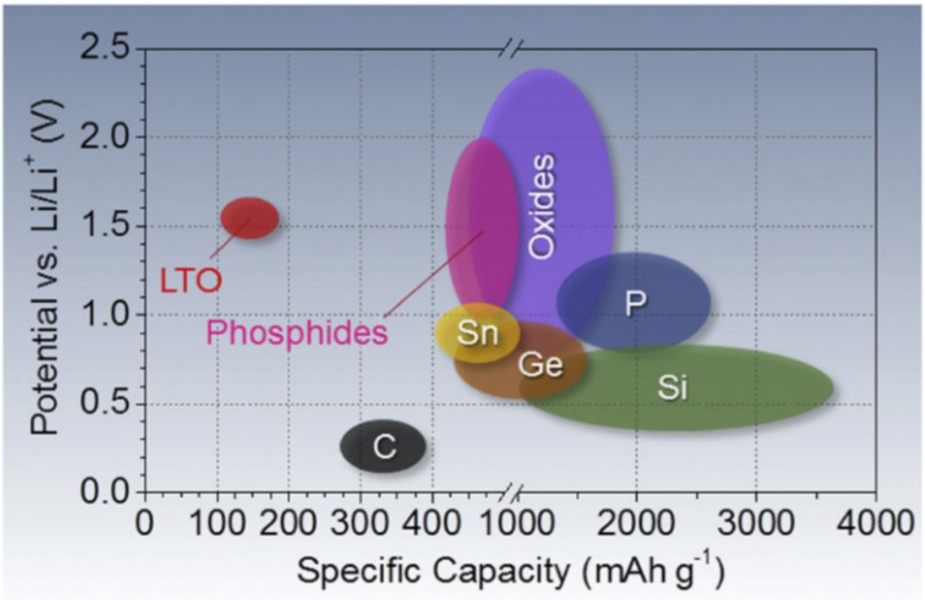

Figure 1.4: Range of average discharge potential and specific capacity of the most common intercalation-type anode material

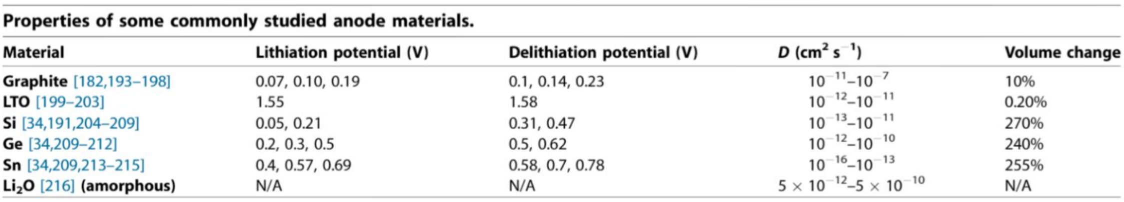

Properties of some commonly studied anode materials.

Material	Lithiation potential (V)	Delithiation potential (V)	D (cm^2 s^{-1})	Volume change
Graphite [182,193–198]	0.07, 0.10, 0.19	0.1, 0.14, 0.23	10^{-11}–10^{-7}	10%
LTO [199–203]	1.55	1.58	10^{-12}–10^{-11}	0.20%
Si [34,191,204–209]	0.05, 0.21	0.31, 0.47	10^{-13}–10^{-11}	270%
Ge [34,209–212]	0.2, 0.3, 0.5	0.5, 0.62	10^{-12}–10^{-10}	240%
Sn [34,209,213–215]	0.4, 0.57, 0.69	0.58, 0.7, 0.78	10^{-16}–10^{-13}	255%
Li_2O [216] **(amorphous)**	N/A	N/A	5×10^{-12}–5×10^{-10}	N/A

Figure 1.5: Overview on anode materials and their properties

Intercalation-based materials

This type of materials host within their particles the lithium ions which migrate from the cathode and then release them during delithiation allowing to achieve a good cycle life.

Graphite is the widest used material for anode and allowed the commercial spread of lithium-ions batteries from more than 20 years.

Graphite structure offers a good mechanical stability, electrical conductivity, Li diffusion and a relatively low volume change due to lithiation/delithiation. Lithium ions intercalate between the planes of the graphite particles. Six lithium atoms per one atom of carbon can be stored, as showed by the electrochemical reaction in equation 1.2.

$$Li_{1-x}C_6 + xLi^+ + xe^- \underset{discharge}{\overset{charge}{\rightleftarrows}} Li_xC_6 \text{ Negative electrode} \tag{1.2}$$

Carbon is one of the best choice for anode, thanks to its relatively low cost, abundance, moderate energy density, power density, and cycle life. However the volumetric capacity of commercial graphite electrodes is still small, around $330 - 430mAh/mm^3$, less than other materials. Graphite has relative large particle size (micrometer radius) and can achieve a capacity close to the theoretical one. However it does not combine well with propylene carbonate (PC) electrolyte,

which is known for its low melting point and fast lithium transport. Indeed PC electrolyte tends to intercalate together with Li ions and cause graphite exfoliation and capacity fade.
Graphite particles experiences uniaxial strain deformation (about 10% along the radial direction) during lithiation, which is the main reason of performance degradation with cycling. Lithiated graphite and Li/Li+ have about the same electrochemical potential, so when it is combined with a suitable active material of the positive electrode the cell can have a high voltage and high energy density. [20]
A reductive electrolyte decomposition occurs in the interface between the electrode and the electrolyte during the charging process, since the anode operates at voltage values outside the electrochemical stability window of the electrolyte components. The decomposition reaction produces a film which lie on the electrode surface. This film growth decreases after the first cycles and stabilizes at a certain thickness.
The layers build up on the graphite surface can be divided in two different types, according to their location and function. The protective layers act as solid electrolyte interphase (SEI) on the surface where the the lithium ions transport takes place by the intercalation/deintercalation in the particle. The SEI contains several components depending on electrolyte composition, and its unique properties allow the migration of lithium ions, but act as a impermeable layer for electrons and other electrolyte components. So, these properties prevent further reductions of the graphite surface and the corrosion of charged electrode. The protective layers which lie on the surface where no lithium exchange occurs are commonly called non-SEI layers, they have a different composition respect to the SEI one and does not have the same function, but still protect the anode from further reduction.
The SEI properties mainly depend on the composition of the electrolyte, so solvent and additives should be taken in consideration in order to improve its stability, and to decrease the irreversible capacity and self discharge rate, resulting in a supporting effect both in the formation processes but also in the ageing process.
The decreasing of cell performances at high temperature mentioned in the "safety issue" chapter is related to the degradation of the SEI film, which start to break down and dissolve even below 60°C. [21]

Hard carbons have smaller grains, which are less susceptible to exfoliation. The nanovoids between the grains reduce the volume expansion and provide excess gravimetric capacity, resulting in a capacity grater than the theoretical one. However an higher fraction of surface of the planes exposed to the electrolyte increases the SEI produced, decreasing the capacity in first few cycles. Moreover they suffer large voltage hysteresis, higher irreversible capacity loss and even lower volumetric capacity, so they are unlikely to be commercialized.

LTO best features are related to its thermal stability, high rate and high cycle life. Its weak points are the high cost of Ti, the reduced cell voltage and the lower capacity ($175mAhg^{-1}$ and $600mAhmm^{3}$). The slight radial strain (about 2% in volume change) induced by the intercalation/deintercalation process in combination with the high potential of lithiation makes LTO a safe material and allows high current rate.
The high equilibrium potential (about 1.55V versus Li/Li^{+}) allows LTO to be

operated in a potential window above 1V, avoiding the formation and growth of SEI, which can slow down lithium diffusion and reduce lithium ions available for cycling. Moreover its high potential enhances the cell safety because it prevents dendrite formation even at high current rate, which could lead to internal short circuit.

Then the low volume change rate preserves the SEI layer and allows the use of nanoparticles, which lead to higher rate performance at the expense of volumetric capacity. Finally even if LTO is not characterized by an high Li diffusivity or electrical conductivity and has a low energy, it has an high power density and a long cycle life.

An important limitation is related to the surface reactions which are not completely avoidable with LTO anodes. They occur between the organic electrolyte and the LTO active material, generating an important amount of gasses. This reactions can be reduced by carbon coating, which however can catalyze and accelerate SEI formation, especially at elevated temperatures. However this anode material can last for tens thousands of cycles, representing an interesting option for high power applications.

Conversion-reaction-based materials The working principle of this type of material is based on the Faradaic reaction represented in equation 1.3

$$M_aX_b + Li^+ + ae^- \xrightleftharpoons[discharge]{charge} aM + bLi_nX \tag{1.3}$$

Where M are transition metals such as Ti, V, Cr, Mn, Fe, Co, Ni, Cu, Mo, W, Ru. And X are anions composed by non metal elements such as O,N,F,S and P. A variety of anode materials are possible combining the mentioned metals and anions.

This material can reach high values of theoretical capacity which is in a range between $350mAhg^{-1}$ for Cu_2S and $1800mAhg^{-1}$ for MnP_4.

However they have some limitations concerning discharge to charge efficiency, volume expansion and high reaction potential. The low discharge to charge efficiency makes this material cyclability very poor compared to graphite. The huge volume expansion during lithiation/delithiation could lead to pulverization or electric isolation.The higher reaction potential plateau makes the energy density associated to this material lower than the graphite one. [20]

Alloying-reaction based materials Silicon is the the most widespread among the alloying materials for anode. It is probably the next generation material for anodes, since its huge theoretical capacity can overcome the existing limits of lithium-ion battery in automotive applications concerning their poor autonomy.

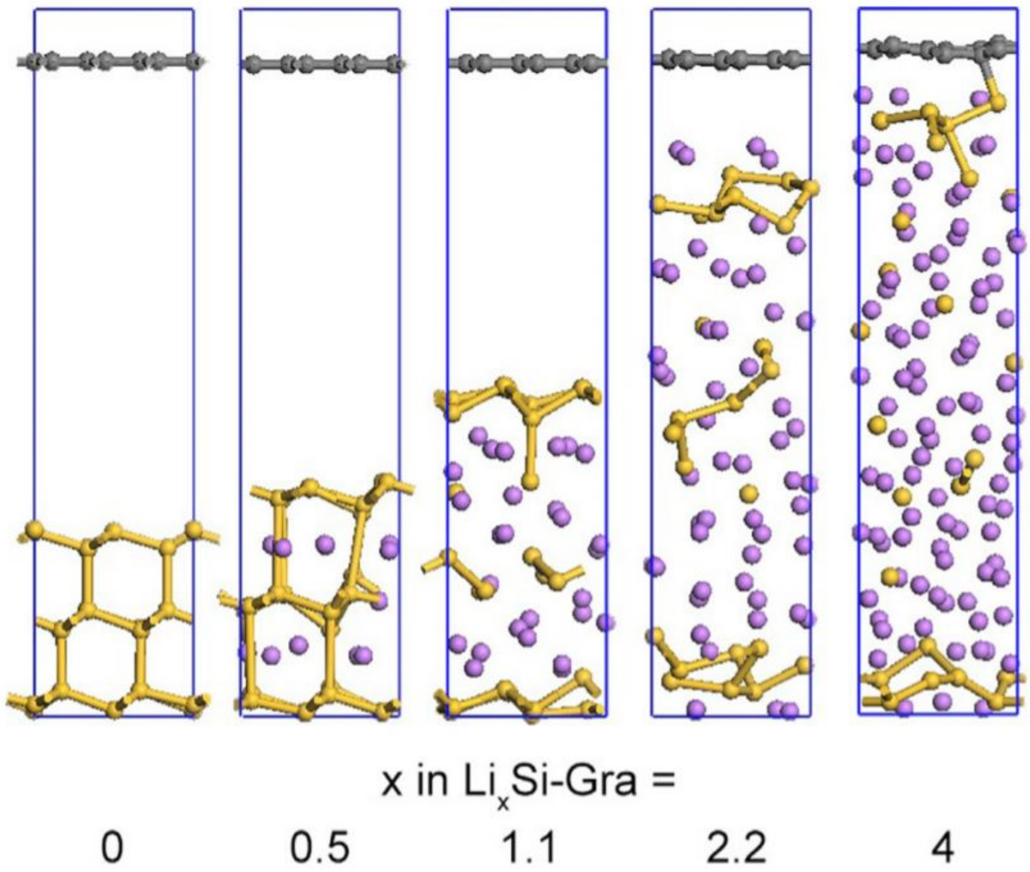

Figure 1.6: Configurations of the LixSi-Graphene system at various stages of lithium insertion [30]

The main problem with this type of material is the huge volume change during lithiation/delithiation process, since it can expand up to 300% the original volume, as shown in figure 1.6.
A huge volume change causes the destruction of the SEI layer, resulting in continuous electrolyte decomposition which leads to lithium inventory consumption and cell impedance increase. The strategy to reduce this problem is to produce a carbon coating of sufficient small dimensions in order to ensure mechanical stability, electron and Li transport, while maintaining Li diffusion paths within the electrode.
Also the SEI layer is stabilized encapsulating the active material in a bigger carbon shell which allows volume expansion, as shown in figure 1.6. Binder can replace carbon shell, bonding the active material and improving mechanical stability.
Si is the most interesting alloying material, thanks to its relatively low average delithiation potential, extremely high gravimetric and volumetric capacity, abundance, low cost, chemical stability and non toxicity. [20]

The comparison between the most common anode materials in terms of potential versus specific capacity is presented in figure 1.7.

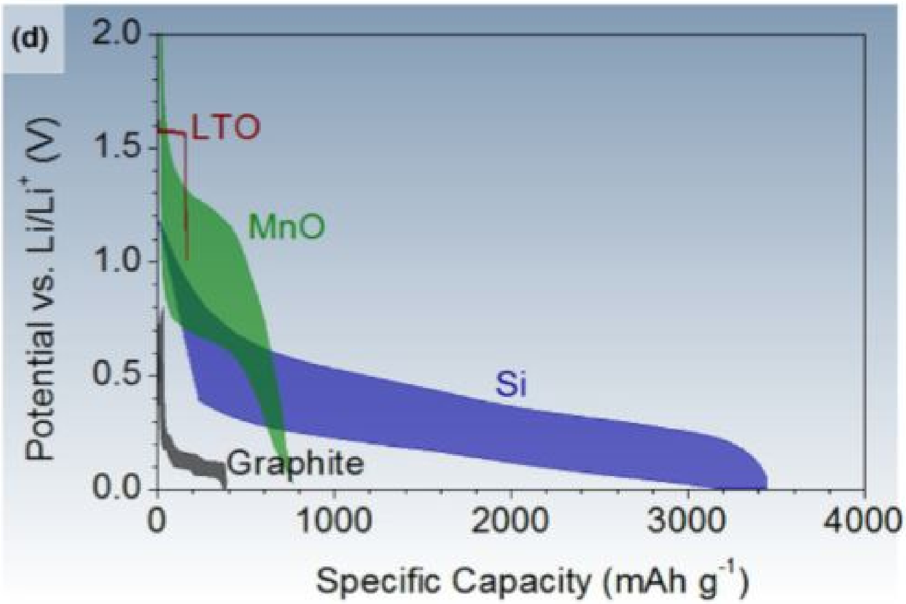

Figure 1.7: Discharge profile over the SOC window for anode material

1.2.2 Positive electrode

The choice of a cathode material has to satisfy some requirements such as capacity, energy and power density, cost thermal and structural stability.

Cathode material stores energy through two different mechanisms: intercalation and conversion reaction.

The conversion materials exchange Li ions and electrons according to a solid-state redox, which provides a change in the crystalline structure, accompanied by the breaking and recombining of the chemical bonds. However this type of materials presents an high volume expansion, poor electron conductivity and hysteresis issue, which make them not common in lithium ion cell application, and therefor they will not be mentioned in this section.

Intercalation materials act as a solid host network which can store guest ions. The ions can be inserted and removed from the host network reversibly. The host network compounds could be metal chalcogenides, transition metal oxides, and polyanion compounds. These compounds can be divided into several crystal structures, such as layered, spinel, olivine, and tavorite. [20]

An overview on the cathode material is presented in figure 1.9, among them the most common are: lithium cobalt oxide (LCO), lithium iron phosphate (LFP), Nickel cobalt aluminum (NCA), Nickel cobalt manganese (NMC), and lithium manganese oxide (LMO)

The specific capacity versus potential plot of some of the most common cathode material is reported in figure 1.8.

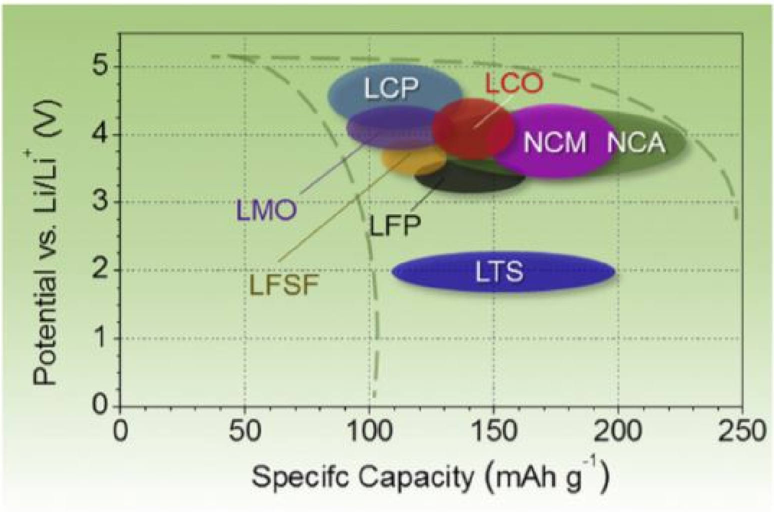

Figure 1.8: Range of average discharge potential and specific capacity of the most common anode material

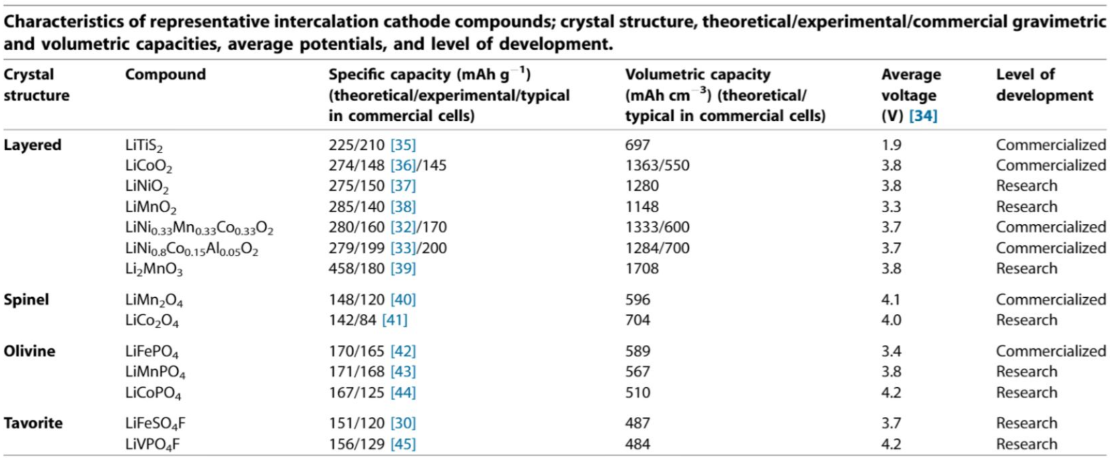

Characteristics of representative intercalation cathode compounds; crystal structure, theoretical/experimental/commercial gravimetric and volumetric capacities, average potentials, and level of development.

Crystal structure	Compound	Specific capacity (mAh g^{-1}) (theoretical/experimental/typical in commercial cells)	Volumetric capacity (mAh cm^{-3}) (theoretical/ typical in commercial cells)	Average voltage (V) [34]	Level of development
Layered	$LiTiS_2$	225/210 [35]	697	1.9	Commercialized
	$LiCoO_2$	274/148 [36]/145	1363/550	3.8	Commercialized
	$LiNiO_2$	275/150 [37]	1280	3.8	Research
	$LiMnO_2$	285/140 [38]	1148	3.3	Research
	$LiNi_{0.33}Mn_{0.33}Co_{0.33}O_2$	280/160 [32]/170	1333/600	3.7	Commercialized
	$LiNi_{0.8}Co_{0.15}Al_{0.05}O_2$	279/199 [33]/200	1284/700	3.7	Commercialized
	Li_2MnO_3	458/180 [39]	1708	3.8	Research
Spinel	$LiMn_2O_4$	148/120 [40]	596	4.1	Commercialized
	$LiCo_2O_4$	142/84 [41]	704	4.0	Research
Olivine	$LiFePO_4$	170/165 [42]	589	3.4	Commercialized
	$LiMnPO_4$	171/168 [43]	567	3.8	Research
	$LiCoPO_4$	167/125 [44]	510	4.2	Research
Tavorite	$LiFeSO_4F$	151/120 [30]	487	3.7	Research
	$LiVPO_4F$	156/129 [45]	484	4.2	Research

Figure 1.9: Overview on cathode materials and their properties

Transition metal oxide

$LiCoO_2$ (LCO) introduced by Goodenough is one of the first active material studied and commercialized and still widely used in commercial Li-ion battery.The Co and Li are located in the octahedral sites and occupy alternating layers, forming an hexagonal symmetry.

LCO has interesting properties concerning its high theoretical capacity of $274 mAhg^{-1}$, high theoretical volumetric capacity of $1364 mAhcm^{-3}$, low self discharge, high discharge voltage and good cycling performance.

The major limitations concern the fast capacity fade at high current rates, the economic point of view due to the high cost of Cobalt, and the low thermal stability referred to the exothermic release of oxygen when the temperature grows over a certain threshold, which could lead to thermal runaway. Moreover deep discharging cycles (above 50% or more Li extraction) induces lattice distortion from hexagonal to monoclinic symmetry, decreasing the cycling performance.

Some metal alternatives such as Mn,Al,Fe,Cr were studied as partial substitutes

of Co, but limited performance were encountered. Stability and performance characteristics are enhanced during deep cycles by metal oxides coating (Al_2O_3, B_2O_3, TiO_2, ZrO_2) which reduce the structural change of LCO and side reactions with electrolytes. [20]
The metal oxide is lithiated/delithiated according to the following reaction: [6]

$$2LiCoO_2 \underset{discharge}{\overset{charge}{\rightleftarrows}} 2Li_{0.5}CoO_2 + Li^+ + e^- \tag{1.4}$$

$LiNiO_2$ (LNO) has the same crystal structure of LCO and similar theoretical capacity. The interesting low cost and high energy density compared to LCO prompted a good research in this material.
The weak point of pure LNO cathodes is in the tendency of Ni^{2+} to substitute $Li+$ during intercalation/deintercalation, reducing the lithium diffusion paths. Moreover LNO is even more thermally unstable than LCO because Ni ions are reduced faster than Co. Mg doping the adding of a small amount of aluminum improve both thermal stability and electrochemical performance.

This modified version of LNO is $LiNi_{0.8}Co_{0.15}Al_{0.05}O_2$ (NCA), which is commonly used in commercial lithium-ion batteries, such as for Tesla EVs. NCA has an high discharge capacity (about $200mAhg^{-1}$) and a long storage calendar life compared to Co-based oxide cathode.
Its weak points concern the high capacity fade rate at elevated temperature (40-70°C) due to fast SEI growth and micro-crack propagation at grain boundaries. [20]

The cheaper and less toxic features of the Mn enhance the spread of layered $LiMnO_2$ (LMO) cathodes since two decades, when a preparing method which prevents impurities contamination, different stoichiometries, poor crystallinity and undesirable structure change during cycling was discovered.
But some characteristics such as the tendency of the layered structure to change into the spinel one during delithiation and the leaching of Mn out of the LMO during cycling lead to weak cycling performance of LMO. Moreover Mn can dissolute into Mn^{4+} and Mn^{2+} ions, the last one can migrate towards the anode and destabilize the SEI layers with cycling since they are soluble in the electrolyte. Even cationic doping does not improve its cycle stability, especially at high temperature. [20]

The research of cheaper cathode material led to the formulation of $Li(Ni_{0.5}Mn_{0.5})O_2)$ (NMO), because of good energy density and the lower cost thanks to the cheaper transition metals, compared to LCO.
The Ni ions allow an higher Li extraction, so an higher capacity can be achieved. Moreover it has been showed that low valence transition metal cations, such as Ni^{2+}, provides high rate pathways, so a greater Li diffusion within the electrode particles is achieved, which results in a lower strain rate and a better cycle stability. The adding of Co in NMO enhances structural stability further. [20]

$LiNi_xCo_yMn_zO_2$ (NMC) is widely used in battery market with the same quantity of Ni,Co and Mn, i.e. $x = y = z = 0.33$. In the automotive field BMW uses

this chemistry for its electric models.
It has a good cycle stability even at 50°C, an higher achievable specific capacity, similar operating voltage and a lower price than LCO, since a lower amount of Co is used.
The Li_2MnO_3 adding enhances the capacity under high voltage operation, since when it is activated (>4.5V) it releases Li_2O which provides extra Li ions in the initial cycles. Then the remaining Li_2MnO_3 facilitates the Li diffusion and acts as a Lithium reservoir.
Recent researches showed that an average composition as $LiNi_{0.68}Co_{0.18}Mn_{0.14}O_2$ can achieve both good electrochemical features, meant as energy/power density and good cycle stability and safe.
Each particles has a greater nickel fraction (about $LiNi_{0.8}Co_{0.1}Mn_{0.1}O_2$) in the core, which enhances a greater energy and power density and prevent structural deterioration with high Li extraction. Then the outer layers have a concentration gradient with a progressive larger fraction of Co and Mn which enhances cycle life and stability. The origin of the stability of this material is supposed to be the stable MN^{4+} in the surface layer, which delays the gas evolution due to the reaction between Ni ions and electrolyte.[20]

Spinel $Li_2Mn_2O_4$, also called LMO as the layered one, has interesting characteristics due to the abundance, low cost and environmental friendliness of Mn.
In this structure the lithium occupy some octahedral interstitial sites and diffuses through the vacant ones. The rate of performance is increased by using nanoparticles, which determine a shorter diffusion length and a better electronic transport. Otherwise irreversible side reactions with electrolyte, oxygen loss from delithiated active material, Mn dissolution and the formation of tetragonal structures affect the cyclable performance adversely. [20]

Polyanion compounds
Polyanion compounds are characterized by the basic unit $(XO_4)^{3-}$ where X can be metal such as S,P,Si,As,Mo,W. Polyanions occupy lattice position and increase cathode redox potential and stabilize its structure.

$LiFePO_4$ is the most known among the polyanion compounds and is one of the most common cathode material in commercial lithium-ion batteries, it has an olivine structure and has good thermal stability, high power capability and a competitive cost.
The weak point of this material is related to the low average potential and low electrical and ionic conductivity. In fact the low potential combined with the nanostructured LFP electrodes result in a low energy density, which is the major limit of LFP cell.
Deep researches in the mechanistic understand of this material leads to an increasing of the rate performance by reducing the particles size in combination with carbon coating and cationic doping. [20]
Lithium iron phosphate delithiates into FePO4 during charging as shown by the electrochemical reaction 1.5 [6].

$$LiFePO_4 \underset{discharge}{\overset{charge}{\rightleftarrows}} Li_{1-x}FePO_4 + xLi^+ + xe^- \text{ Positive electrode} \tag{1.5}$$

LiFePO4 and FePO4 coexists throughout almost the whole SOC-window. This results in a flat potential of 3.45 V vs. Li/Li+, as showed in figure 1.10.
The safety of LFP is related to the strong bonding of oxygen in the phosphate group, this results in better resistance to thermal runaway respect to other active material. The low cost is related to the usage of cheaper material, compared to Nickel and cobalt. [20]

$LiMnPO_4$ (LMP) is another olivine structure which is characterized by an higher average voltage (about 0.4V greater than LFP) which allows to improve the low energy density of LFP, while a lower conductivity is obtained. [20]

$LiFeSO_4F$ (LFSF) is a tavorite structural material and is another promising cathode material thanks to its high cell voltage and good specific capacity ($151 mAhg^{-1}$). Moreover it does not need carbon coating and/or particle size reduction in order to improve electronic and ionic conductivity as LFP does. It is also a cheap option because of the low cost of the materials by which is composed. [20]

From the discharge profile in figure 1.10 some key factor such as potential level and capacity can be deduced for different cathode materials. [20]

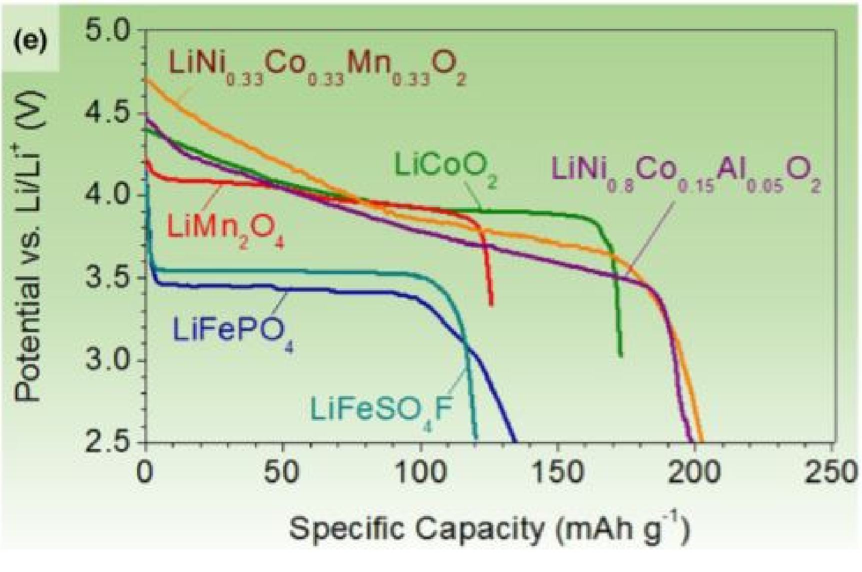

Figure 1.10: Discharge profile over the SOC window for the most common cathode material

Finally brief summary of the cathode material feature is presented in figure 1.11.

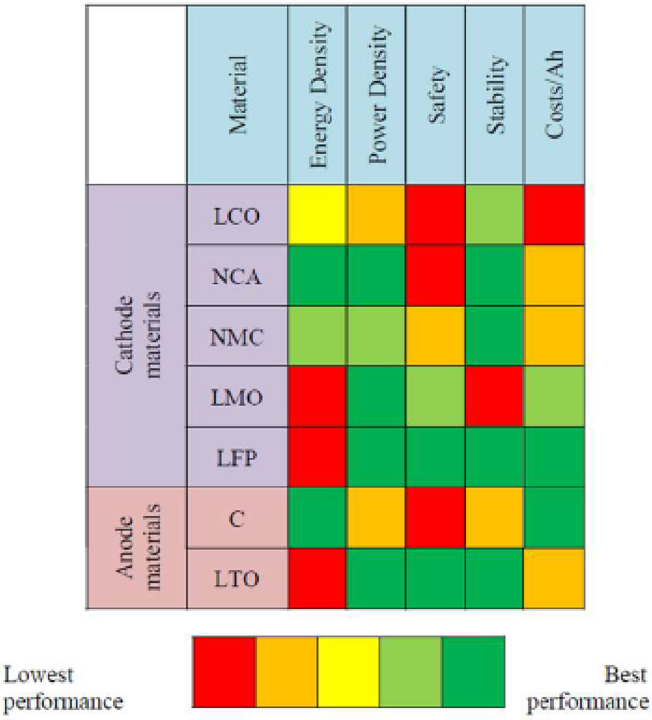

	Material	Energy Density	Power Density	Safety	Stability	Costs/Ah
Cathode materials	LCO	🟨	🟧	🟥	🟢	🟥
	NCA	🟩	🟩	🟥	🟩	🟧
	NMC	🟢	🟢	🟧	🟩	🟧
	LMO	🟥	🟩	🟢	🟥	🟢
	LFP	🟥	🟩	🟩	🟩	🟩
Anode materials	C	🟩	🟧	🟥	🟧	🟩
	LTO	🟥	🟩	🟩	🟩	🟧

Lowest performance 🟥 🟧 🟨 🟢 🟩 Best performance

Figure 1.11: Summary of cathode and anode material properties

1.2.3 Electrolyte

The electrolyte allows the ions migration between the electrodes, but does not conduce electric current. The electrolyte should have the following requirements: low viscosity and high ion conductivity at room temperature, stable with a wide electrochemical window and operating temperature range, the electrolyte components should be chemically and electrochemically stable toward other battery components such as the separator, current collector, and packaging materials, they have to enhance the formation of a SEI film on the surface of the negative electrode after the first cycles.
It usually consist of lithium salt dissolved in solvent that contains also small amounts of additives, such as flame-retardants and red-ox shuttles.
The lithium salts are correlated to the chemistry of the cathode, for example for LFP cells LiPF6 salt is used, that has appropriate characteristics related to electrochemical stability and usable temperature range.[6]
Carbonate solvent are the most widespread in lithium-ion cell. Examples of these type of solvent are ethylene (EC), diethyl-carbonate (DEC), propylene carbonate (PC), or dimethyl-carbonate (EMC).[3] Furthermore also ether solvents such as dioxolane (DOL), dimethoxyethane (DME) are used, especially associated with Silicon anode. This type of solvent ensure a low viscosity and an high ionic conductivity.

1.2.4 Separator and collectors

The separator is located between the positive and negative electrode, it allows the ions migration but prevents the electrode contact which lead to short circuit. It is a porous three layers polymer where the outer layers consist of polypropylene (PP) and the inner layer of polyethylene (PE). PE layer has a melting point (130 ℃) lower than PP layer, so the pores in the PE will close above this temperature and will provide a protection during an external short circuit. [6]

The collectors are the conductive zones from where the electrons are extracted. They are usually made of copper (anode) and aluminum (cathode). [3]

1.3 Safety issue

Safety is one of the most crucial aspect and is still an existing problem for the diffusion of electric vehicles. The right temperature working range is the main important requirement for lithium-ions battery.
Indeed figure 1.12 shows how the temperature influences the available capacity for the same number of cycles. The causes of a capacity fade are broadly linked to the SEI layer damage at high and low temperature. This fact broadly makes the graphite particles exposed to the electrolyte and allows the production of a new SEI, reducing the Li ions available for cycling.

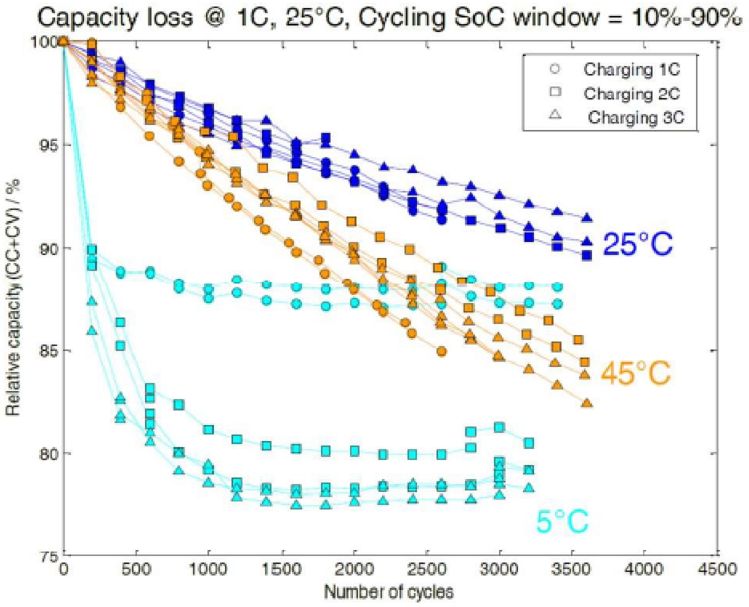

Figure 1.12: Temperature effect on battery performance

The damage of lithium-ion battery comes mainly from three source: mechanical, electrical and thermal, as shown in figure 1.13.

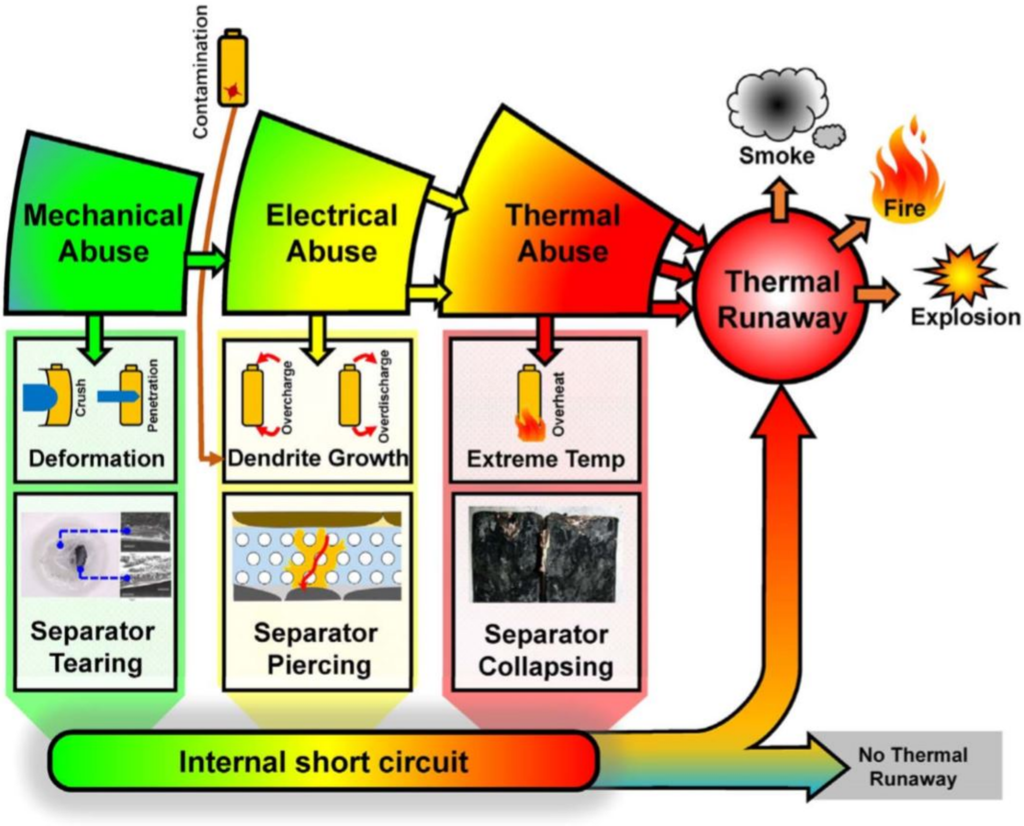

Figure 1.13: Sources of lithium-ion batteries damage [17]

Mechanical abuse, such as vibration or crush and penetration due to collisions, could induce damage in batteries which leads to capacity and power fade or more severe consequence as short circuit. In fact in case of collisions the internal structure of the battery could collapse making the positive and negative electrode in touch, causing internal short circuit. [17]

Electrical abuse is another critical problem for the batteries, it happens as a result of: external short circuit, overcharge or overdischarge over the cell limits potential.
Overdischarge causes a severe increase in the battery temperature and a progressive damage. In particular if the battery management system does not prevent the voltage to go below its lower limit, the copper decomposition of occurs. The dissolved copper can pass through the separator and deposits on the cathode surface, causing an internal resistance increasing and capacity fade. In some extreme cases the copper dendrite can grow until they touch both the cathode and the anode, causing internal short circuit.
When the battery management system does not stop the charging process when the upper voltage limit is reached overcharge occurs. Heat generation due to ohmic heat and side reactions, and gases release are the common characteristics of overcharge. Moreover lithium dendrites grow on the graphite surface due to the excessive interacalation rate, and simultaneously the high deintercalation rate in the cathode could cause its structural collapse.
External short circuit occurs when the positive and negative electrodes are con-

nected by a conductor, it does not heat the cell as the internal one. It acts like a fast discharging process, whose highest current is limited by the speed of lithium ions.
Thermal abuse can be caused by mechanical or electrical abuse for the reasons discussed earlier, however internal short circuit is the most dangerous source of thermal abuse . Internal short circuit occurs when the cathode and anode gets in touch due to the failure of the separator, developing a huge heat amount.
The danger connected to internal short circuit can be divided in three levels as shown in figure 1.14. Generally it depends on the self discharge rate and the heat generation. In the first level the cell shows self-extinguish features, since the cell properties come back to default when abuse is no longer applied, and the cell shows just slow self-discharge and no heat generation. In the second level irreversible voltage drop and temperature rise occur. Then in the third level the collapse of the separator causes a huge heat generation and voltage drop to zero, the reactions becomes unstoppable.

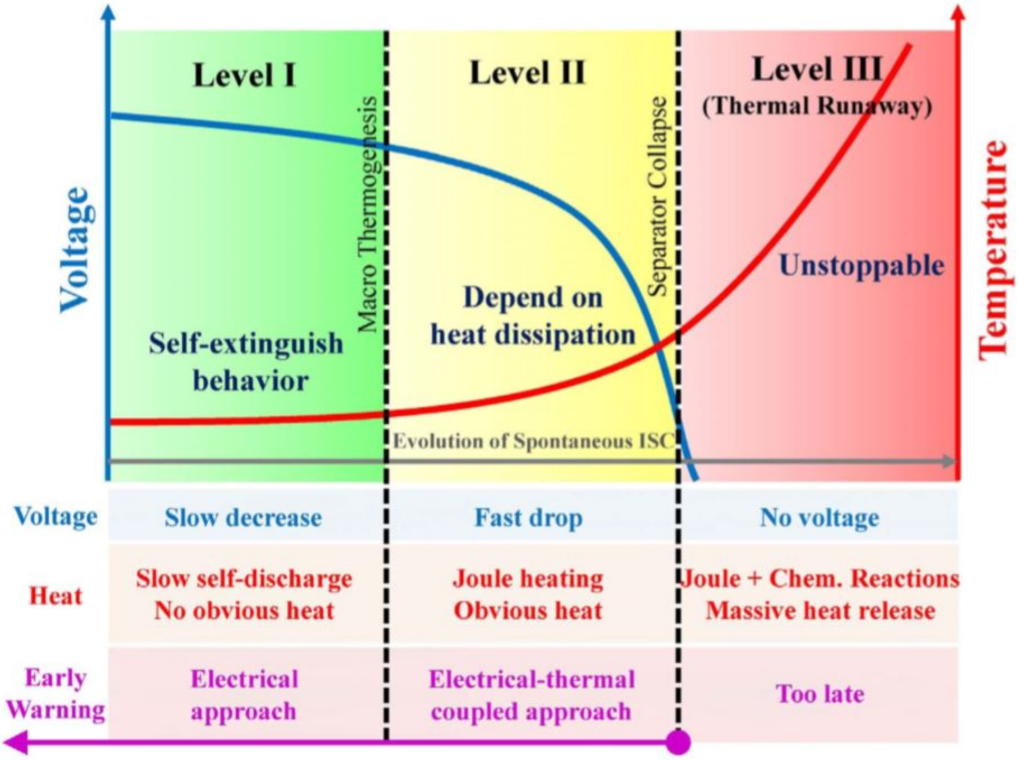

Figure 1.14: Internal short circuit stages [17]

It is interesting to study the mechanisms which leads to a progressive thermal damage, unitl the irreversible thermal runaway occurs. The mechanism which leads to thermal runaway can be interpretated as a chemical chain reaction which occur when the temperature rises abnormally under abuse condition. A graphic representation of the chemical reactions connected to the temperature and the timeline at which they occur is presented in figure 1.15.
The first reaction is the SEI decomposition on the anode, which takes place at approximately 100°C, exposing the graphite to the electrolyte. Then at about

250°C the graphite structure collapses, and also electrolyte decompose, releasing a large amount of heat. For what concerns the separator its melting becomes at about 130-170°C, which initially causes the close of the pores, making the lithium transfer more difficult. Then when the temperature goes over 260°C the separator with ceramic coating melts down, leading to internal short circuit and electrolyte burning. At this stage the process becomes irreversible and unstoppable leading to thermal runaway, which can causes severe consequences, such as fire or explosion. [17]

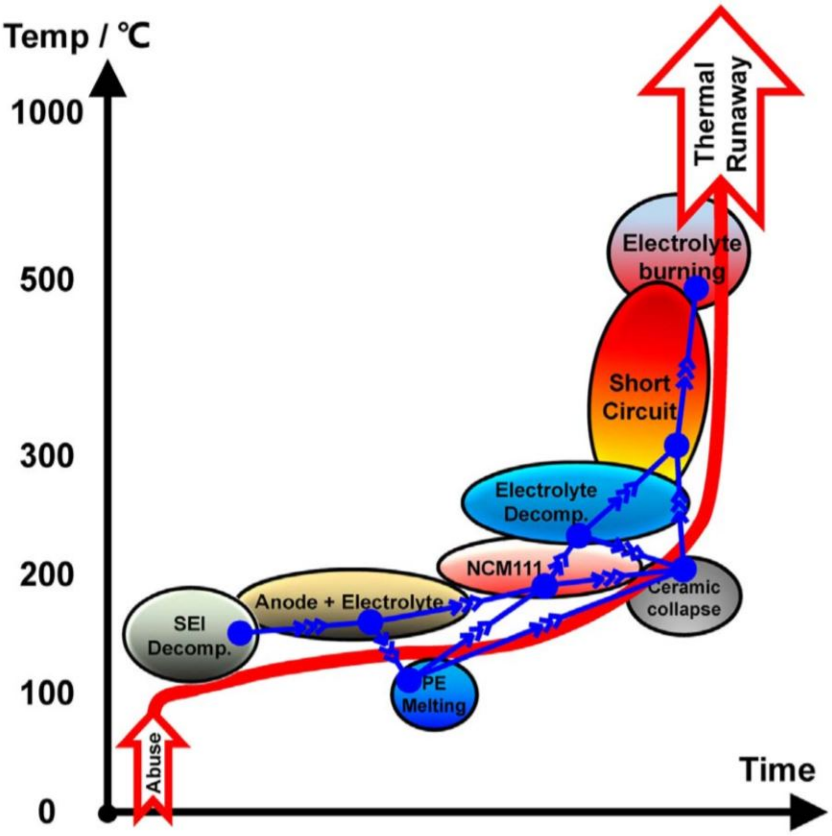

Figure 1.15: Runaway chain reaction [17]

1.4 Multi-scale nature

Battery is an interesting multi-scale physic problem, since exist several different models based on very different scale phenomena, as shown in figure 1.16. Lithium diffusion and particles stress models are established at the particles scale, which is around the micrometer. Charge balance and transport, and lithium transport in electrolyte phase models are based on electrode scale, which is around the tenth of millimeter. Current distribution, heat generation and transfer models are characteristic of the cell scale, around decimeter. Finally inter cell heat and electrical distribution models are established at module scale.

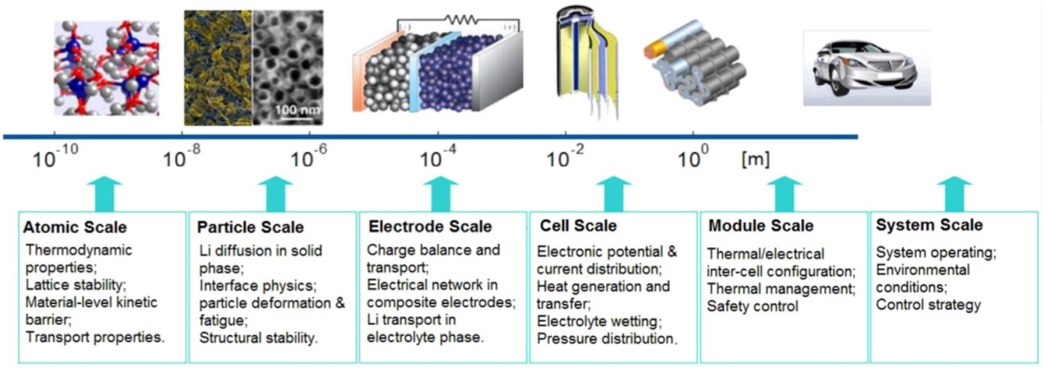

Figure 1.16: Multi-scale physis of lithium-ion battery [2]

In chapter 3 we are interested in the study of the stresses which arise from lithium intercalation. So a model at particle size is established in order to describe how the concentration gradient of lithium ions deform the particle, and how the deformed particles interact each other.
A graphical representation of the anode at particle scale is presented in figure 1.17. Both graphite and several intercalation-based material of cathode can be assumed as spherical particles, according to the SEM images presented in figure 1.18. Moreover this makes the approach presented in chapter 3 suitable both for anode and cathode intercalation materials.

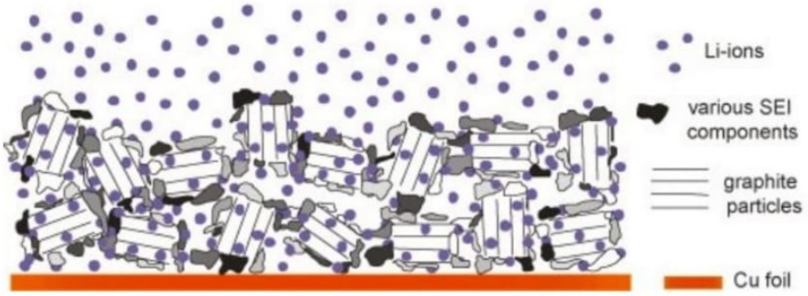

Figure 1.17: Anode at particle scale

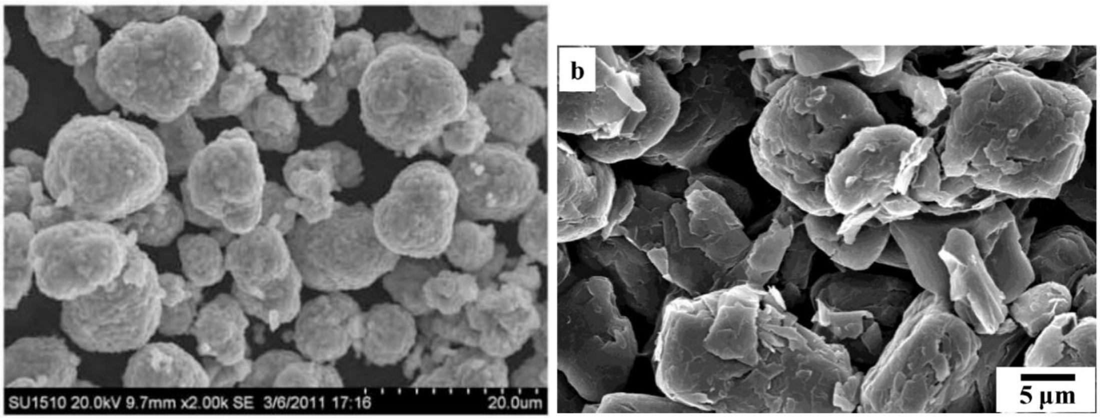

Figure 1.18: SEM images of active material: NMC (cathode) on the left, graphite (anode) on the right [31]

1.5 Configuration

The cells can be distinguished according to their structure: pouch, cylindrical or prismatic, as shown in figure 1.19 [2].
The pouch cells are characterized by a small thickness and a low weight, since they have not a rigid case. For these reasons they are suitable for telephony application and they cool down easily because of wide surfaces, but a proper packing is requested due to their weak mechanical characteristics.
Cylindrical cells are characterized by an excellent packing of the electrodes and separator inside the cell. In fact they are wrapped and inserted in the case with the electrolyte, filling all the available space into the case. On the other hand a set of cylindrical cells are hard to be packed in a module due to their geometry.
Prismatic cells are characterized by the fact that electrodes and separator wrapped in the case do not fill all the available space in the case, but on the other hand a set of prismatic cell can be easily packed in a module.
Both cylindrical and prismatic cells are characterized by an high energy density and good mechanical properties, since the case is made of aluminum or steel. [3]

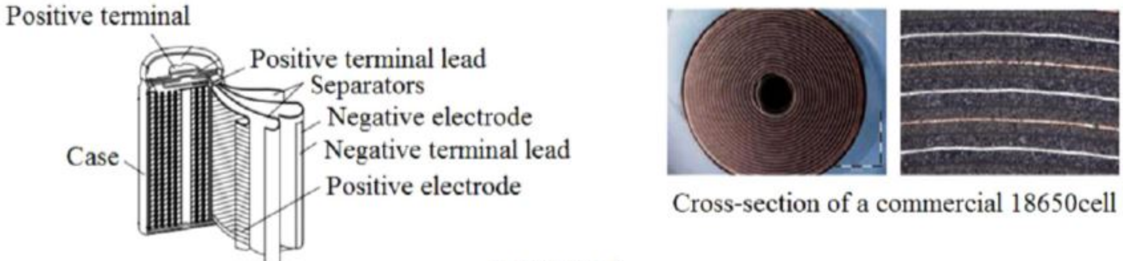

Cross-section of a commercial 18650cell

Cylindrical

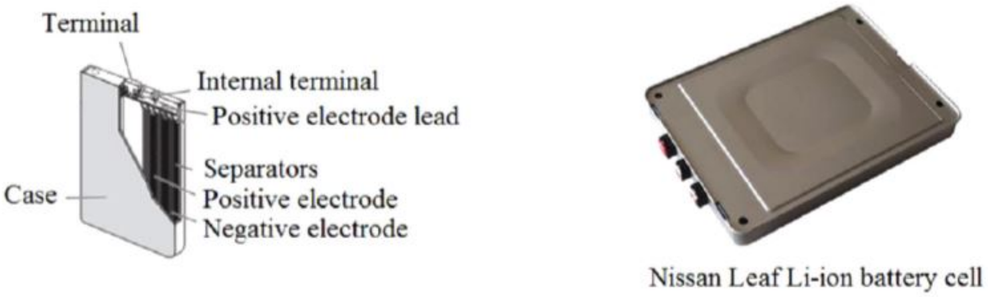

Nissan Leaf Li-ion battery cell

Prismatic

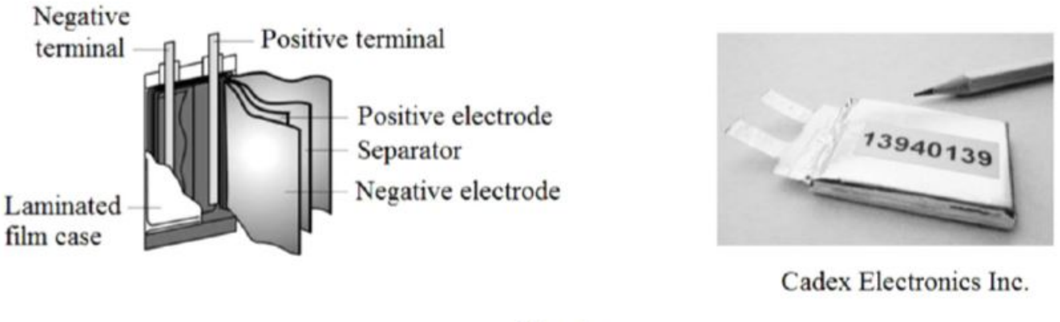

Cadex Electronics Inc.

Pouch

Figure 1.19: Cell configuration [2]

A single cell has a very low potential and capacity, for this reason, depending on the application, a large number of cell are connected in order to obtain the required amount of power. The set of several cells is called module, therefore the battery pack is composed by a variable number of modules.

Chapter 2

Aging mechanism

Several phenomena contribute in damaging of lithium ion cell, their understanding allows to build up a proper mathematical models and experimental tests.
This study aims to deepen the knowledge on capacity fade, so the phenomena which cause this type of damaging are examined in the next section.
A schematic summary of all the possible degradation mechanism is reported in figure 2.1.

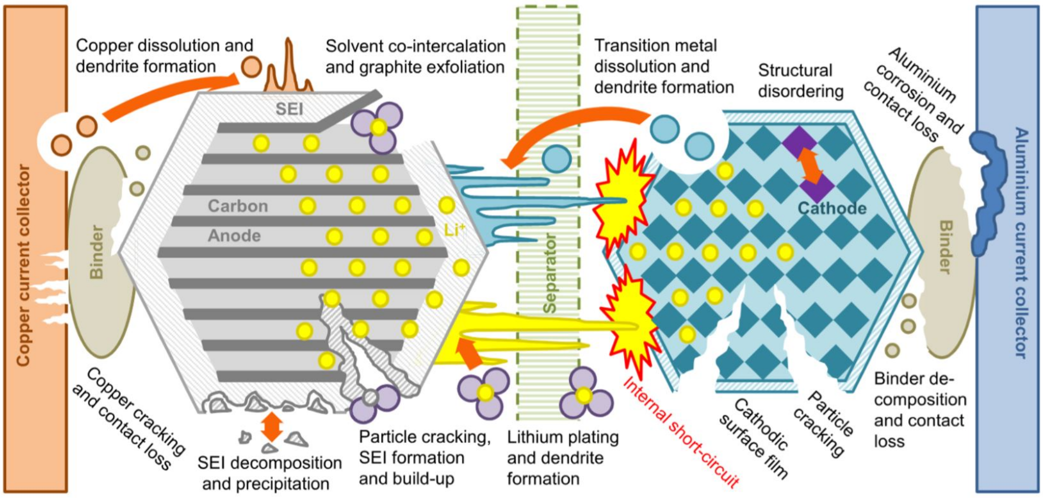

Figure 2.1: Schematic summary of degradation mechanism in lithium ion cell [4]

2.1 Capacity fade mechanism

Aging effects lead to a variation of the electrode properties and could occur during storage or use. In the first case they affects the calendar life of the battery and are mainly related to self discharge and impendance rise. In the latter case they are due to mechanical degradation and lithium plating and affect the cycle life. This type of degradation can be monitored by measuring capacity fade, impedance rise, closely related to power fade, and over potentials.

Capacity fade is mainly related to three phenomena:

Loss of lithium ions. The reduction of lithium ions available for cycling causes a progressive reduction of cell capacity because the fewer the lithium which

can be stored in the electrodes, the fewer the potential which can be reached at the end of the charge.
The lithium consumption is mainly due to side reactions which occur in the electrolyte, such us decomposition reaction, lithium plating and especially surface film formation (SEI growth). Moreover lithium ions could be trapped in electrically isolated particles and no longer available for cycling.

Loss of anode active material. Cracks on the particles of the active material could lead to a reduction of the material available for lithium insertion and loss of electrical contact between the particle and the binder or the current collector.

Loss of cathode active material. Structural disordering and crack could reduce the active material available for lithium insertion.

In these study we particularly focus on anode damaging, meant as reduction of electrical contact with the current collector and cracks propagation.
An interesting summary of the cause/effect relations of degradation mechanism is reported in figure 2.2.

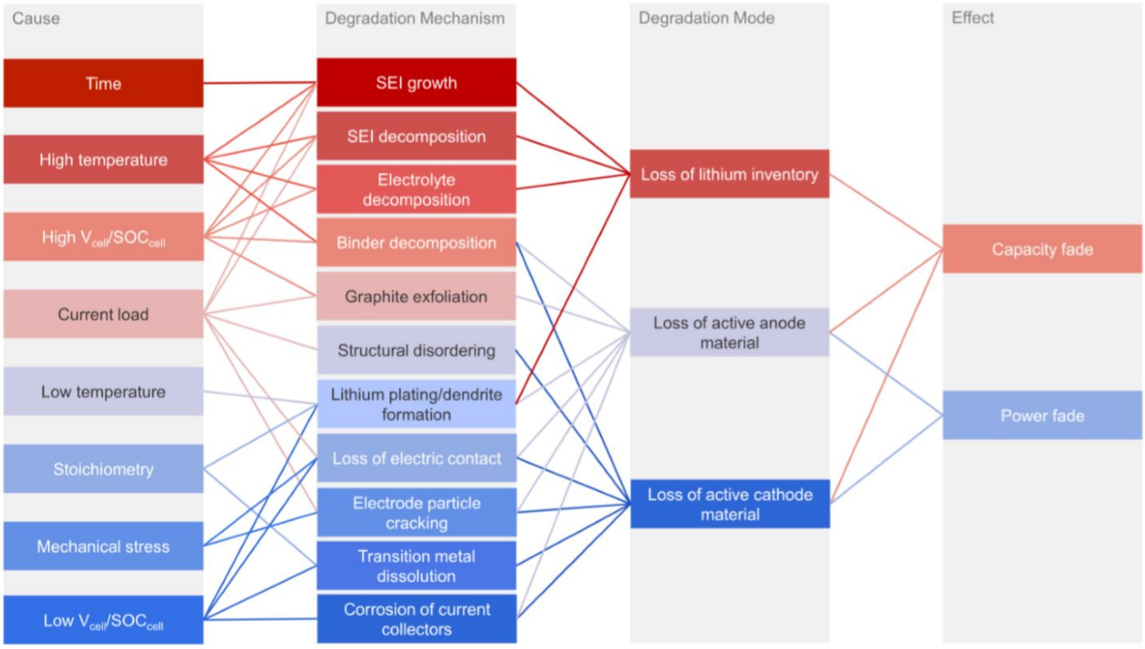

Figure 2.2: Lithium-ion anode ageing—causes, effects, and influences [4]

2.1.1 Change in electrode/electrolyte interface and SEI formation and growth

Changes at the electrode/electrolyte interface due to side reactions between anode and electrolyte are considered by many researchers to be the major source for ageing. In figure 2.3 are summarized the main phenomena which lead to changes at the anode/electrolyte interface.

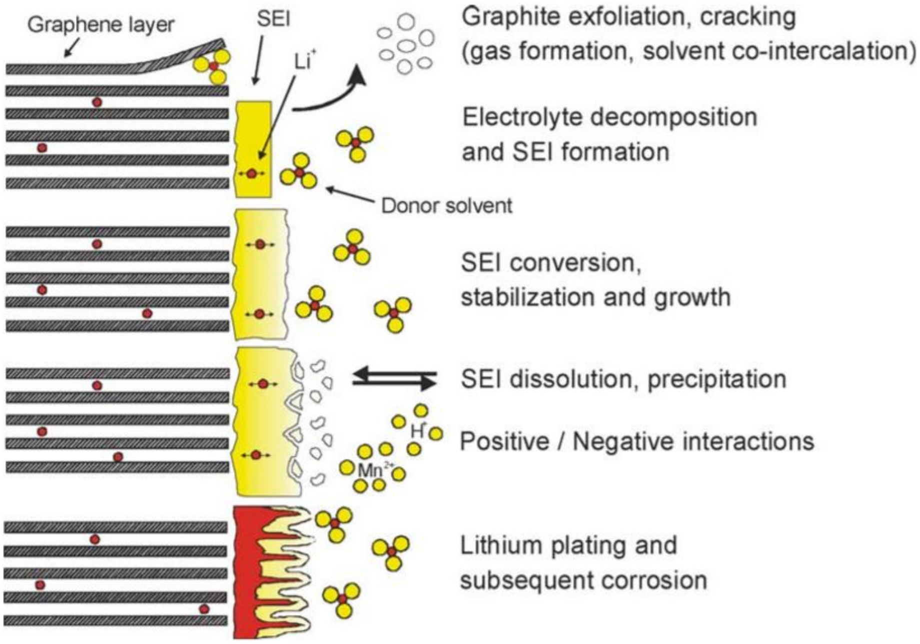

Figure 2.3: Lithium-ion anode ageing—causes, effects, and influences [7]

Graphite anodes operate at voltage values outside the electrochemical stability window of the electrolyte components, as shown in figure 2.4. For this reason the electrolyte decomposition takes place at the electrode/electrolyte interface when the electrode is in the charged state.

The decomposition products, the so called SEI layer, covers the electrode's surface. The SEI is mainly formed during the first cycles and protects the electrodes from further degradation, but causes also a capacity loss since it consumes lithium ion, and the loss of cyclable lithium is considered the most important reason to capacity loss.

The irregular growth of the SEI layer could be caused by cracks in graphite layer, since their presence allows the exposition of fresh active material to electrolyte. Several researches [22, 16] demonstrated that lithium intercalation causes crack in graphite particles. On the contrary no researches describes a possible mechanical failure, such as cracks, due to vibration load. It is supposed that if vibration load enhances cracks propagation, how might be expected, also this source of damage could induce a capacity fade.

The properties of the SEI layer are not comparable to the one of a solid electrolyte, and other charged species (anions, electrons, solved cations) and neutral species (solvent and impurities) still diffuse through the SEI in the later stages of cycling, causing anode corrosion (capacity fade) and electrolyte decomposition throughout the entire battery life. However this effects occur at a lower extent and at lower rate, compared to the first cycle. [7]

On a long time scale the SEI penetrates into pores of the electrode, resulting in a decrease of the accessible active surface area of the electrode.

The SEI growth can leads to a gradual reduction of the contact between the particles of the active material, causing an increase in the cell impedance.

The increase in electrode impedance is considered to be caused by the growth of the SEI as well as by changes of the SEI in composition and morphology. Indeed even if the SEI formation takes place just in the first cycles, the SEI conversion proceeds also during further cycling and storage.

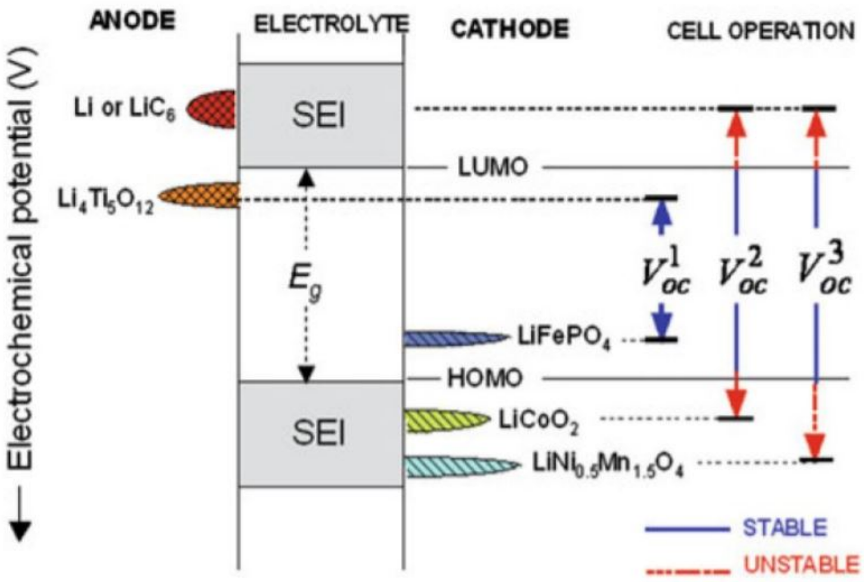

Figure 2.4: Electrochemical potential of some common active materials related to electrochemical window of the electrolyte (HOMO-LUMO)

It is widely accepted that high temperature affects the morphology and composition of the SEI layer. Indeed the negative impact of elevated temperature on cell ageing is mainly related to the degradation of the SEI layer which starts to break down and to dissolve. Great influence of the temperature is registered when the cell are stored at elevated temperature even below $60°C$.

Even low temperatures result in different changes. It emphasizes the slow lithium ions diffusion into carbon and/or in the electrolyte. Moreover it can cause metallic lithium plating and lithium dendrite growth.

Finally the interaction of the cathode with anode has to be taken into consideration. In fact the transport of soluble SEI products between anode and cathode and possible chemical redox reactions at the respective electrodes could occur. However the main effect of the cathode on the anode properties is transition metal dissolution. In fact transition metal ions (such as Mn^{2+}) in $LiMn_2O_4$ spinel can be incorporated into the anode SEI, leading to accelerated cell ageing.
In [16] the loss of active material from the cathode was observed after the vibration test.

2.1.2 Damaging of the active material

The damage of active material is considered one of the main contribution to the capacity fade, mainly for three reasons: it reduces the active site for lithium ions intercalation [4], it reduce the electric contact and enhance the SEI production. For what concern the first reason is clear that a reduction of the specific active area decreases the hosting capability of lithium ions in the electrode, decreasing the capacity which can be stored in the cell.

The particle damaging can reduce the electric contact between the particles and the binder, reducing the electric transfer capability, moreover it can reduce the contact between the particle and the current collector, decreasing the amount of electrons transferred to the external circuit. This phenomenon is detected by cell impedance rise.

Therefore the crack formation creates new free surface within the graphite particles exposed to the electrolyte, this leads to the formation of a SEI layers on the new free surface, as in the first cycles of the cell. The high rate of SEI formation on the new surface cause a sharp increase of the lithium consumption, no more available for cycling.

2.2 Literature review

2.2.1 Capacity fade due to electrochemical load

A large amount of works confirms that the capacity reduction is linked to the number of charge/discharge cycles experienced by the cell. From the experimental point of view a lot of researches pointed out the dependence of capacity with the number of charge/discharge cycles. However, an interesting research [15] built up a mathematical model which links the capacity reduction to the number of cycles through the rate of lithium consumption due to the crack formation on the graphite particle surface. A schematic representation of this concept is presented in figure 2.5.

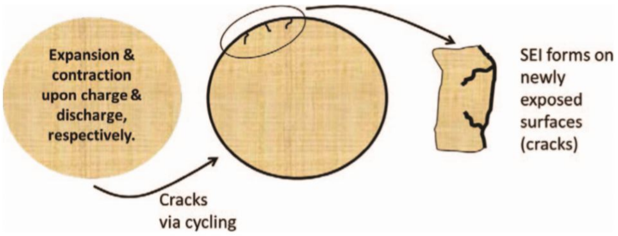

Figure 2.5: Scheme of lithium loss as a result of diffusion induced stress [15]

The crack formation and propagation are due the stresses which arise in the particle because of the intercalation/deintercalation of lithium ions. Then a model of crack propagation was established according to the Paris law, and the rate of lithium consumption was predicted according to the increasing length of the cracks,

which offers new free surfaces for SEI formation. The SEI growth and Paris law constants are considered as fitting parameter of the model.
Experimental tests show a good agreement with the mathematical model, as shown in figure 2.6.

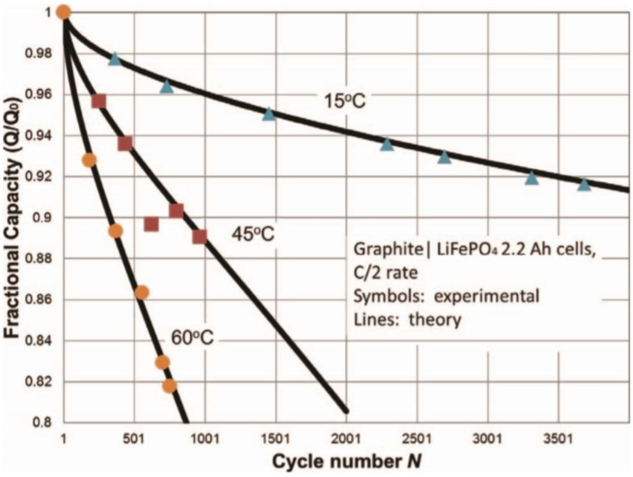

Figure 2.6: Capacity fade plot as a function of number of cycles for different temperatures. The dots represent the experimental data and the solid line represent the results of the model [15]

Moreover the figure 2.6 shows how the temperature affects the cell performance. In fact the temperature increase, even to quite common values, causes a sharp decrease in cell performance, which can be observed as a reduction of cell capacity for the same cycles number.

2.2.2 Capacity fade due to vibration load

A lot of studies were published in the last years in order to identify the factors which influence the service life, mechanical durability and reliability, such as C-rate, the depth of discharge and temperature. Nevertheless vibration load did not receive the same attention.
The vibration load, resulting for example from road roughness, could affect mechanical proprieties and electrical performance of batteries. In fact the fatigue load introduced by vibration could cause some problems in electrical power system, such as deformations and cracks in the electrode. [8]
Few researches are published concerning the effects of vibration load on batteries, and moreover they have reached contradictory result.

The largest works are done by Hooper and Marco from Warwik university, both in term of defining a signal which represented the vibration induced by the road in the whole vehicle life and in characterizing the variation of mechanical and electrical properties of batteries due to vibrations. [9-11]
In [9] they recording data from accelerometer driving the car over different road surfaces, then according to Millbrook structural durability schedule they defined a

proper sequence which represents the common use by European customers. Therefore the signal was time compressed keeping the same level of fatigue spectrum, so that it can be replicated on a shaker. From this analysis they understood that the common standard, such as UN 38.3 or SAEJ2380 are too strict compared to the real life stress.

In [11] they described the variation of mechanical and electrical proprieties, such as stiffness, Capacity, DC resistance, Ohmic resistance, charge transfer resistance and open circuit voltage. They observed an increasing of the internal resistance, a slight reduction in 1C capacity, which depend on initial SOC and cell orientation.
On the contrary in [10] they observed the same reduction in capacity both for control samples and the tested one, suggesting that the reduction was due to the laboratory environmental condition rather than the effects of vibration.
A too few samples were taken into consideration in [10-12], so that the fluctuation of the results associated with these phenomena makes impossible to distinguish whether the vibration or other causes leads to the change in the electrical performance of cells. These fluctuations are mainly due to accidental errors, cell-to-cell variation and environmental factors.

In [8] The authors followed a statistical approach to the problem, defining a number of samples which could guarantee an acceptable error. They observed a 5% reduction on cell capacity and an increasing trend in cell resistance after the vibration load described in SAE J2380 standard. The results are shown in figure 2.7.

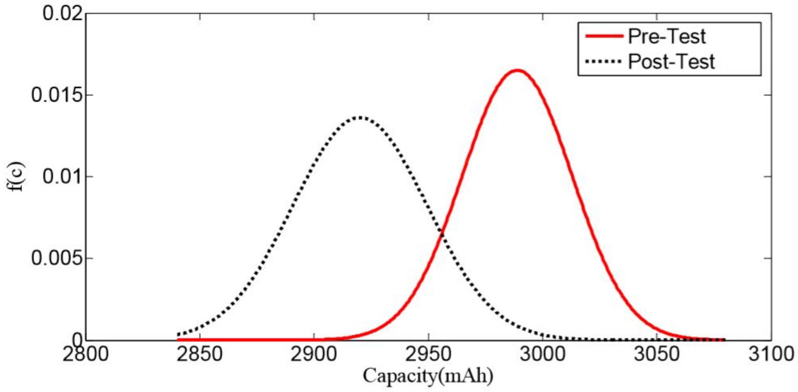

Figure 2.7: The distribution function and the theoretical normal distribution function of capacity samples after vibration [8]

In [10] the authors compared the results obtained by a sine sweep test and a long term vibration test for 186 days. In particular the sine sweep test was carried out ten times, and after each test the capacity was measured in order to describe how the capacity decrease. The result showed no capacity decreasing after the 10 sine sweep tests, and a slight capacity decrease in the long term vibration test.

In [13] the thermal effect of vibration load was investigated. In fact the author experienced that the lithium-ion battery of a small drone overheated in flight, but did not overheat when the electronic equipment was test on the ground. So the author performed some vibration tests to investigate how temperature field is linked to the mechanical stress.

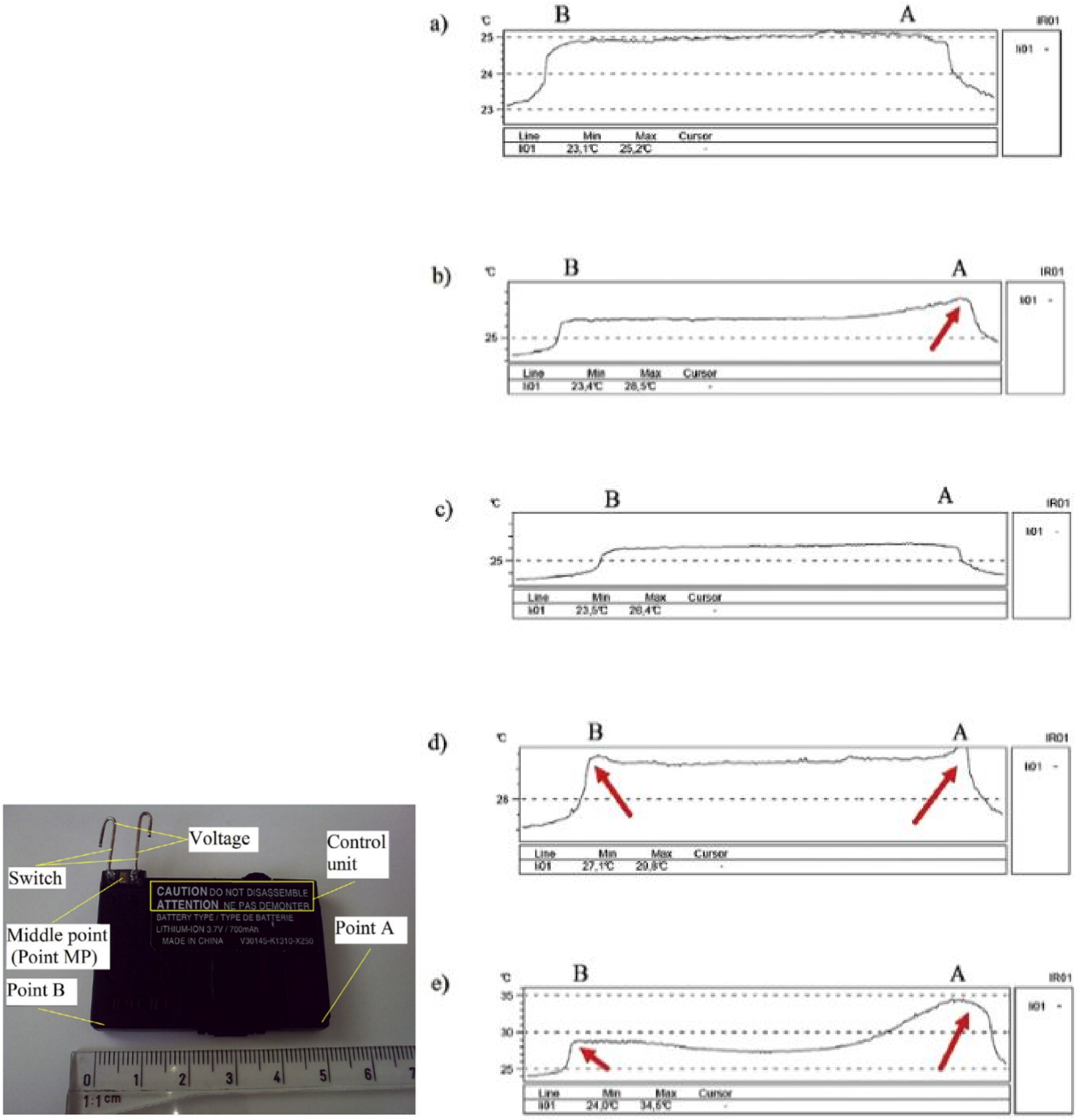

Figure 2.8: Left: Overview of the test battery and the monitored points [13]. Right: Temperature distribution in selected cross-sections: a) state before the experiment, b) after the first vibration cycle, c)after the second vibration cycle , d) after the third vibration cycle, e) after the fifth vibration cycle [13]

The cells, shown in left side of figure 2.8, were subjected to 5 vibration tests (30 seconds long, at 166.6Hz with 1mm of amplitude) and after each tests a thermogram was immediately taken and then the cell was subjected to an incremental increase current load from 0.01A to 0.1A.

The results presented in the right side figure 2.8 show an increment in temperature after each test, that could lead the cell to hazardous temperature value. Moreover the results show that the temperature is not uniform, but has some peaks in critical point at the edge of the cell.

Babu et al. [16] recently carried out a research about the effects of vibration on the damage of active material, on the internal resistance and on the dynamic properties of the cell.
For what concerns the morphology analysis two distinct observations can be made for anode and cathode. The anode was found intact and comparable to the one of the new cell, but the surface shows the presence of tower like structure due the deposition of material from the cathode, as shown in figure 2.9.

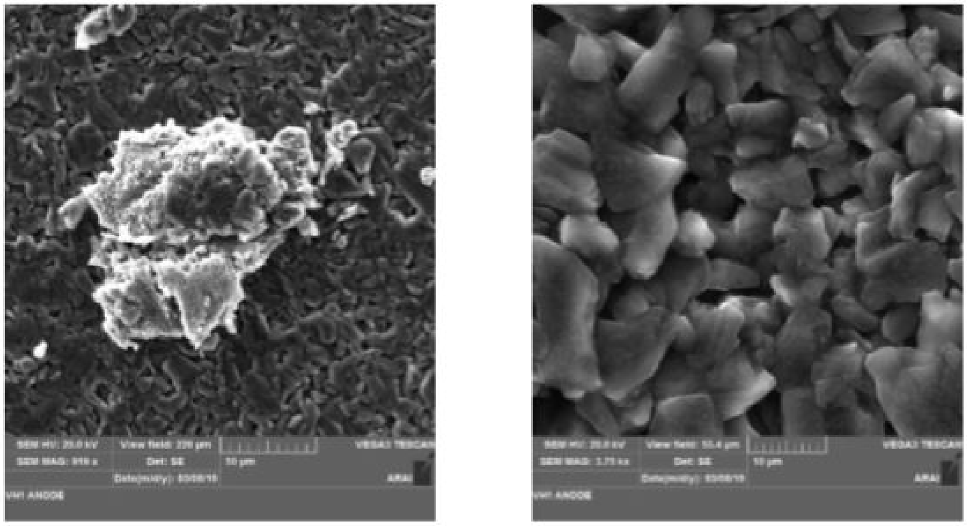

Figure 2.9: SEM images of the anode of the cell after vibration testing [16]

Even the cathode structure was essentially untouched, but the formation of crater like structure are noticed on the active material, as shown in figure 2.10.

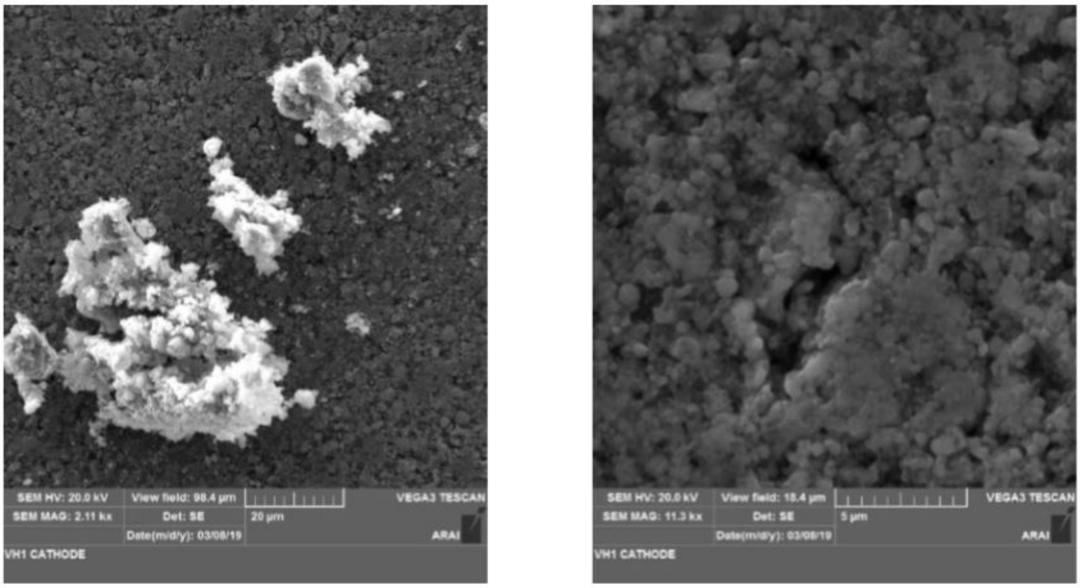

Figure 2.10: SEM images of the cathode of the cell after vibration testing [16]

For what concerns the internal resistance, an overall increasing trend was observed. In fact the tested cells showed an increase in internal resistance by 5-25% as compared to the new cells. The EIS Nyquist plot reported in figure 2.11 shows the increase of internal resistance and the behavior of the cell.

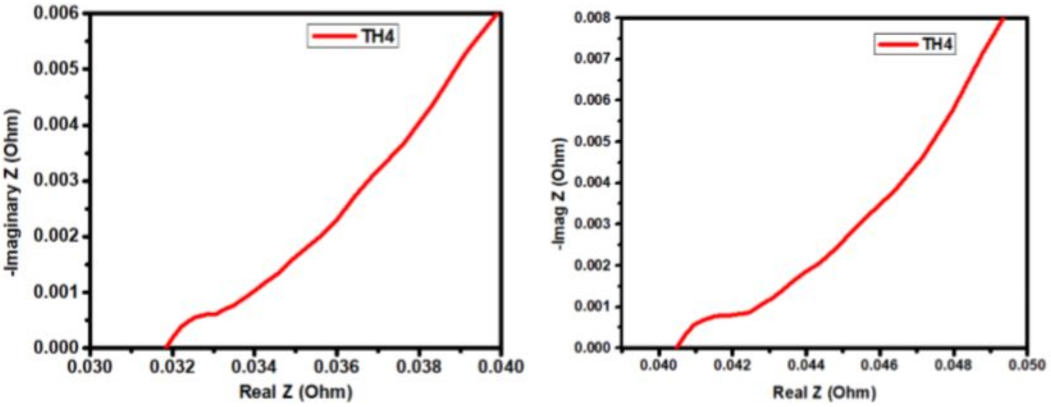

Figure 2.11: Nyquist Plot for New Cell (left) and Nyquist Plot for Cell tested after Vibration testing (right) [16]

The increase of internal resistance could be caused by the reduction of protective characteristic of the film formed on carbon electrode (SEI) during vibration. In fact, according to the authors, the heat generated by vibration could lead to evaporation of the electrolyte and damage of the film.
Moreover a voltage drop of 0.3-0.4 was detected after the vibration test, which leads to a severe capacity fade.
Furthermore a change in the dynamic properties was detected, as the first natural frequency, and consequently the dynamic stiffness, and the max amplitude increased after the the vibration test. The FRF of the new and the tested cells is reported in figure 2.12.
The dynamic stiffness measurements was carried out simply by means of an impact hammer and an accelerometer. The cells were mounted in the fixture in vertical direction, so only this direction was excited by the hammer and measured by the accelerometer.

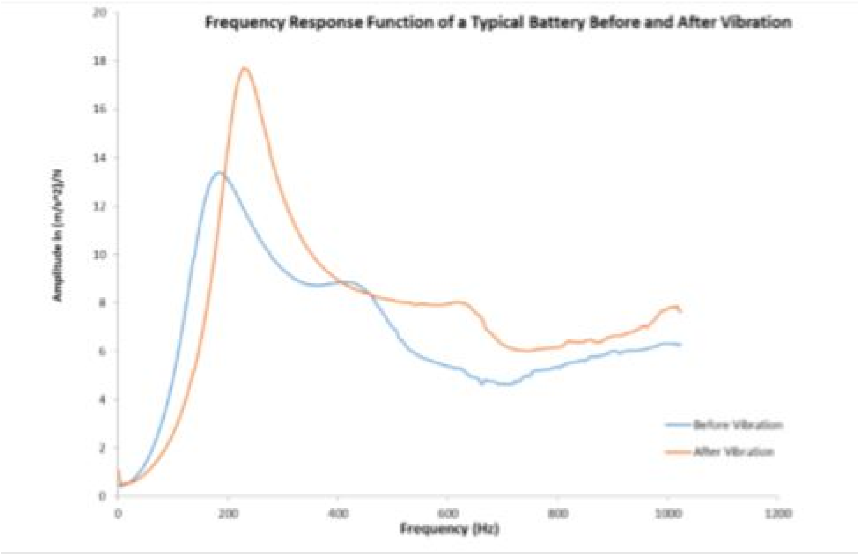

Figure 2.12: FRF curve for cell before and after vibration [material characterization]

In particular the resonance frequency was 172.5 Hz before test and became 239.3 Hz after the vibration test, i.e. 38% greater. According to the author, this effect could be related to the distributed mass of the cell components which was earlier acted as lumped mass before vibration.
Finally, according to the author, the cathode corrosion and a serious increase in the internal resistance can lead to decrease in useful cell capacity, since the lower voltage cut-off of the cell is reached sooner in a cell with higher internal resistance [16].

Chapter 3

Theoretical approach

In this section a mathematical model for the prediction of cell damaging is presented.
As mentioned in the introductory chapter, the lithium ion cell can be studied at different scales, this model refers to the particle level. So it describes the phenomena which occur in the particles of the electrodes.
The capacity reduction due to battery cycling, meant as charge/discharge, is universally accepted in literature. As a first approximation the capacity reduction is due to the formation of the SEI layer over the new free surfaces in the cracks of graphite particles. The cracks in the particles are generated by the stress in the graphite particle because of the lithium insertion or extraction. At the same manner the dynamic loads are supposed to generate an amount of stress in the particles and enhance the crack growing, making the capacity reduction effect more heavy.
So the aim of the model is to describe both the stress due to lithium ions insertion/extraction, the so called diffusion induced stress theory (DIF), the stress which arises from the dynamic load and how this two effects combines each other.

3.1 Diffusion induced stress theory

The stress in the graphite particles during charge and discharge cycles is a result of the chemical strain induced by the lithium ion concentration gradient within the particle. The presence of a concentration gradient is due to the slow diffusion of the ions within the graphite particles, and a constant concentration is not immediately established in the whole particle.
At the beginning of the charge, the lithium ions get into the particle causing a maximum surface concentration that decreases sharply towards the center of the particle. Then during the charging process the ions diffuse toward the center of the particle, so the concentration gradient fades and a uniform concentration value is established in the whole particle at the end of the charge.

The chemical strain, modeled by equation 3.1 [21], is proportional to the concentration gradient, according to the partial molar volume Ω of lithium in graphite.

$$\varepsilon_{ch} = \frac{\Omega}{3}\Delta C \tag{3.1}$$

The partial molar volume of a component is broadly the volume variation of a mixture due to the addition of a mole of solute. However the partial molar volume depends also on the solvent. In fact when one mole of water is added to a large volume of water the volume increases by $18cm^3$, but when a mole of water is added to a large volume of ethanol the volume of the mixture increases only by $14cm^3$. This means that the partial molar volume of water in water is $18cm^3mol^{-1}$ and the partial molar volume of water in ethanol is $14cm^3mol^{-1}$. So, the partial molar volume of a component in a mixture is the change in volume per mole of component added to the mixture.
For this reason the stress in the particle, generated by the chemical stress, depends on how the lithium ions diffuse and on the concentration profile which is established within the particle over time. Therefore the problem is an elastic-diffusive type.

The graphite particle is assumed to be spherical and an isotropic linear elastic solid. From the electrochemical point of view the current density (in galvanostatic control) and the maximum concentration (in potentiostatic control) are assumed to be uniform over the particle surface. These assumptions allow to deal with an axisymmetric monodimensional model, whose the only variable is the radius of the particle.

3.1.1 Diffusivity equation

The diffusion equation is derived according to a thermodynamic approach.
The driving force of mass transport is the gradient of chemical potential. The chemical potential of a solute in an ideal solution subjected to stress is written according to equation 3.2 [23,28,29].

$$\mu = \mu_0 + RTln(C) - \sigma_h \Omega \tag{3.2}$$

Where μ_0 is a constant, R the universal constant of gasses, C the concentration field, T the temperature, σ_h the hydrostatic stress experienced by the particle and Ω the partial molar volume.
The lithium flux due to the chemical potential along the radial direction is expressed as [28]:

$$J = -MC\frac{\partial \mu}{\partial r} \tag{3.3}$$

Where M is the mobility of the solute. Replacing the expression of chemical potential (equation 3.2) in the expression of lithium flux (equation 3.3), it gives:

$$J = -D\left(\frac{\partial C}{\partial r} - \frac{\Omega C}{RT}\frac{\partial \sigma_h}{\partial r}\right) \tag{3.4}$$

Where D is the diffusion coefficient defined as $D = MRT$, and remarking that $\frac{\partial(ln(C))}{\partial r} = \frac{1}{C}\frac{\partial C}{\partial r}$.
At this stage the mass conservation equation is introduced:

$$\frac{\partial C}{\partial t} + div(J) = 0 \tag{3.5}$$

Mass conservation in spherical coordinates is written as:

$$\begin{aligned} &\frac{\partial C}{\partial t} + \frac{1}{r^2}\frac{\partial (r^2 J)}{\partial r} = 0 \\ &\frac{\partial C}{\partial t} + \frac{2}{r}J + \frac{\partial J}{\partial r} = 0 \end{aligned} \tag{3.6}$$

Finally the definition of lithium flux (equation 3.4) is replaced in the last equation of 3.6, and the complete concentration equation is obtained:

$$\begin{aligned} &\frac{\partial C}{\partial t} - D\frac{2}{r}\left(\frac{\partial C}{\partial r} - \frac{\Omega C}{RT}\frac{\partial \sigma_h}{\partial r}\right) - D\frac{\partial^2 C}{\partial r^2} + \frac{D\Omega}{RT}\left(\frac{\partial C}{\partial r}\frac{\partial \sigma_h}{\partial r} + C\frac{\partial^2 \sigma_h}{\partial r^2}\right) = 0 \\ &\frac{\partial C}{\partial t} = D\left[\frac{\partial^2 C}{\partial r^2} + \frac{2}{r}\frac{\partial C}{\partial r} - \frac{\Omega}{RT}\frac{\partial C}{\partial r}\frac{\partial \sigma_h}{\partial r} - \frac{\Omega C}{RT}\left(\frac{\partial^2 \sigma_h}{\partial r^2} + \frac{2}{r}\frac{\partial \sigma_h}{\partial r}\right)\right] \end{aligned} \tag{3.7}$$

The concentration field is coupled with the hydrostatic stress according to equation 3.7. However the contribution of hydrostatic stress in chemical potential (equation 3.2) can be neglected as a first approximation. This lead to a slight variation in stress rate according to [29] in the "free surface" boundary condition explained later.

This simplification results in neglecting the last two terms of the complete concentration equation in the second line of 3.7. So, the so called diffusion equation is derived:

$$\frac{\partial C}{\partial t} = \frac{D}{r^2}\frac{\partial}{\partial r}\left(r^2\frac{\partial C}{\partial r}\right) \tag{3.8}$$

Where D is the diffusivity coefficient of lithium ions in the graphite particle.

In case of constant voltage control, also called potentiostatic control, the boundary conditions are given by a set of Dirichlet conditions [26]:

$$\begin{cases} C(r,0) = C_0, & \text{for } \ 0 \leq \text{r} \leq \text{R} \\ C(R,t) = C_R, & \text{for } \ \text{t} \geq 0 \\ C(0,t) = finite, & \text{for } \ \text{t} \geq 0 \end{cases} \tag{3.9}$$

In this section the solution of the problem expressed in equation 3.8-3.9 is presented according to the note on Sturm-Liouville problem reported in [24]. The partial differential equation 3.8 is solved by variable separation, which allows to derive an analytical solution for the aforementioned problem.

First of all the solution is splitted in two part, the first part gives the homogeneous solution, the second part the non homogeneous one:

$$C(r,t) = v(r,t) + C_R \tag{3.10}$$

The function $v(r,t)$ satisfies the differential equation 3.8, has a null derivative at the center of the sphere and vanishes on the surface.

Therefore $v(r,t)$ is written as the product of two functions, T and P by variable separation. The first function depends only on the time and the latter depends only on the radial coordinate.

$$v(r,t) = P(r)T(t) \tag{3.11}$$

Replacing the guessed form of $v(r,t)$ in the equation 3.8, the left hand side and the right hand side are reported in the first and in the second line of equation 3.12, accordingly.

$$\begin{aligned}&\frac{\partial C}{\partial t} = \frac{\partial [P(r)T(t)]}{\partial t} = P(r)\frac{\partial T(t)}{\partial t}\\ &\frac{D}{r^2}\frac{\partial}{\partial r}r^2\frac{\partial C}{\partial r} = \frac{D}{r^2}\frac{\partial}{\partial r}r^2\frac{\partial [P(r)T(t)]}{\partial r} = \frac{DT(t)}{r^2}\frac{\partial}{\partial r}r^2\frac{\partial P(r)}{\partial r}\end{aligned} \tag{3.12}$$

Then assembling equations 3.12 according to equation 3.8 and dividing by $DP(r)T(t)$, the expression in equation 3.13 is got.

$$\frac{1}{D}\frac{1}{T(t)}\frac{\partial T(t)}{\partial t} = \frac{1}{P(r)}\frac{1}{r^2}\frac{\partial}{\partial r}r^2\frac{\partial P(r)}{\partial r} = -\lambda^2 \tag{3.13}$$

Left hand side of equation 3.13 results as a function of time, and the right hand side depends only on the radial position. The only way that a function depending on time is equal to another function depending on space is that the two functions are equal to a constant. $-\lambda^2$ is the constant adopted because allows easier calculations later.
So the left hand side of 3.13 becomes $\frac{dT(t)}{dt} = -\lambda^2 DT(t)$ whose general solution is $T(t) = Ce^{-\lambda^2 Dt}$.
Instead the right hand side of 3.13 becomes:

$$\frac{d}{dr}r^2\frac{dP(r)}{dr} + \lambda^2 r^2 P(r) = 0 \tag{3.14}$$

A guess solution of equation 3.14 could be:

$$P(r) = A\frac{sin(\lambda r)}{r} + B\frac{cos(\lambda r)}{r} \tag{3.15}$$

The guess solution 3.15 is actually the real solution since replacing itself and its first derivative in equation 3.14 it gives zero.
The constant B of the solution 3.15 is set to zero, otherwise the solution would become infinite for $r = 0$. With this assumption the solution 3.15 remains finite at the center of the sphere, as prescribed by the condition 3.9.
So the total solution for $v(r,t)$ is:

$$v(r,t) = T(t)P(r) = ACe^{-\lambda^2 Dt}\frac{sin(\lambda r)}{r} = De^{-\lambda^2 Dt}\frac{sin(\lambda r)}{r} \tag{3.16}$$

The set of homogeneous condition and the form of the original differential equation makes the solution for $v(r,t)$ to be the solution of a Strum-Liouville problem. Accordingly, an infinite set of solutions for $v(r,t)$, that give a complete set of orthogonal eigenfunctions, is got. The solution of equation 3.16 has to respect the homogeneous condition on the sphere surface, which is:

$$v(R,t) = T(t)P(R) = De^{-\lambda^2 Dt}\frac{sin(\lambda R)}{R} = 0 \tag{3.17}$$

Equation 3.17 is true when $D = 0$, leading to a trivial solution, or when λR is an integer multiple of π. The last consideration leads to an eigenvalue solution:

$\lambda_n = n\pi/R$ for $n = 1, ..., \infty$. Thus the solution for $v(r,t)$ is an infinite set of orthogonal eigenfunctions given by an infinite set of eigenvalues, each of them multiplied by a different constant D_n. So the general solution for $C(r,t)$ is written as follows:

$$C(r,t) = \sum_{n=1}^{\infty} D_n e^{-\lambda^2 D t} \frac{sin(\lambda_n r)}{r} + C_R \tag{3.18}$$

At this stage just the initial condition is left to be satisfied. In general a variable initial condition can be taken into account: $C(r,0) = C_0(r)$ for $t = 0$. This condition replaced in equation 3.18 gives:

$$C_0(r) = \sum_{n=1}^{\infty} \frac{D_n}{r} sin\left(\frac{n\pi r}{R}\right) + C_R \tag{3.19}$$

The eigenfunctions $sin(\frac{n\pi r}{R})/r$ form a set of orthogonal eigenfunctions in the interval between zero and R, so the initial condition function is expanded in terms of these eigenfunctions.

The definition of orthogonal eigenfunctions $\Phi_i, i = 1, 2, 3, ...$ according to a certain weighting factor W in an interval (a, b) is the following:

$$\begin{aligned} &\int_a^b \Phi_n(x)\Phi_m(x)W(x)\,dx = 0 \text{ if } n \neq m, \\ &\int_a^b [\Phi_n(x)]^2 W(x)\,dx \neq 0 \text{ if } n = m, \end{aligned} \tag{3.20}$$

Then the coefficients of eigenfunction expansion of Sturm-Liouvill problem is got by using the orthogonality relationship for the integral of sine. Moreover the Sturm-Liouvill problem defined in equation 3.16 has a weighting factor of r^2, that must be used in the orthogonality integral. For this reason, both side of equation 3.19 are multiplied by $r^2 \frac{sin(\frac{m\pi r}{R})}{r}$, where m is another integer number, and then integrated from zero to R. This leads to:

$$\begin{aligned} \int_0^R [C_0(r) - C_R] r^2 \frac{sin(\frac{m\pi r}{R})}{r} dr &= \int_0^R \sum_{n=1}^{\infty} D_m r^2 \frac{sin(\frac{n\pi r}{R})}{r} \frac{sin(\frac{m\pi r}{R})}{r} dr \\ &= \sum_{n=1}^{\infty} \int_0^R D_m sin(\frac{m\pi r}{R}) sin(\frac{n\pi r}{R}) dr \\ &= D_m \int_0^R sin^2(\frac{m\pi r}{R}) \end{aligned} \tag{3.21}$$

The order of summation and integral is reversed in the second row of equation 3.21, since these operations can commute. Moreover, in the second row of equation 3.21, all the integrals in the summation vanish except for the one identified by $n = m$, thanks to the orthogonality of the of the function $sin(\frac{n\pi r}{r})$. Then solving for D_m and integrating $sin^2(\frac{m\pi r}{R})$ by part two times, it results:

$$D_m = \frac{\int_0^R r[c_0(r) - c_R] sin(\frac{m\pi r}{R}) dr}{\int_0^R sin^2(\frac{m\pi r}{R})} = \frac{2}{R} \int_0^R r[c_0(r) - c_R] sin\left(\frac{m\pi r}{R}\right) dr \tag{3.22}$$

Thus the initial concentration is defined as $c_0(r) = C_0$, leaving the general initial condition for the one prescribed by the set of boundary condition expressed in equation 3.9. So D_m has the following expression:

$$\begin{aligned} D_m &= \frac{2}{R}\int_0^R r[C_0 - C_R] sin\left(\frac{m\pi r}{R}\right)dr = \frac{2[C_0 - C_R]}{R}\int_0^R r sin\left(\frac{m\pi r}{R}\right)dr = \\ &= \frac{2[C_0 - C_R]}{R}\left(\frac{R}{m\pi}\right)^2\left[sin(\frac{m\pi r}{R}) - \frac{m\pi r}{R}cos(\frac{m\pi r}{R})\right]_0^R = \\ &= -\frac{2R[C_0 - C_R]cos(m\pi)}{(m\pi)} \end{aligned} \tag{3.23}$$

The sign of $cos(m\pi)$ changes according to the the integer m: if m is even it is minus, if is odd it is plus. So the final result for D_m is written as:

$$D_m = -\frac{2R[C_0 - C_R](-1)^{m+1}}{(m\pi)} \tag{3.24}$$

Then the expression of D_m reported in equation 3.24 is substituted in equation 3.18 in order to get the concentration expression reported in equation 3.25.

$$\begin{aligned} &C(r,t) = -\frac{2R[C_0 - C_R]}{\pi}\sum_{m=1}^{\infty}\frac{(-1)^{m+1}}{m}e^{-\lambda_n^2 Dt}\frac{sin(\lambda_n r)}{r} + C_R \\ &\frac{C(r,t) - C_R}{C_0 - C_R} = -2\sum_{n=1}^{\infty}\frac{(-1)^{n+1}}{n\pi\frac{r}{R}}e^{-\frac{(n\pi)^2 Dt}{R^2}}sin\left(\frac{n\pi r}{R}\right) \\ &\text{with } \lambda_n = \frac{n\pi}{R},\ n = 1, ..., \infty \end{aligned} \tag{3.25}$$

Finally the second expression in equation 3.25 is rearranged in order to obtain some dimensionless coefficients.
Left hand side of equation 3.25 is the dimensionless concentration, normalized with the initial and boundary conditions. Then also the radial position is normalized with the dimensionless position $x = r/R$ and the dimensionless group $\tau = Dt/R^2$ is the time constant.
Finally, equation 3.25 is expressed as a function of the aforementioned dimensionless coefficients and rewritten as:

$$\frac{C(r,t) - C_R}{C_0 - C_R} = -2\sum_{n=1}^{\infty}\frac{(-1)^{n+1}}{\pi n x}\,sin(n\pi x)\,e^{-n^2\pi^2\tau} \tag{3.26}$$

The dimensionless coefficient τ represents the "diffusion time", when τ is small the diffusion process is at the beginning and the lithium ions concentration drops quickly away from the surface. When τ is large the lithium ions have more time to diffuse towards the center of the particle and the concentration gradient is smoother.
The time coefficient depend on $1/R^2$ because a greater radius makes the diffusion process longer, and it is directly proportional to the diffusion coefficient because larger is the value, faster is the diffusion of the ions toward the center of the particle.

Equation 3.26 is plotted in figure 3.1 in case of insertion, which provides a null initial concentration ($C_0 = 0$), and with a surface concentration equals to $2.29\,10^{-2} mol/cm^3$ [25].

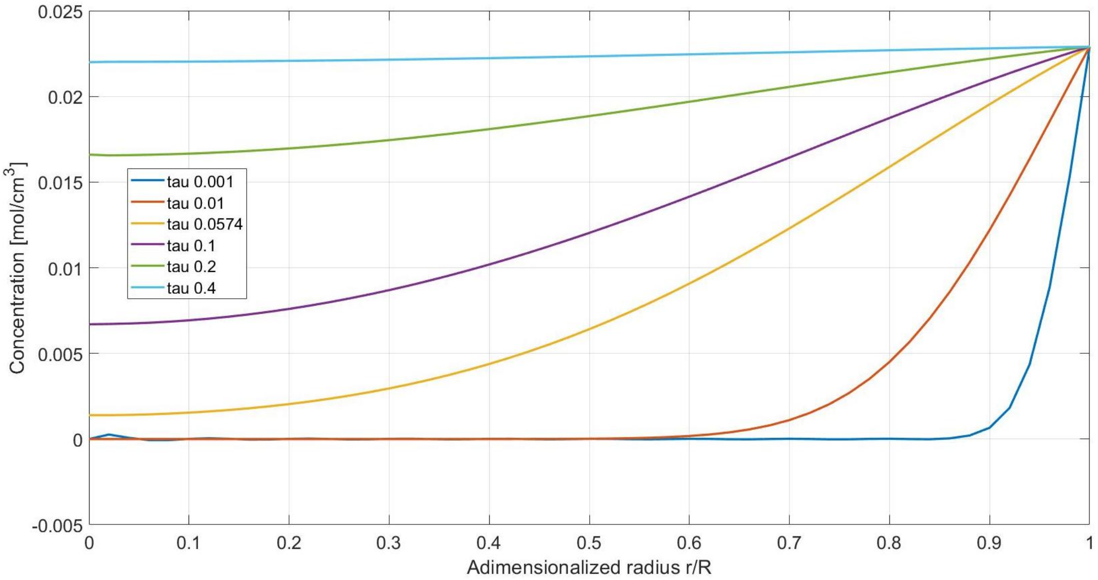

Figure 3.1: Concentration profile with potentiostatic control in lithiation

Therefor equation 3.26 describes the concentration profile in delithiation tuning the initial condition equals to the concentration at the end of lithiation, i.e. the maximum concentration which can be achieved in graphite particle ($C_0 = C_{max}$). Instead, the concentration at $r = R$ is set to zero, since the lithium ions are extracted from the surface. The concentration profile in this configuration is plotted in figure 3.2.

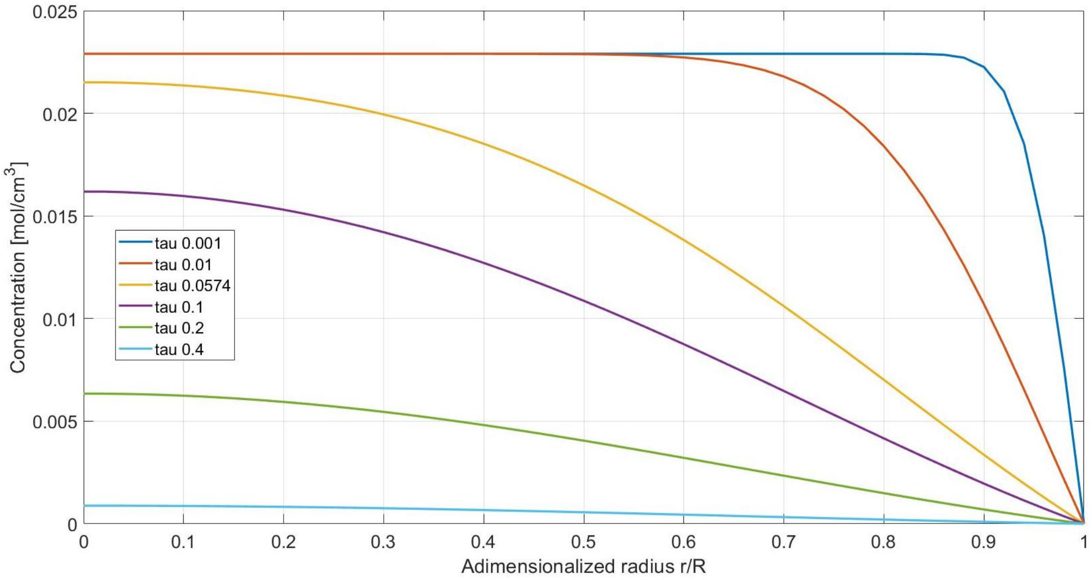

Figure 3.2: Concentration profile with potentiostatic control in delithiation

In case of constant current operation, the so called galvanostatic control, the boundary conditions are expressed in equation 3.27 [26].

$$\begin{cases} C(r,0) = C_0, & \text{for } 0 \leq \text{r} \leq \text{R} \\ \left.\frac{\partial C(r,t)}{\partial r}\right|_{r=R} = \frac{I}{FD}, & \text{for } \text{t} \geq 0 \\ \left.\frac{\partial C(r,t)}{\partial r}\right|_{r=0} = 0, & \text{for } \text{t} \geq 0 \end{cases} \tag{3.27}$$

Where R is the radius of the particle, F the Faraday constant and C_0 is the initial concentration within the particle.

This type of boundary condition modify deeply the solution research process [26]. Now the solution has the following shape:

$$C(r,t) = v(r,t) + w(r) + \phi(t) \tag{3.28}$$

Where the function $v(r,t)$ supplies the solution with homogeneous gradient at the boundary and the function $w(r)$ supplies the non homogeneous gradient at the boundary, in fact $\left.\frac{\partial w}{\partial r}\right|_{r=0} = 0$ and $\left.\frac{\partial w}{\partial r}\right|_{r=R} = \frac{I}{FD}$. Finally the function $\phi(t)$ takes into account the long term solution. Therefor the shape of the solution presented in equation 3.28 is replaced in the equation which governs the concentration profile in spherical coordinated (equation 3.8):

$$\begin{aligned} &\frac{\partial v}{\partial t} + \frac{\partial \phi}{\partial t} - \frac{D}{r^2}\frac{\partial}{\partial r}\left[r^2\left(\frac{\partial v}{\partial r} + \frac{\partial w}{\partial r}\right)\right] = 0 \\ &\frac{\partial v}{\partial t} + \frac{\partial \phi}{\partial t} - \frac{D}{r^2}\left[2r\left(\frac{\partial v}{\partial r} + \frac{\partial w}{\partial r}\right) + r^2\left(\frac{\partial^2 v}{\partial r^2} + \frac{\partial^2 w}{\partial r^2}\right)\right] = 0 \\ &\frac{\partial v}{\partial t} + \frac{\partial \phi}{\partial t} - \frac{2D}{r}\frac{\partial v}{\partial r} - \frac{2D}{r}\frac{\partial w}{\partial r} - D\frac{\partial^2 v}{\partial r^2} D\frac{\partial^2 w}{\partial r^2} = 0 \end{aligned} \tag{3.29}$$

Since $v(r,t)$ satisfies the diffusion equation it holds: $\frac{\partial v}{\partial t} - \frac{2D}{r}\frac{\partial v}{\partial r} - D\frac{\partial^2 v}{\partial r^2} = 0$ which allows to eliminates these term from the last row of equation 3.29, which becomes:

$$\frac{\partial \phi}{\partial t} = \frac{2D}{r}\frac{\partial w}{\partial r} + D\frac{\partial^2 w}{\partial r^2} = A \tag{3.30}$$

Left hand side of equation 3.30 is just a function of time, and right hand side depends only on the space. The only way that this could be true is if both are equal to a constant A. So equation 3.30 is rewritten separating the variables.

$$\begin{cases} \frac{\partial \phi}{\partial t} = A \\ \frac{2D}{r}\frac{\partial w}{\partial r} + D\frac{\partial^2 w}{\partial r^2} = A \end{cases} \tag{3.31}$$

Thus the second line of equation 3.31 is integrated twice in order to get the expression of $w(r)$. Multiplying by r and integrating from zero to R it gives:

$$\begin{aligned} &\int_0^R r\frac{\partial^2 w}{\partial r^2}dr + 2\int_0^R \frac{\partial w}{\partial r}dr = \frac{A}{D}\int_0^R r\,dr \\ &2w + \left[\int_0^R \frac{\partial^2 w}{\partial r^2}dr\,r - \int_0^R\left(\int_0^R \frac{\partial^2 w}{\partial r^2}dr\,1\right)dr\right] = \frac{A}{D}\frac{r^2}{2} + C_1 \\ &2w + \frac{\partial w}{\partial r}r - w = \frac{A}{D}\frac{r^2}{2} + C_1 = \frac{\partial w}{\partial r}r + w = \frac{A}{D}\frac{r^2}{2} + C_1 \end{aligned} \tag{3.32}$$

Then a second integration leads to:

$$\begin{aligned}
&\int_0^R \left(\frac{\partial w}{\partial r} r + w\right) dr = \int_0^R \left(\frac{A}{D}\frac{r^2}{2} + C_1\right) dr \\
&wr - \int_0^R w\, dr + \int_0^R w\, dr = \frac{A}{D}\frac{r^3}{6} + C_1 r + C_2
\end{aligned} \tag{3.33}$$

At this stage the function $w(r)$ is simply obtained dividing dividing by r, and the function ϕ is derived by the integration of the first equation in system 3.31.

$$\begin{cases} \phi(t) = At + B \\ w(r) = \frac{A}{D}\frac{r^2}{6} + C_1 + \frac{C_2}{r} \end{cases} \tag{3.34}$$

Finally the constant A and C_2 are determined according to the Neumann boundary condition.

$$\begin{aligned}
&\left.\frac{\partial w}{\partial r}\right|_{r=0} = \left.\left(\frac{A}{D}\frac{r}{3} - \frac{2}{r^2}C_2\right)\right|_{r=0} = 0 \\
&C_2 = 0 \\
&\left.\frac{\partial w}{\partial r}\right|_{r=R} = \left.\left(\frac{A}{D}\frac{r}{3}\right)\right|_{r=R} = \frac{I}{FD} \\
&A = \frac{3I}{RF}
\end{aligned} \tag{3.35}$$

Therefore the function w and ϕ have the following expression:

$$\begin{cases} \phi(t) = \frac{3I}{RF} t + B \\ w(r) = \frac{I}{RFD}\frac{r^2}{2} + C_1 \end{cases} \tag{3.36}$$

Thus the attention is shifted on the expression of v, which satisfies the diffusion equation with zero gradient boundary condition. v is splitted in a function of time and a function of space, as done before: $v(r,t) = P(r)T(t)$. Since v satisfies the diffusion equation the expression of $v(r,t)$ is replaced in equation 3.8 leading to:

$$\begin{cases} \frac{dT}{dt} = -\lambda^2 D T(t) \\ \frac{d}{dr} r^2 \frac{dP(r)}{dr} + \lambda^2 r^2 P(R) = 0 \end{cases} \tag{3.37}$$

The solution of 3.37 are reported in equation 3.38.

$$\begin{cases} T = Ce^{-\lambda^2 D t} \\ P(r) = A\frac{sin(\lambda r)}{r} + B\frac{cos(\lambda r)}{r} \end{cases} \tag{3.38}$$

Since the solution has to be finite for $r = 0$ the constant B in equation 3.38 is set to zero. Therefore the final solution for v is

$$v(r,t) = Ke^{-\lambda^2 D t}\frac{sin(\lambda r)}{r} \tag{3.39}$$

Then the homogeneous Neumann condition for $r = R$ gives:

$$\begin{aligned} \left.\frac{\partial v}{\partial r}\right|_{r=R} &= Ke^{-\lambda^2 Dt}\left[\frac{\lambda cos(\lambda R)}{R} - \frac{sin(\lambda R)}{R^2}\right] = 0 \\ \lambda cos(\lambda R) &= \frac{sin(\lambda R)}{R} \\ \lambda &= \frac{tg(\lambda R)}{R} \end{aligned} \tag{3.40}$$

The first line of equation 3.40 is true when $K = 0$, but this condition leads to a trivial solution, or when the term in the parenthesis vanishes. This last condition, reported in the second row of equation 3.40, defines the eigenvalues λ_n of the solution of this problem, which are computed as the roots of the transcendent equation reported in the third line of equation 3.40.
This last equation can not be solved analytically. Referring to figure 3.3 it is solved in a graphic way, plotting the function x and $\frac{tg(xR)}{R}$, where R is a constant, and looking for the intersections.

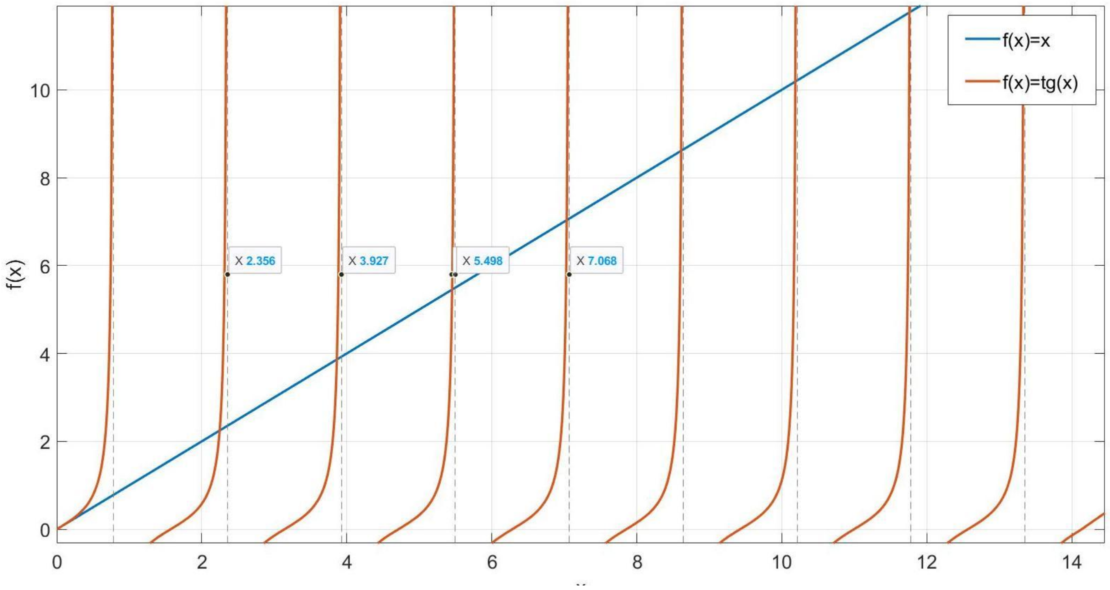

Figure 3.3: Graphic solution of the transcendent equation $\lambda = \frac{tg(\lambda R)}{R}$

A known approximation of the roots of the transcendent equation $x = tg(x)$, namely the values of the asymptotes, is given by $x \simeq (2n + 1)\pi/2$. This approximation is a little rough for the first values, but then it becomes quite accurate, as can be seen from figure 3.3. Therefore the aforementioned approximation is modified in 3.41 in order to get an analytical approximated solution of the equation reported in the third line of 3.40.

$$\lambda_n \simeq \frac{\frac{2n+1}{R}\pi}{2} \tag{3.41}$$

Finally the solution for v is the one which takes into account all the eigenvalues of the solution:

$$
\begin{aligned}
v(r,t) &= K_0 + \sum_{n=1}^{\infty} K_n e^{-\lambda_n^2 D t} \frac{sin(\lambda_n r)}{r} \\
v(r,t) &= K_0 + \sum_{n=1}^{\infty} K_n e^{-\lambda_n^2 D t} \frac{sin(\frac{2n+1}{2R}\pi \, r)}{r}
\end{aligned}
\tag{3.42}
$$

At this stage the whole solution is assembled and the coefficients K_n are determined by the usual eigenfunction expansion.

$$
\begin{aligned}
C(r,t) &= v(r,t) + w(r) + \phi(t) = \\
&= K_0 + \sum_{n=1}^{\infty} K_n e^{-\lambda_n^2 D t} \frac{sin(\lambda_n r)}{r} + \frac{A}{D}\frac{r^2}{6} + C_1 + \frac{C_2}{r} + At + B
\end{aligned}
\tag{3.43}
$$

With this type of equation a separate integration between $n = 0$ and the other value is needed because of the different normalization constant. So the value of K_0 is calculated in 3.44 from equation 3.43 imposing $t = 0$ with an unitary normalization constant.

$$
\int_0^R \left[C_0 - \frac{Ar^2}{6D} - C_1 - B \right] 1 \, dr = \int_0^R K_0 1 \, dr \tag{3.44}
$$

Then the eigenfunction expansion is applied for the other values of n in equation 3.43 with a weighting factor equals to r^2. So both side of equation are multiplied for $r^2 \frac{sin(\lambda_m r)}{r}$ and integrated from 0 to R.

$$
\int_0^R \left[C_0 - \frac{Ar^2}{6D} - C_1 - B \right] r^2 \frac{sin(\lambda_m r)}{r} \, dr = \int_0^R \sum_{n=1}^{\infty} K_n \frac{sin(\lambda_n r)}{r} \, r^2 \frac{sin(\lambda_m r)}{r} \, dr \tag{3.45}
$$

As in the case of Dirichlet condition, all the integrals in the summation in the right hand side of equation 3.45 vanish except for the one with $n = m$ thanks to the orthogonality of the function respect to the chosen weighting factor.
Thus the solution for $C(r,t)$ in case of galvanostatic control is derived solving equation 3.44 and 3.45 for K_0 and K_n, and taking into consideration the constants defined earlier.
At this stage all the constant are defined and the solution of the concentration function in galvanostatic operation is reported in equation 3.46.

$$
C(r,t) = C_0 + \frac{IR}{FD}\left[3\tau + \frac{x^2}{2} - \frac{3}{10} - \frac{2}{x} \sum_{n=1}^{\infty} \left(\frac{sin(\lambda_n x)}{\lambda_n^2 sin(\lambda_n)} e^{-\lambda_n^2 \tau} \right) \right] \tag{3.46}
$$

Where λ_n are the positive roots of $\lambda_n = tan(\lambda_n R)/R$ for $n \in$ N and x is the dimensionless radial position $x = r/R$.

Equation 3.46 is plotted in figure 3.4 in case of insertion. In this operation the inital condition is set to $C_0 = 0$ since there are not lithium ions in the particle.

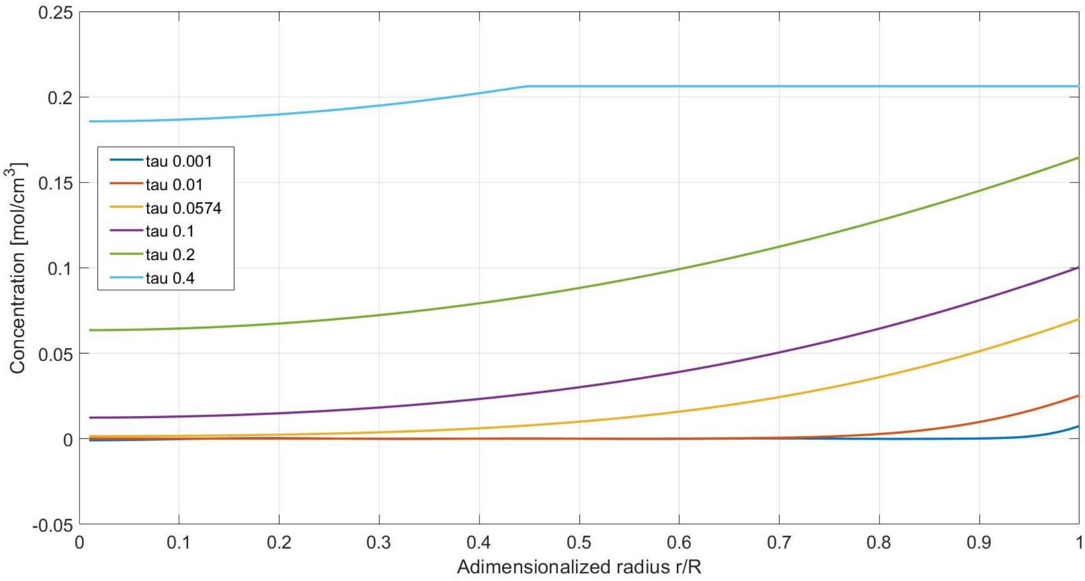

Figure 3.4: Concentration profile with galvanostatic control in lithiation

Instead $C_0 = C_{max}$ in delithiation, which means that the particle is considered totally charged. C_{max} is the maximum concentration value reached at the end of the lithiation. The concentration profile in extraction is reported in figure 3.5.

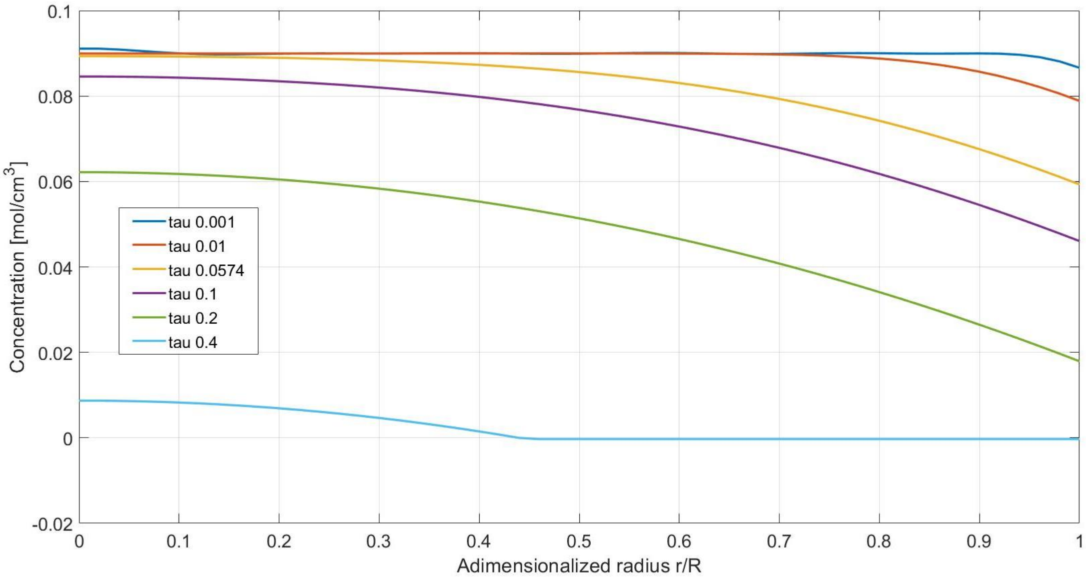

Figure 3.5: Concentration profile with galvanostatic control in delithiation

Then the dependence of the concentration profile on some characteristic values, such as the time of charging/discharging, the current rate and the radius of the particle is analyzed. For sake of simplicity just insertion with galvanostatic control is considered.

At first a set of different current rate is chosen, in order to identify its dependence on the concentration profile. The results are plotted in figure 3.6.

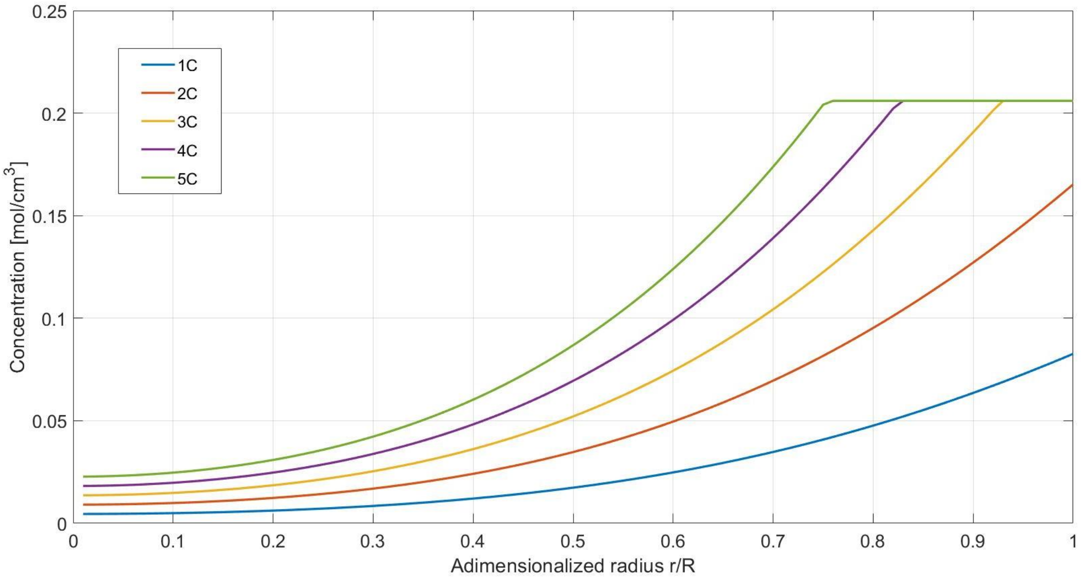

Figure 3.6: Concentration profile in galvanostatic insertion for different current rate at 600s

Figure 3.6 shows how an higher current rate enhances a faster diffusion of the lithium ions inside the particle, as a result of the higher current flux applied as a Neumann boundary condition on the surface. The concentration profiles for great current rate values are flat close to the surface because the maximum concentration is reached even at short time.
Therefor, the evolution of the concentration profile with time is analyzed assuming a current rate equals to 1C. The results are plotted in figure 3.7.

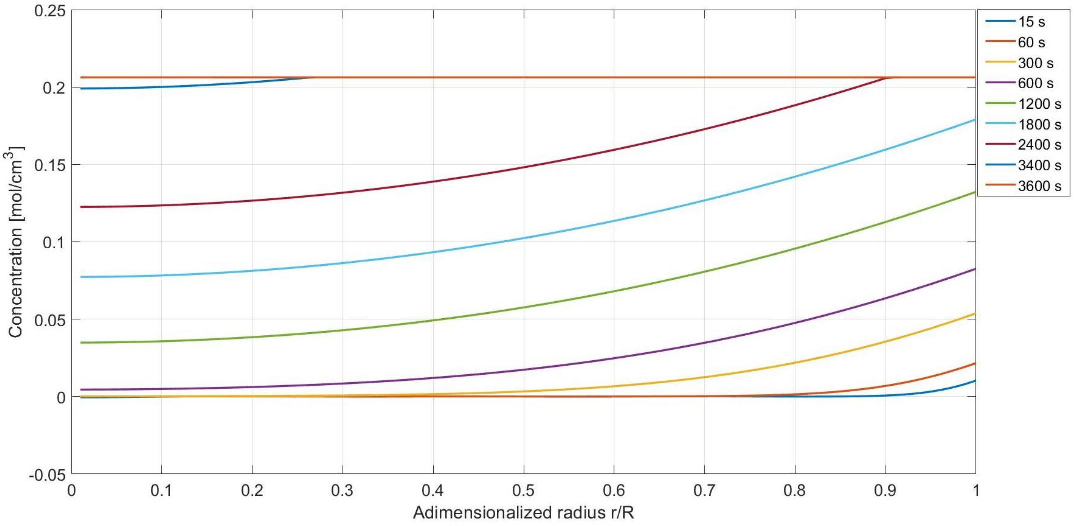

Figure 3.7: Time dependence of the concentration profile in galvanostatic insertion with 1C current rate

Figure 3.7 shows how the lithium ion diffuses within the particle. At the beginning of the insertion the ions are present just in the areas close to surface,

then slowly diffuse toward the center.Thus after one hour the concentration profile is flat equals to the maximum concentration, because that is the time necessary to charge completely a cell with a current rate equals to 1C.
Finally different particle sizes, meant as different radius, are analyzed in figure 3.8.

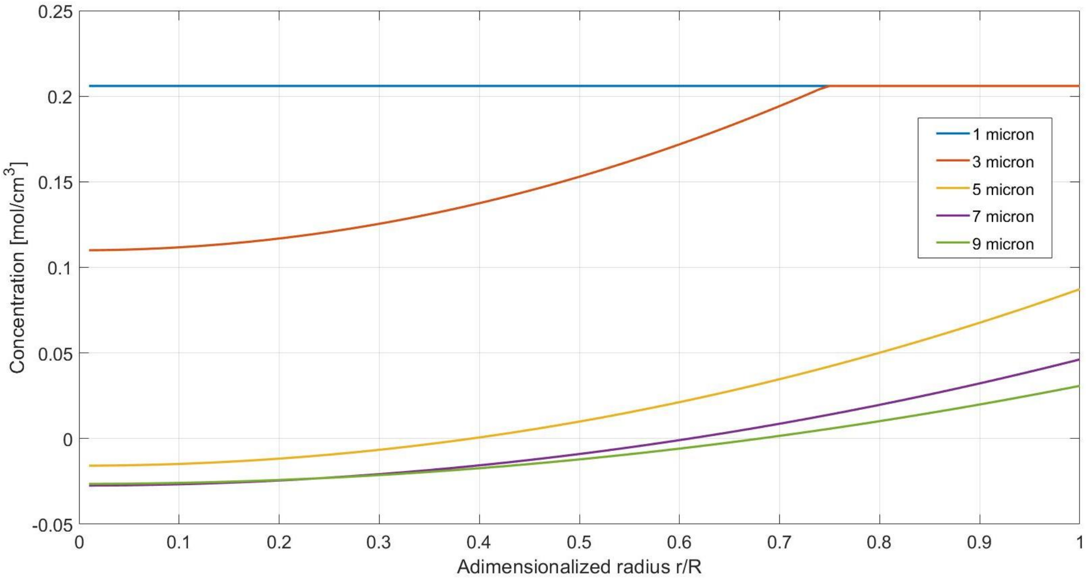

Figure 3.8: Concentration profile in galvanostatic insertion for different current rate at 600s

The results highlight how a smaller particle radius allows to reach a constant concentration gradient faster because the diffusion path is shorter. This results in a lower stress rate for particles with reduced size.

3.1.2 Elastic problem

The stress within a spherical domain is modeled with the set of equation 3.47-3.49. The first one is the equilibrium equation over a spherical domain. The second one are the constitutive equations, where the subscripts r and c refer to radial and circumferential. It is worth to emphasize that the chemical strain is added in right side of the equation in analogy to the thermal deformation. The third set of equations are the congruence ones.

$$\frac{d\sigma_r}{dr} + \frac{2}{r}\Bigg(\sigma_r - \sigma_c\Bigg) = 0 \tag{3.47}$$

$$\begin{cases} \varepsilon_r = \frac{1}{E}\Bigg(\sigma_r - 2\nu\sigma_c\Bigg) + \frac{\Omega C}{3} \\ \\ \varepsilon_c = \frac{1}{E}\Bigg[\sigma_c - \nu(\sigma_r + \sigma_c)\Bigg] + \frac{\Omega C}{3} \end{cases} \tag{3.48}$$

$$\begin{cases} \varepsilon_r = \frac{du}{dr} \\ \\ \varepsilon_c = \frac{u}{r} \end{cases} \tag{3.49}$$

Therfore the set of equations 3.49 are replaced in the set of equations 3.48, and then this result in equation 3.47. In this way a second order differential equation in the displacements is obtained (equation 3.50).

$$\frac{d^2u}{dr^2} + \frac{2}{r}\frac{du}{dr} - \frac{2u}{r^2} = \frac{1+\nu}{1-\nu}\frac{\Omega}{3}\frac{dC}{dr} \tag{3.50}$$

The displacement field is obtained by the integration of 3.50.
Considering the integration by part:

$$\int_0^r \frac{2}{r}\frac{du}{dr}\, dr = \frac{2u}{r} + \int_0^r \frac{2u}{r^2}\, dr \tag{3.51}$$

A first integration leads to:

$$\frac{du}{dr} + \frac{2u}{r} + \int_0^r \frac{2u}{r^2}\, dr - \int_0^r \frac{2u}{r^2}\, dr = \frac{1+\nu}{1-\nu}\frac{\Omega}{3}C(r) + C_1 \tag{3.52}$$

Then multiplying by r^2 and integrating it leads to:

$$\int_0^r r^2\frac{du}{dr}\, dr + 2\int_0^r ru\, dr = \frac{1+\nu}{1-\nu}\frac{\Omega}{3}\int_0^r r^2C(r)\, dr + \int_0^r C_1r^2\, dr \tag{3.53}$$

Then considering the integration by part:

$$\int_0^r r^2\frac{du}{dr} = r^2u - 2\int_0^r ru\, dr \tag{3.54}$$

and replacing it in equation 3.53 it results:

$$r^2u - 2\int_0^r ru\, dr + 2\int_0^r ru\, dr = \frac{1+\nu}{1-\nu}\frac{\Omega}{3}\int_0^r r^2C(r)\, dr + \int_0^r C_1r^2\, dr \tag{3.55}$$

Finally computing the integrations and dividing by r^2 the final expression 3.56 is got:

$$u(r) = \frac{1+\nu}{1-\nu}\frac{\Omega}{3}\frac{1}{r^2}\int_0^r C(r)r^2\, dr + \frac{C_1}{3}r + \frac{C_2}{r} \tag{3.56}$$

The constants C_1 and C_2 are obtained imposing the desired boundary condition. Null displacement at the centre of the sphere is the first condition which leads to $C_2 = 0$. This result is obtained solving $\lim_{r\to 0} u(r)$, since the equation 3.56 is not defined for $r = 0$.
The second condition can be derived for two different surface condition: free surface or constrained surface. The first condition is related to the free expansion of the particle, the second one takes into consideration the interaction with other particles, and free expansion is no longer allowed.

Free surface condition is verified when the radial stress vanishes on the surface of the sphere. The expression of the radial stress (equation 3.57) is obtained from the set of constitutive equations 3.48.

$$\sigma_r = \frac{E\left[\left(\varepsilon_r - \frac{1}{3}\Omega C(r)\right)(1-\nu) + 2\nu\left(\varepsilon_c - \frac{1}{3}\Omega C(r)\right)\right]}{(1+\nu)(1-2\nu)} \tag{3.57}$$

Then the set of congruence equations is substituted in 3.57 obtaining equation 3.58 which depends only on the displacement field.

$$\sigma_r = \frac{E\left[\left(\frac{du}{dr} - \frac{1}{3}\Omega C(r)\right)(1-\nu) + 2\nu\left(\frac{u(r)}{r} - \frac{1}{3}\Omega C(r)\right)\right]}{(1+\nu)(1-2\nu)} \tag{3.58}$$

So the expression 3.53 is valued for $\sigma_r = 0$ at $r = R$, obtaining equation 3.59.

$$\left(\left.\frac{du}{dr}\right|_{r=R} - \frac{1}{3}\Omega C(r)\right)(1-\nu) + 2\nu\left(\frac{u(R)}{R} - \frac{1}{3}\Omega C(r)\right) = 0 \tag{3.59}$$

Then the expression of the displacement field and its derivative valued of $r = R$ are reported in the first and second line of equation 3.60.

$$\begin{aligned} u(R) &= \int_0^R C(r)r^2\,dr + \frac{C_1 R}{3} \\ \left.\frac{du}{dr}\right|_{r=R} &= \frac{1+\nu}{1-\nu}\frac{\Omega}{3}\left(-\frac{2}{r^3}\int_0^r C(r)r^2\,dr + \frac{1}{r^2}C(r)r^2\right) + \frac{C_1}{3} \end{aligned} \tag{3.60}$$

At this stage the results in equation 3.60 are replaced in equation 3.59, which is solved for C_1 giving equation 3.61.

$$C_1 = 2\frac{1-2\nu}{1-\nu}\frac{\Omega}{R^3}\int_0^R C(r)r^2 dr \tag{3.61}$$

Finally, substituting the expression of C_1 in the equation 3.50, the displacement field reported in equation 3.62 is got.

$$u(r) = \frac{\Omega}{3(1-\nu)}\left[(1+\nu)\frac{1}{r^2}\int_0^r C(r)r^2\,dr + 2(1-2\nu)\frac{r}{R^3}\int_0^R C(r)r^2\,dr\right] \tag{3.62}$$

The shape of the displacement still depends on the concentration profile. The displacement function associated to the concentration profile given by the potentiostatic insertion at $\tau = 0.0574$ is showed in figure 3.9. The time constant $\tau = 0.0574$ causes the maximum radial stress, so it is taken as reference.

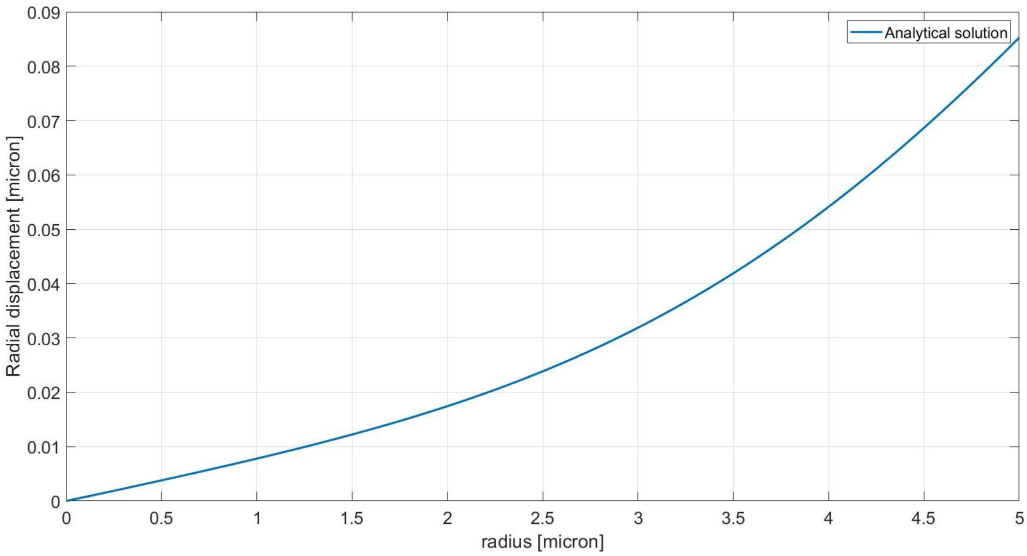

Figure 3.9: Radial displacement due to potentiostatic insertion at $\tau = 0.0574$ with free surface boundary condition

Table 3.1: Material proprieties (Graphite)

Parameter	Symbol	Unit	Value
Young Modulus	E	GPa	15
Poisson ration	ν		0.3
Fraction molar volume	Ω	m^3/mol	$3.497\,10^{-6}$
Maximum concentration	C_{max}	mol/m^3	$2.29\,10^{4}$

Once the expression of the displacements is obtained, the expressions of strain (equation 3.63) and stress (equation 3.64) are obtained. Strain equations are obtained replacing the displacement field (equation 3.62) in the congruence equations (3.49). Therefore the stress equations are obtained replacing the strain equations just derived in the constitutive ones (equation 3.48).

$$\begin{cases} \varepsilon_r = \frac{1+\nu}{1-\nu}\frac{\Omega}{3}\left[-\frac{2}{r^3}\int_0^r C(r)r^2\,dr + C(r)\right] + \frac{2\Omega}{3}\frac{1-2\nu}{1-\nu}\frac{1}{R^3}\int_0^R C(r)r^2\,dr \\ \\ \varepsilon_c = \frac{1+\nu}{1-\nu}\frac{\Omega}{3}\frac{1}{r^3}\int_0^r C(r)r^2\,dr + \frac{2}{3}\Omega\frac{1-2\nu}{1-\nu}\frac{1}{R^3}\int_0^R C(r)r^2\,dr \end{cases} \tag{3.63}$$

$$\begin{cases} \sigma_r = \frac{2\Omega}{3}\frac{E}{1-\nu}\left[\frac{1}{R^3}\int_0^R C(r)r^2\,dr - \frac{1}{r^3}\int_0^r C(r)r^2\,dr\right] \\ \\ \sigma_c = \frac{\Omega}{3}\frac{E}{1-\nu}\left[\frac{2}{R^3}\int_0^R C(r)r^2\,dr + \frac{1}{r^3}\int_0^r C(r)r^2\,dr - C(r)\right] \end{cases} \tag{3.64}$$

The expressions just derived for displacement, strains and stresses (equations 3.62-3.64) have a singularity for $r = 0$ which has to analyzed separately.
The displacement function is forced to be zero at $r = 0$, on the contrary the stresses and strains functions does not have a specific value prescribed by the boundary

conditions at the center of the sphere. For this reason the limit of the radial and hoop stress for r tending to zero has been computed.

$$\lim_{r\to 0}\sigma_r = \frac{2\Omega}{3}\frac{E}{1-\nu}\left[\frac{1}{R^3}\int_0^R C(r)r^2\,dr - \frac{1}{r^3}\int_0^r C(r)r^2\,dr\right] \tag{3.65}$$

The first integral is constant with the radius, so it remains finite at $r = 0$, on the other hand the second integral is not defined at $r = 0$. The function $C(r)$ can be assumed as a constant for $r = 0$ equals to $C(r = 0)$ and is taken out from the integral. The integral computed in this way gives:

$$\frac{C(r=0)}{r^3}\int_0^r r^2\,dr = \frac{C(r=0)}{r^3}\frac{r^3}{3} = \frac{C(r=0)}{3} \tag{3.66}$$

Finally the value of the radial stress at the center of the sphere is:

$$\sigma_r(r=0) = \frac{2\Omega}{3}\frac{E}{1-\nu}\left[\frac{1}{R^3}\int_0^R C(r)r^2\,dr - \frac{C(r=0)}{3}\right] \tag{3.67}$$

At the same manner the value of the hoop stress at the center of the sphere is computed.

$$\lim_{r\to 0}\sigma_c = \frac{\Omega}{3}\frac{E}{1-\nu}\left[\frac{2}{R^3}\int_0^R C(r)r^2\,dr + \frac{1}{r^3}\int_0^r C(r)r^2\,dr - C(r)\right] \tag{3.68}$$

Then assuming $C(r) = C(r = 0)$, which can be taken out from the integral, and computing the integral, the final expression is got:

$$\sigma_c(r=0) = \frac{\Omega}{3}\frac{E}{1-\nu}\left[\frac{2}{R^3}\int_0^R C(r)r^2\,dr - \frac{2}{3}C(r)\right] \tag{3.69}$$

Finally the shape of the radial and circumferential stress are reported in figure 3.10 and 3.11 with the same concentration profile of the displacement of figure 3.9.

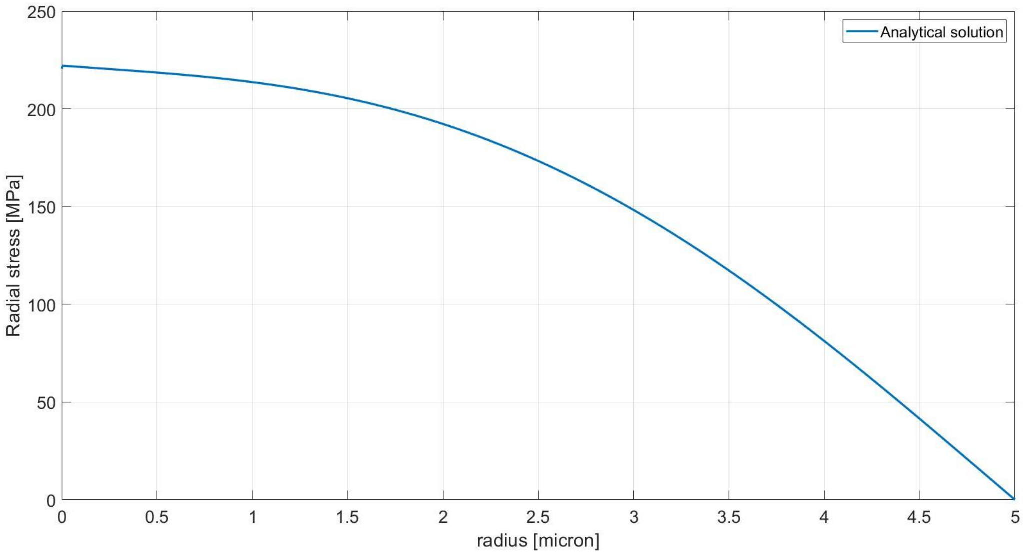

Figure 3.10: Radial stress due to potentiostatic insertion at $\tau = 0.0574$ with free surface boundary condition

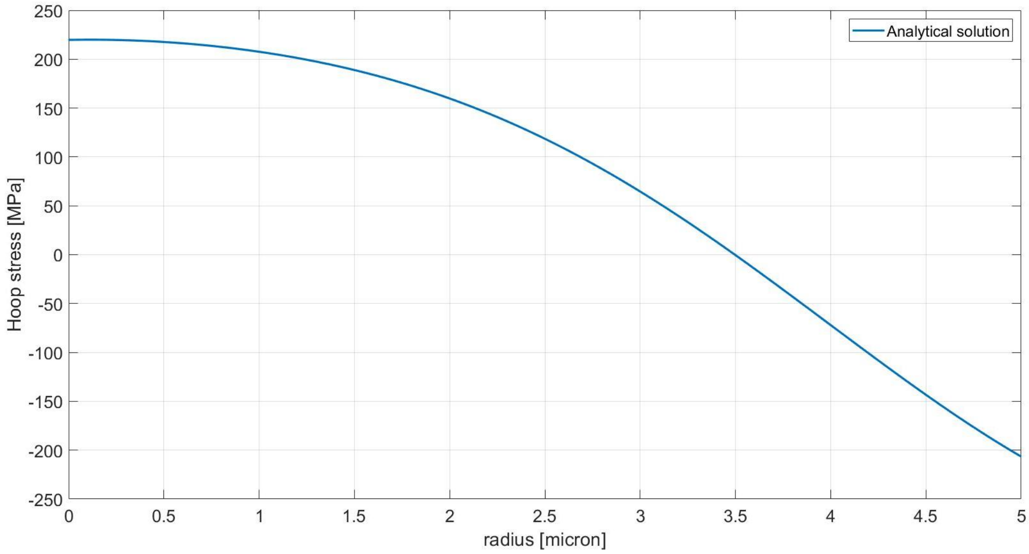

Figure 3.11: Circumferential stress due to potentiostatic insertion at $\tau = 0.0574$ with free surface boundary condition

Therefore it could be interesting to simulate a constrained surface condition, since the particle is not free to expand during lithiation because of the interaction with the other particles. As a first approximation this condition is simulated constraining the points on the sphere surface ($u(R) = 0$), aware that this assumption is much more strict than the reality.
So C_1 is derived making the displacement equation vanishes on the surface, this leads to:

$$u(R) = \frac{1+\nu}{1-\nu}\frac{\Omega}{3}\frac{1}{R^2}\int_0^R C(r)r^2\,dr + C_1 R = 0 \tag{3.70}$$

and so:

$$C_1 = -\frac{1+\nu}{1-\nu}\frac{\Omega}{3}\frac{1}{R^3}\int_0^R C(r)r^2\,dr \tag{3.71}$$

Finally the displacement field is reported in equation 3.72.

$$u(r) = \frac{1+\nu}{1-\nu}\frac{\Omega}{3}\left[\frac{1}{r^2}\int_0^r C(r)r^2\,dr - \frac{r}{R^3}\int_0^R C(r)r^2\,dr\right] \tag{3.72}$$

The shape of the displacement is reported in figure 3.12. The concentration profile considered is the same used to derive the displacement with free surface condition.

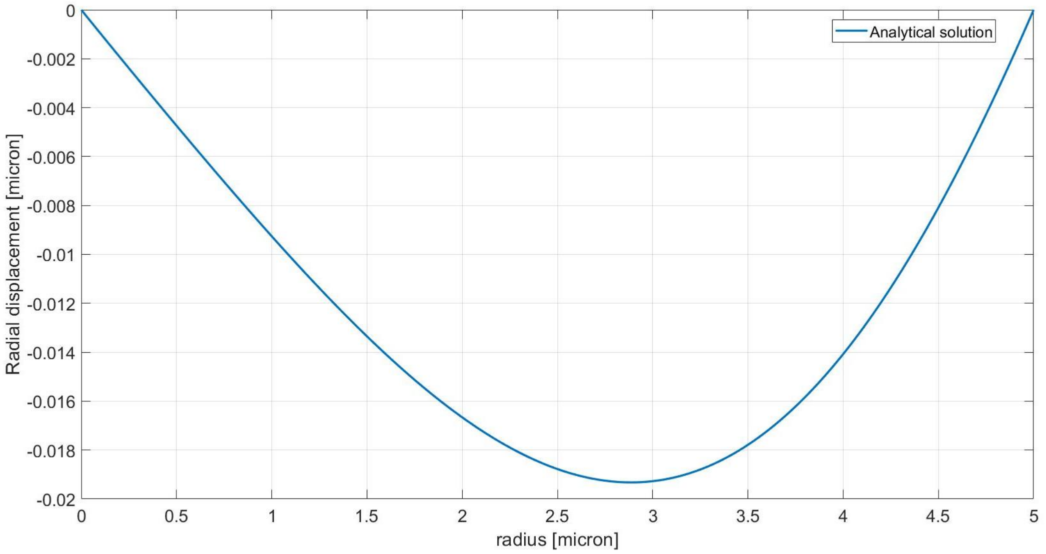

Figure 3.12: Radial displacement due to potentiostatic insertion at $\tau = 0.0574$ with constrained surface boundary condition

Then the strain and stress relationship are derived in analogy to the case "free surface", and are reported in equations 3.73 and 3.74.

$$\begin{cases} \varepsilon_r = \frac{1+\nu}{1-\nu}\frac{\Omega}{3}[-\frac{2}{r^3}\int_0^r C(r)r^2\,dr + C(r) - \frac{1}{R^3}\int_0^R C(r)r^2\,dr] \\ \\ \varepsilon_c = \frac{1+\nu}{1-\nu}\frac{\Omega}{3}\left[\frac{1}{r^3}\int_0^r C(r)r^2\,dr - \frac{1}{R^3}\int_0^R C(r)r^2\,dr\right] \end{cases} \tag{3.73}$$

$$\begin{cases} \sigma_r = -\frac{\Omega}{3}\frac{E}{1-\nu}\left[\frac{1+\nu}{1-2\nu}\frac{1}{R^3}\int_0^R C(r)r^2\,dr + \frac{2}{r^3}\int_0^r C(r)r^2\,dr\right] \\ \\ \sigma_c = \frac{\Omega}{3}\frac{E}{(1-\nu)(1-2\nu)}\left[-(1+\nu)\frac{1}{R^3}\int_0^R C(r)r^2\,dr + (1-2\nu)\frac{1}{r^3}\int_0^r C(r)r^2\,dr + C(r)\right] \end{cases} \tag{3.74}$$

The stress values for $r = 0$ have to be computed separately as done before, solving the limit of the stress for r tending to zero. The shape of radial and circumferential stress, always with the same concentration profile, are reported in figure 3.13 and 3.14.

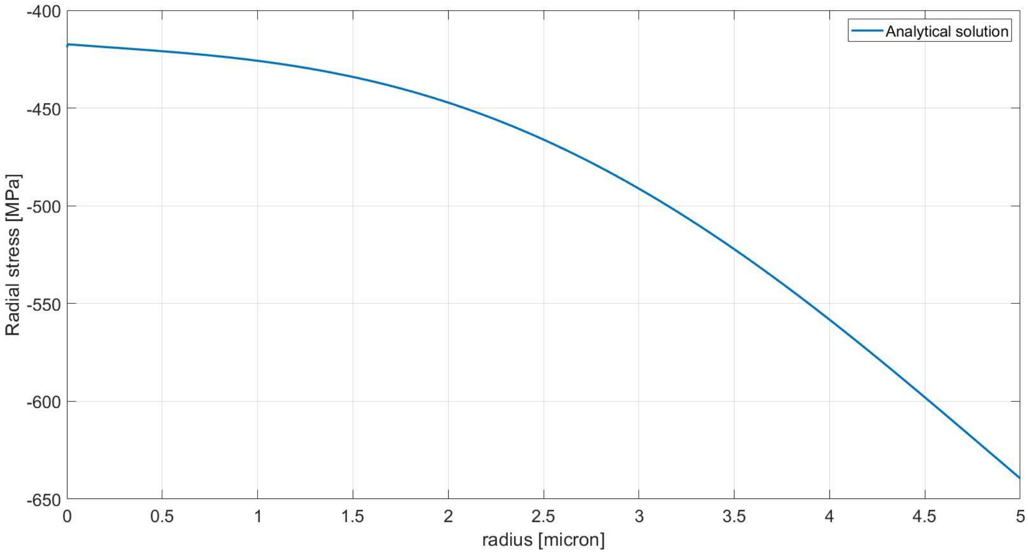

Figure 3.13: Radial stress due to potentiostatic insertion at $\tau = 0.0574$ with constrained surface boundary condition

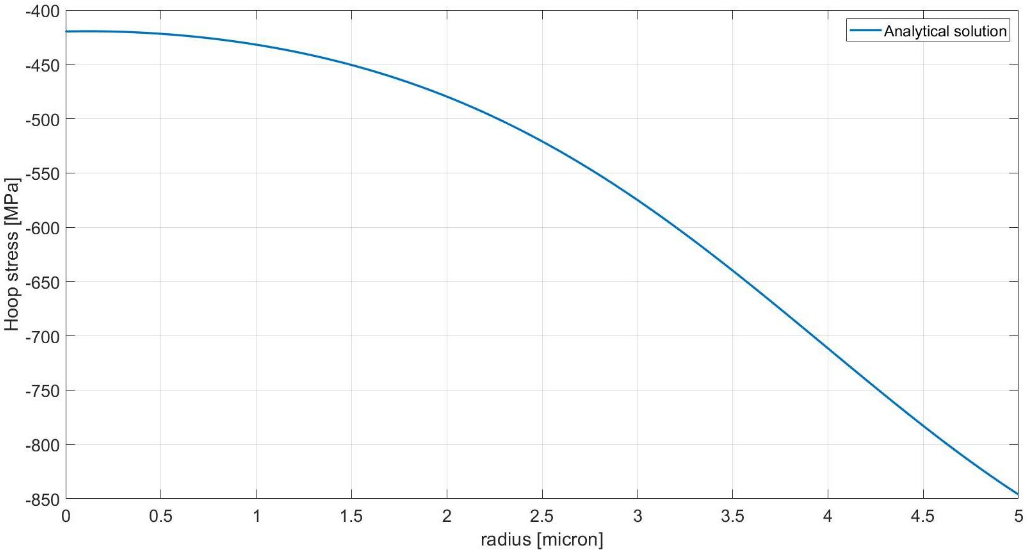

Figure 3.14: Circumferential stress due to potentiostatic insertion at $\tau = 0.0574$ with constrained surface boundary condition

The stress state with this boundary condition is definitely translated towards the compression one, erasing the tensile stress and increasing the values of compression stress. This suggests that the interaction with the other particle could lead to potential fracture in the contact zones due to stress concentration. However it is necessary to emphasize that the stress are just compressive.

3.1.3 Coupled problem

The following step involves in considering the whole expression of chemical potential reported in equation 3.2, namely the concentration dependence on the hydrostatic stress.
First of all the expression of hydrostatic stress is computed from the radial and hoop stress reported in 3.64 as follow:

$$\sigma_h = \frac{\sigma_1 + \sigma_2 + \sigma_3}{3} = \frac{\sigma_r + 2\sigma_c}{3} = \frac{2\Omega E}{9(1-\nu)}\left[\frac{3}{R^3}\int_0^R C(r)r^2\,dr - C(r)\right] \tag{3.75}$$

The expression of the hydrostastic stress in 3.75 depends on the radial coordinate only through the concentration, in fact the integral valued from zero to T is constant in the whole particle, this will lead to a particular result later.
Then the derivation of the hydrostatic stress respect to the radial coordinate is expressed according the chain rule in equation 3.76.

$$\begin{aligned}\frac{\partial\sigma_h}{\partial r} &= \frac{\partial\sigma_h}{\partial C}\frac{\partial C}{\partial r}\\ \frac{\partial\sigma_h}{\partial C} &= -\frac{2\Omega E}{9(1-\nu)}\\ \frac{\partial\sigma_h}{\partial r} &= -\frac{2\Omega E}{9(1-\nu)}\frac{\partial C}{\partial r}\end{aligned} \tag{3.76}$$

The result in the last row of equation 3.76 is replaced in equation 3.4:

$$\begin{aligned}J &= -D\left(\frac{\partial C}{\partial r} + \frac{\Omega C}{RT}\frac{2\Omega E}{9(1-\nu)}\frac{\partial C}{\partial r}\right)\\ J &= -D\left(1 + \frac{2\Omega^2 EC}{9RT(1-\nu)}\right)\frac{\partial C}{\partial r}\end{aligned} \tag{3.77}$$

The second row of equation 3.77 allows to describe the influence of the stress rate on the concentration distribution keeping the same expression of the ionic flux, meant as a diffusion coefficient multiplied for the concentration gradient. Therefore the stress rate influence results in a corrective factor which multiply the diffusion coefficient. This allows to define a equivalent diffusivity value reported in equation 3.78.

$$D_{eqvn} = D\left(1 + \frac{2\Omega^2 EC}{9RT(1-\nu)}\right) \tag{3.78}$$

The term in the parenthesis of equation 3.78 is always greater than one, even for materials with negative partial molar volume, since its value is squared. For this reason, the coupling between the stress and the diffusion results always in a greater equivalent diffusivity coefficient, so the diffusion is always enhanced respect to the pure diffusive model. This leads to smoother concentration gradient within the cell and a modification of the stress rate.

Equation 3.77 allows to compute the concentration gradient using the analytical solutions 3.26 and 3.46 derived in the previous section, replacing the equivalent

diffusivity defined in 3.78 instead of the diffusion coefficient. However now the solutions 3.26 and 3.46 do not give immediately the final result because also the right hand side depends on the concentration through the equivalent diffusivity.
An iterative calculation, shown in figure 3.15 is carried out in order to solve the non linear solutions 3.26 and 3.46.

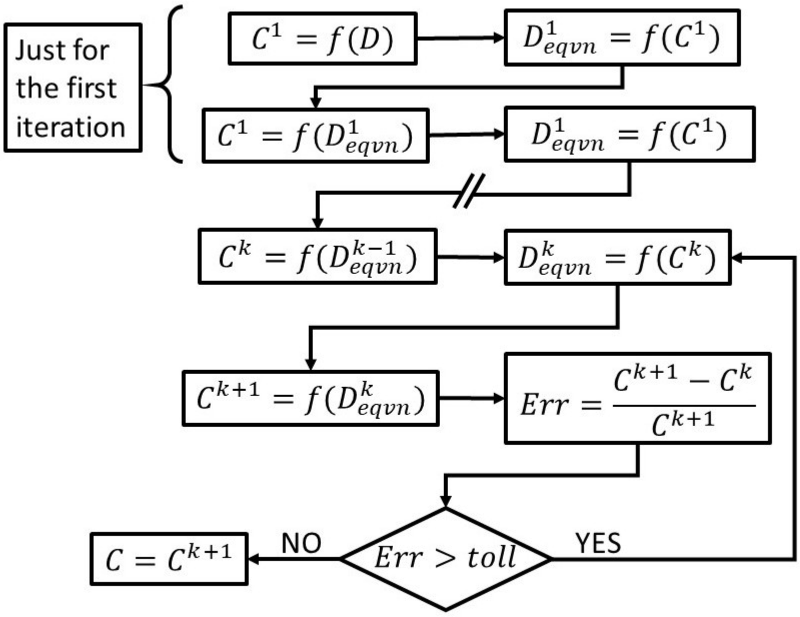

Figure 3.15: Iterative calculation for the stress-concentration coupled solution

The tolerance value mentioned in figure 3.15 is set to 0.001. The solution converges in about 20 iterations with this tolerance.
The results in case of galvanostatic insertion are reported in figure 3.16 and 3.17.

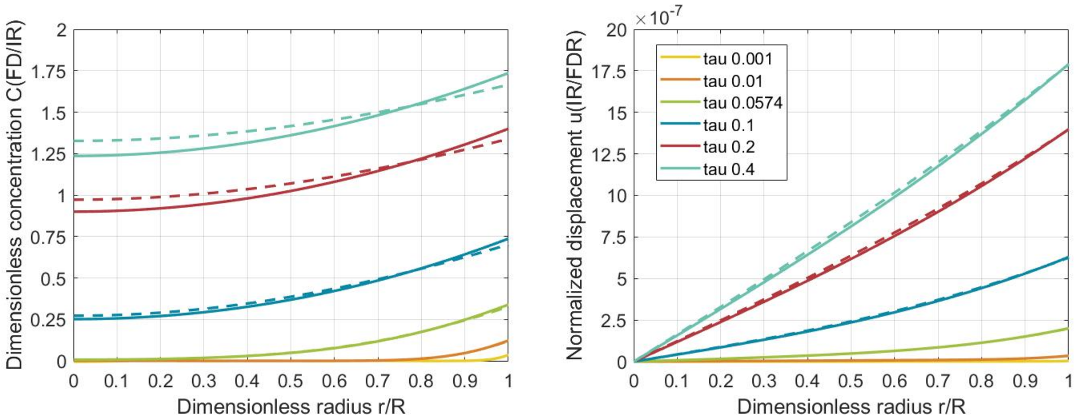

Figure 3.16: Left: normalized concentration in galvanostatic insertion. Right: normalized displacement in galvanostatic insertion. Solid and dashed lines refer to uncoupled and coupled model respectively. The colors refers to the same normalized times reported in legend.

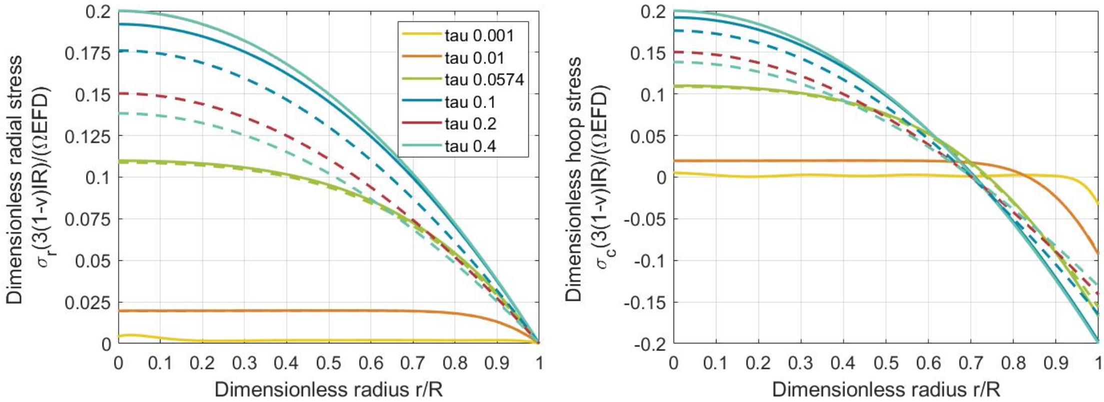

Figure 3.17: Left: normalized radial stress in galvanostatic insertion. Right: normalized hoop stress in galvanostatic insertion. Solid and dashed lines refer to uncoupled and coupled model respectively. The colors refers to the same normalized times reported in legend.

The equivalent diffusivity, greater than the diffusion coefficient D, makes the concentration gradient smoother and allows to achieve a greater concentration level within the particle. The displacements are slightly increased according to figure 3.16.
The stress, reported in figure 3.17, in the coupled model are reduced respect to the uncoupled model, both in tension and compression, thanks to the smoother gradient which reduce the chemical strain, according to equation 3.1.
The result in galvanostatic extraction are reported in figure 3.18 and 3.19.

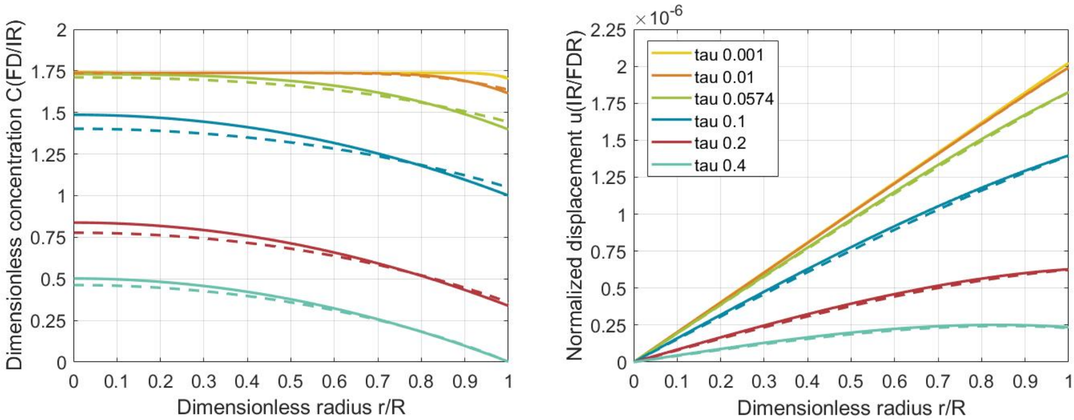

Figure 3.18: Left: normalized concentration in galvanostatic extraction. Right: normalized displacement in galvanostatic extraction. Solid and dashed lines refer to uncoupled and coupled model respectively. The colors refers to the same normalized times reported in legend.

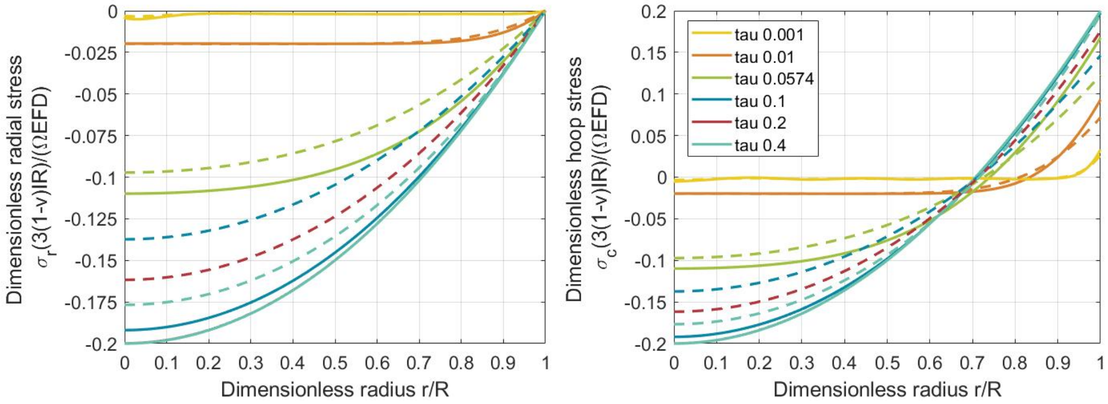

Figure 3.19: Left: normalized radial stress in galvanostatic extraction. Right: normalized hoop stress in galvanostatic extraction. Solid and dashed lines refer to uncoupled and coupled model respectively. The colors refers to the same normalized times reported in legend.

Even in extraction the values of the stress are reduced considering the dependence of the chemical potential with the stress.
Finally the same results are derived with potentiostatic operation. The results for lithium insertion are reported in figures 3.22 and 3.23. The coupled model is still characterized by a smoother concentration gradient, with higher concentration levels and slightly greater displacements.
Otherwise the stress trend for the coupled model is different respect to galvanostatic operation. The coupled model presents greater stress for the lower time constants τ respect to the uncoupled model, and viceversa for the greater time constants τ, as in galvanostatic operation. This suggests that the beginning of insertion could be a critical condition.

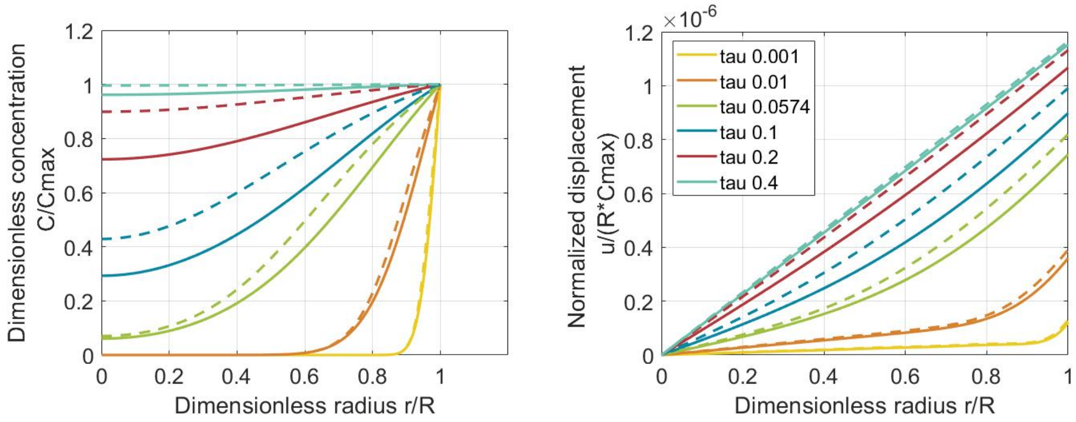

Figure 3.20: Left: normalized concentration in potentiostatic insertion. Right: normalized displacement in potentiostatic insertion. Solid and dashed lines refer to uncoupled and coupled model respectively. The colors refers to the same normalized times reported in legend.

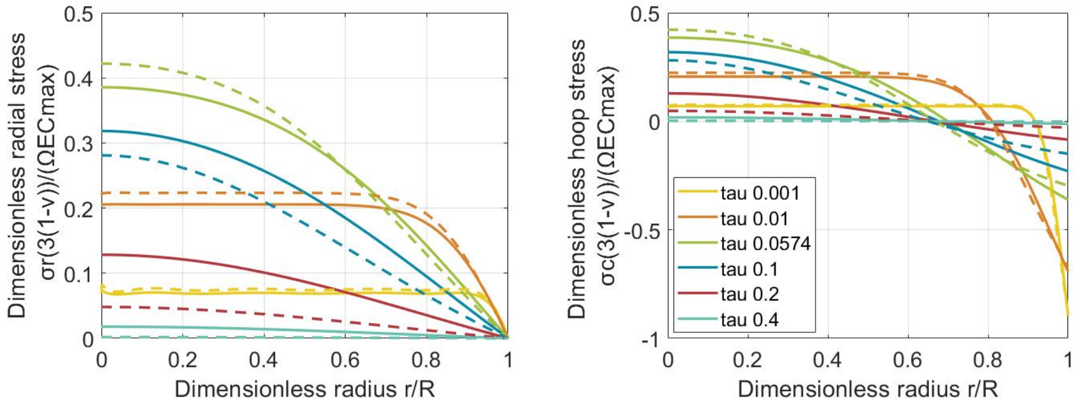

Figure 3.21: Left: normalized radial stress in potentiostatic insertion. Right: normalized hoop stress in potentiostatic insertion. Solid and dashed lines refer to uncoupled and coupled model respectively. The colors refers to the same normalized times reported in legend.

The results for potentiostatic extraction are reported in figures 3.22 and 3.23. The greater equivalent diffusivity of the coupled model results in lower concentration levels, since the lithium ions diffuse faster in the particle, this results also in lower displacement. Even in extraction the coupled model presents greater stress for the lower time constants τ. However this fact does not involve a critical condition because the hoop stress is really similar both for the coupled and uncoupled model. Indeed the hoop stress is the most dangerous stress in extraction because it presents tensile stress on the surface.

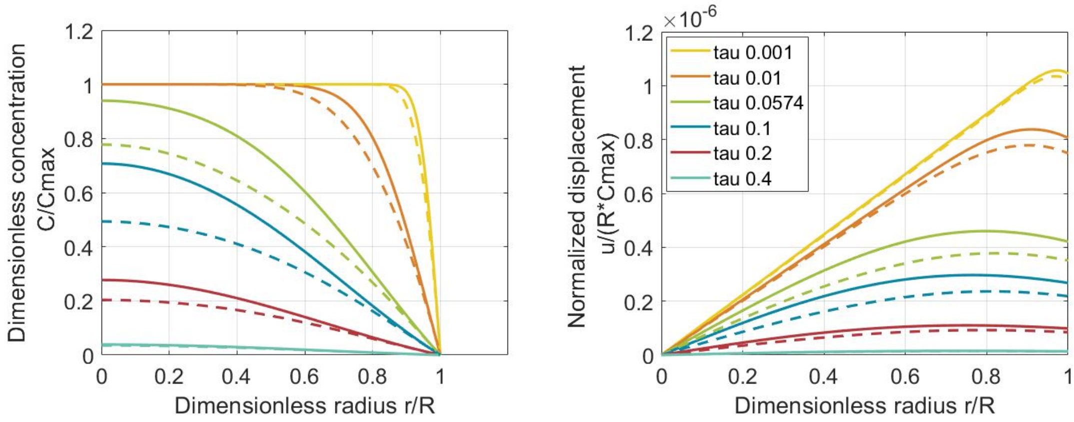

Figure 3.22: Left: normalized concentration in potentiostatic extraction. Right: normalized displacement in potentiostatic extraction. Solid and dashed lines refer to uncoupled and coupled model respectively. The colors refers to the same normalized times reported in legend.

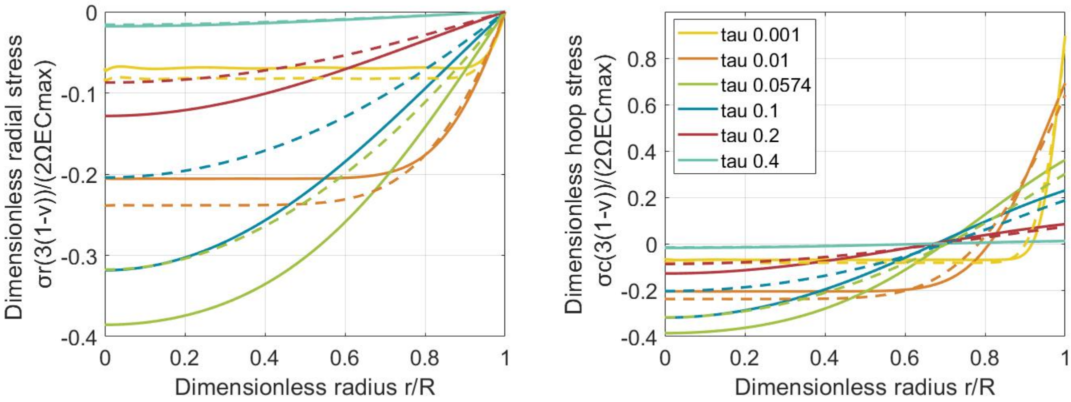

Figure 3.23: Left: normalized radial stress in potentiostatic extraction. Right: normalized hoop stress in potentiostatic extraction. Solid and dashed lines refer to uncoupled and coupled model respectively. The colors refers to the same normalized times reported in legend.

3.2 Numeric analysis

Numeric analysis were performed in order to validate the analytical model and to deduce a more realistic behavior of the interaction with other particles.
The problem is modeled in Ansys APDL as an hemisphere with plane 82 elements in axisymmetric mode. The geometry and the mesh of the particle is reported in figure 3.24.

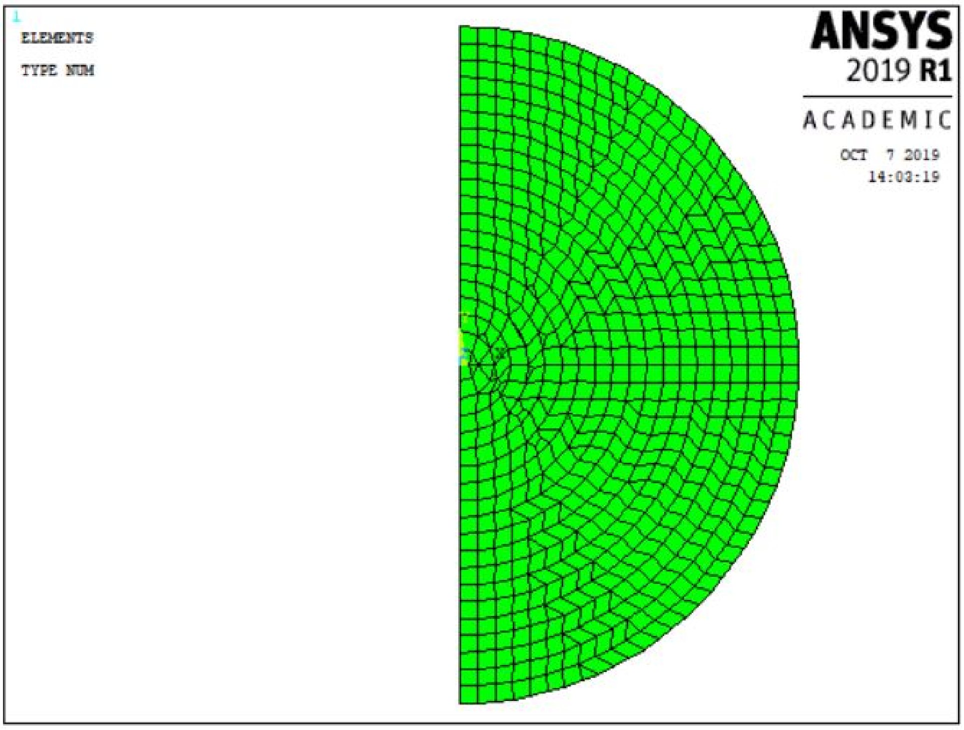

Figure 3.24: Hemisphere simulated in Ansys in axisymmetric mode

3.2.1 Analogy between thermal and chemical strain

The shape of the equation 3.1 which describes the chemical strain is the same of the equation which describes the thermal strain of a body characterized by a temperature field. The only difference between these two lies in the different proportionality coefficient, i.e. partial molar volume for the first and thermal expansion coefficient for the latter. The similitude between this phenomena allows to describe the strain induced by the chemical gradient as the one induced by an equivalent temperature gradient, facilitating the implementation of such a model in a finite element commercial program.
Now the problem lies in finding a proper temperature gradient which produces a strain field as the one induced by the considered concentration gradient. This is made equating the thermal strain and chemical strain equation (equation 3.79).

$$\alpha \Delta T = \frac{\Omega}{3} \Delta C \tag{3.79}$$

Equation 3.79 is solved for $T(r)$, omitting the difference.

$$T(r) = \frac{\Omega}{3\alpha} C(r) \tag{3.80}$$

Equation 3.80 gives the temperature profiles as a function of the particle radius to assign to the body in order to replicate the strain field caused by the concentration distribution $C(r)$. The coefficient α is just a set parameter and can be chosen arbitrarily, since it just modify the absolute temperature value but not the difference, which is the real cause of the strain.

The temperature field is not applied as a continuous function over the particle but it has been done in this way: the hemisphere is divided in k concentric areas, as shown in figure 3.25, and an equivalent temperature value is assigned to each area.

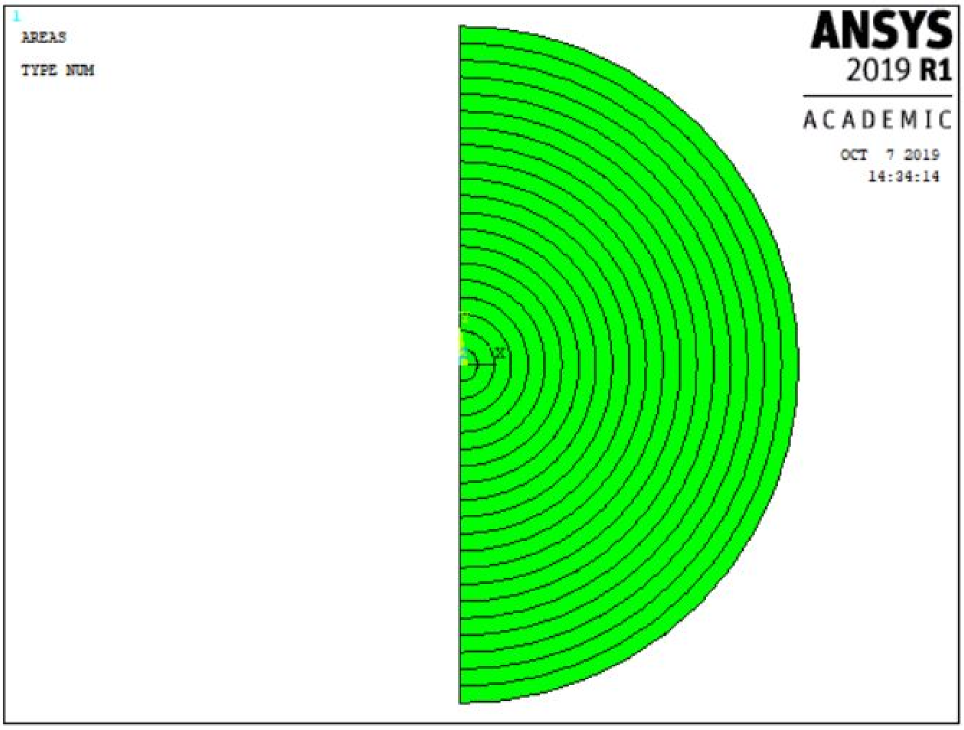

Figure 3.25: Areas with $k = 20$

Referring to figure 3.26, the concentration function is valued at the coordinate R_k in the middle between the coordinates which define the arcs of the k-th area. Then, knowing the value $C(r_k)$, the equivalent temperature value to be assigned to the k-th area is derived from equation 3.80.
In this way an equivalent temperature field, which generates a body force field as the one generated by the concentration gradient, is assigned to the sphere.

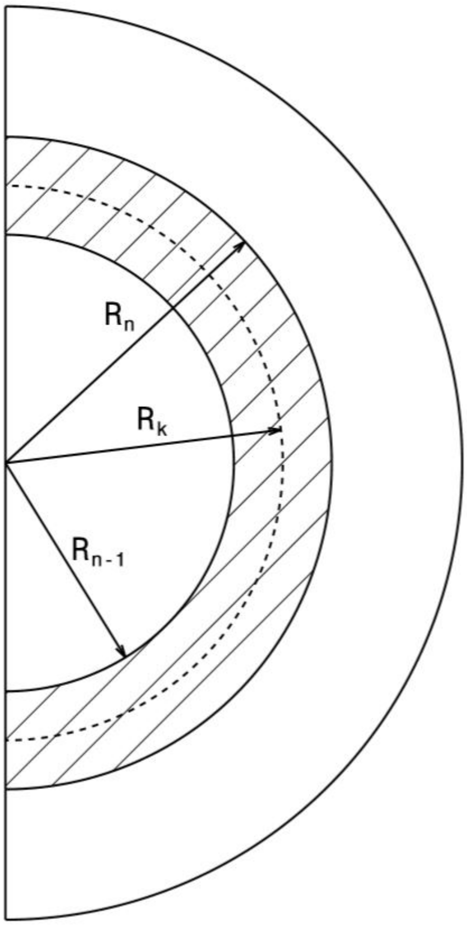

Figure 3.26: K-th area

3.2.2 analytical model validation

The first step involves in validating the results of the analytical model.
The load acting on the particle is the concentration gradient due to lithium diffusion, which is simulated as a temperature gradient as explained in the previous section. Four different operation conditions are taken into consideration, which result in different concentration profiles: insertion and extraction both in potentiostatic and galvanostatic mode. Each operation condition can still be valuated at different normalized time τ, resulting in different concentration profiles for each configuration
The node at the center of the sphere is constrained, in order to prevent rigid body motion.
The displacement field calculated by Ansys is shown in figure 3.27. The displacement and stress fields are symmetric respect to the center of the sphere, as expected from the axisymmetric nature of the problem.
The following results are obtained in case of lithiation and with a time constant $\tau = 0.0574$. This value is the one which guarantees the higher radial stress values.

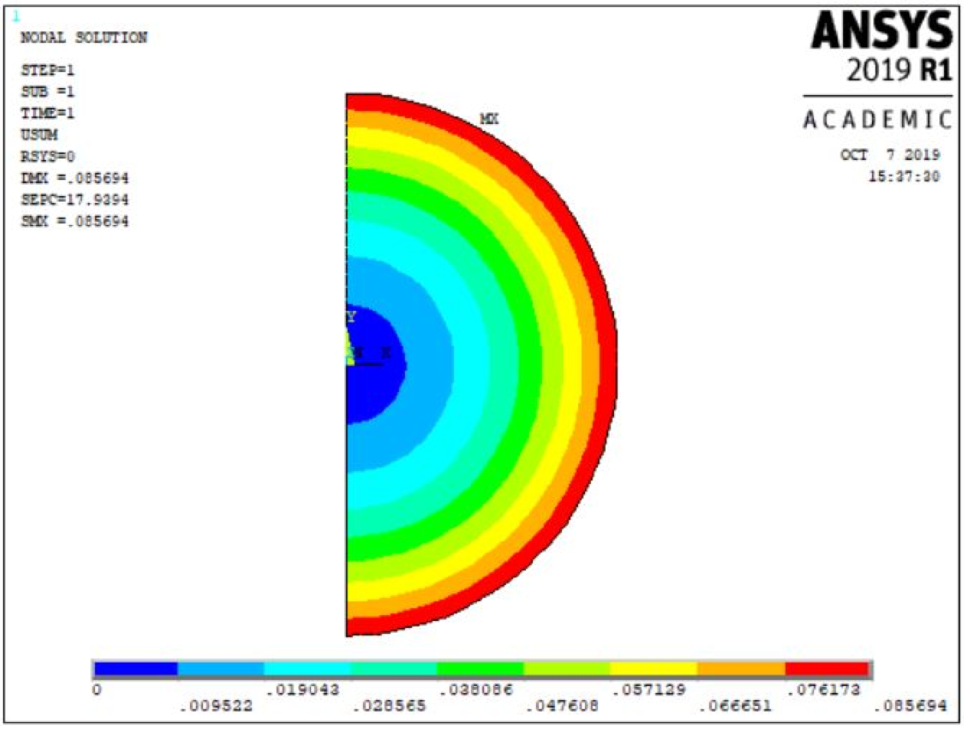

Figure 3.27: Numeric displacement field during lithiation in potentiostatic operation with "free surface condition"

Then the numeric solution is plotted versus the radial coordinate and compared to the analytical one. The results of the displacement and the stress are showed in figure 3.28.

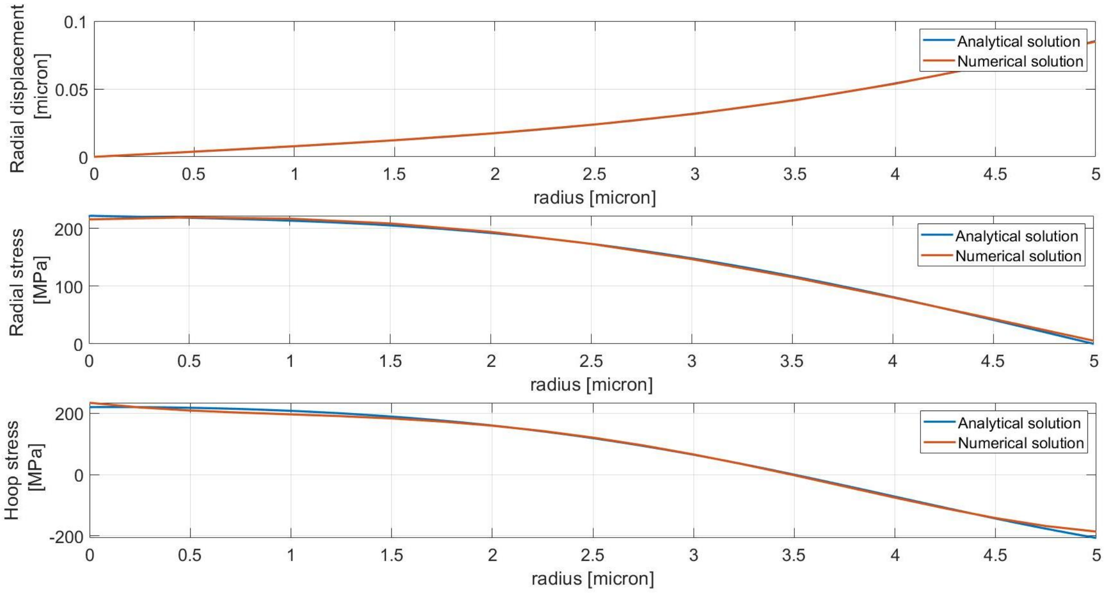

Figure 3.28: Comparison between numerical and analytical results in potentiostatic insertion at $\tau = 0.0574$ with free surface boundary condition

The same comparison is made for the "constrained surface condition", and the results are showed in figure 3.29.

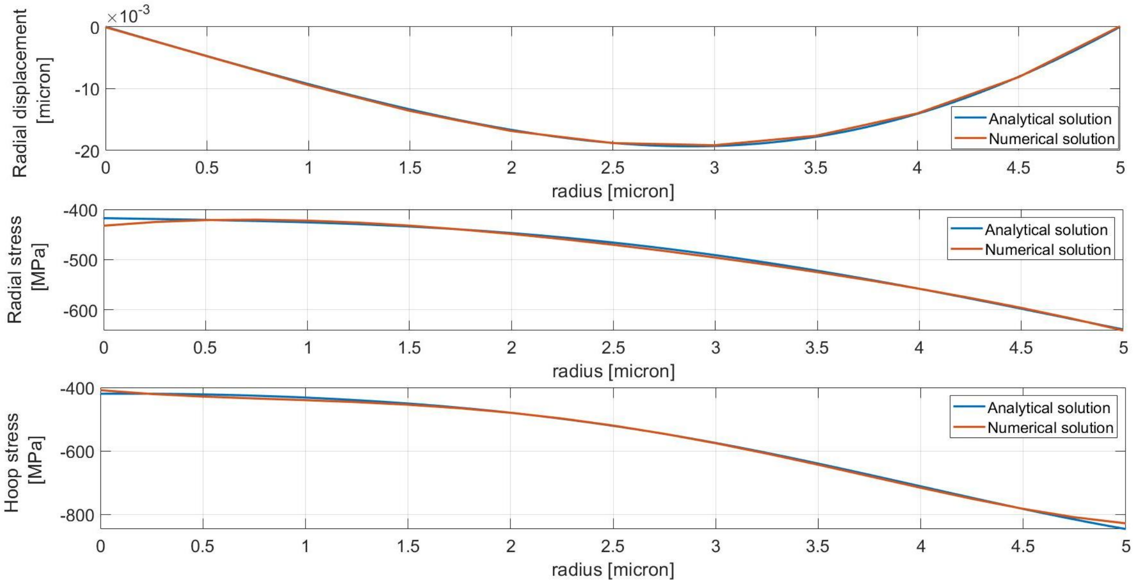

Figure 3.29: Comparison between numerical and analytical results in potentiostatic insertion at $\tau = 0.0574$ with constrained surface boundary condition

The results shown in figures 3.28 and 3.29 show a good agreement between the analytical and numerical models, and confirm the equivalence between thermal and chemical strain.

Therefore displacement and stresses fields are derived with delithiation operation (extraction). This case is simulated assuming an initial constant concentration level within the particle, setting the value $C_0 = C_{max}$. C_{max} is the concentration level reached at the end of lithiation.
The displacement and stress fields are reported in figure 3.30.

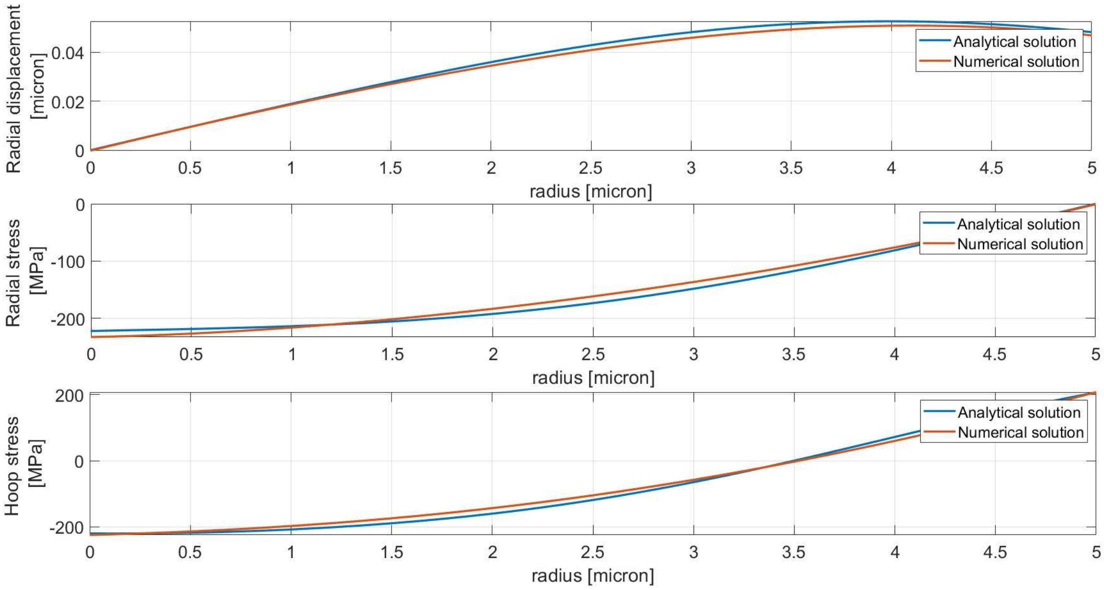

Figure 3.30: Comparison between numerical and analytical result in potentiostatic extraction at $\tau = 0.0574$ with free surface boundary condition

A good agreement between analytical and numerical results is achieved in case of extraction. It is worth to underline that the hoop stress on the surface is tensile with this type of operation. This could be the driving force of crack propagation.

All the presented results are derived with potentiostatic control, the same could be derived with the galvanostatic one, it just changes the shape of the concentration profile.

At this stage the meaning of the sign of stress is explained.
During lithiation the outer part of the sphere is expanding at a greater rate than the core, so the radial stress is tensile. For the same reason the hoop stress is tensile in the core and compressive in the surface, because the expansion of the surface is prevented by the lower expansion rate of the core.
Instead, during delithiation, the outer part of the sphere is expanding at a lower rate of the core, since the concentration is lower in the surface and greater in the core. This causes a compressive radial stress in the sphere. Therefore the hoop stress is tensile on the surface and compressive in the core because the expansion of the core is prevented by the lower one of the surface.
It is useful to replace the concentration strain with the temperature strain, in order to better understand this concept. Indeed the hoop stress in delithiation is equivalent to the tensile stress in shaft hardening.

3.2.3 Contact model

The interaction of the particle with its boundary is studied in order to identify how this effect affects the stress rate within the particle. A contact analysis is heavily non linear, and is carried out with a FEM software (Ansys APDL).

This analysis is carried out using dedicated elements for contact analysis, *conta172* and *targe169*. These are line-type elements applied to the nodes on the surfaces which are supposed to come in contact. *conta172* lies on the surface of the deformed body, and *targe169* lies on the body which defines the constraints of the deformed body. These elements have three nodes, so they fit well on the sides of a plane82 square element, used for the discretization of the bodies. A sketch of the contact element is reported in figure 3.31.

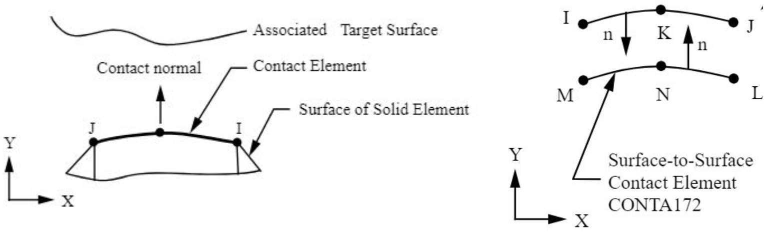

Figure 3.31: Conta172 and targe169 elements

Each contact pair has to be defined by the same real constant, which defines also the stiffness contact. ANSYS numerically puts a spring of defined stiffness between the two surface which comes in contact. If the the spring is stiff enough, the behaviour of the model is like the two surfaces have made contact. The stiffness value can greatly affect the solution, so an iteration on its value is necessary in order to get a proper convergence solution. A low stiffness value is chosen at the beginning, in order to verify if the model converges properly. Then if the model does not converge a lower value has to be chosen. Then, after that a stiffness value which guarantee a convergent solution is found, it is gradually increased in order to simulate a more realistic contact. In fact if the stiffness value is too low the penetration of the contact surfaces could occur.
Then a proper tuning of the solution control parameters is performed in order to get a convergent solution. Initially it has been set a large number of minimum substep, in order to prevent the situation in which the contact nodes are driven through the target one too fast, which leads to a not convergent solution. Finally this parameter is set to 20.
Therefore 100 substeps as a first attempt are set, so one hundredth of the total load is applied at the first step. A too large load in just one step could cause a huge element distortion which leads to a solution failure.
Then 1000 is set as maximum number of substeps, in order to stop the calculations if a convergent solution is not got within this steps. Finally auto time stepping is set, so the software determine the appropriate size of each substeps, respecting the limits on maximum and minimum number set before.
Finally nonlinear solution is enabled.

The first model aims to simulate the interaction of the particle with the current collector, assumed as a thin plate.
The constraints of the model are defined as follows: the displacements along x and y axis of the nodes of the current collector are set to zero, as well as the central node of the sphere. This type of constraints are chosen in order to describe the stress rate and the displacement field which result from the interaction between

the current collector and the particle, and does not pretend to simulate a real configuration. Indeed the current collector would be deformable and the particle should be constrained from the interaction with the other particles.
conta172 elements lies on a fraction of the particle surface and *targe169* on the current collector.
The results show that the interaction with the current collector causes a different response for the displacement and the stresses.
The radial displacement, shown in figure 3.32, is close to zero near the contact area and gradually increase to the value which results from "free surface" condition, however the constraint influences the displacement field all over the particle.

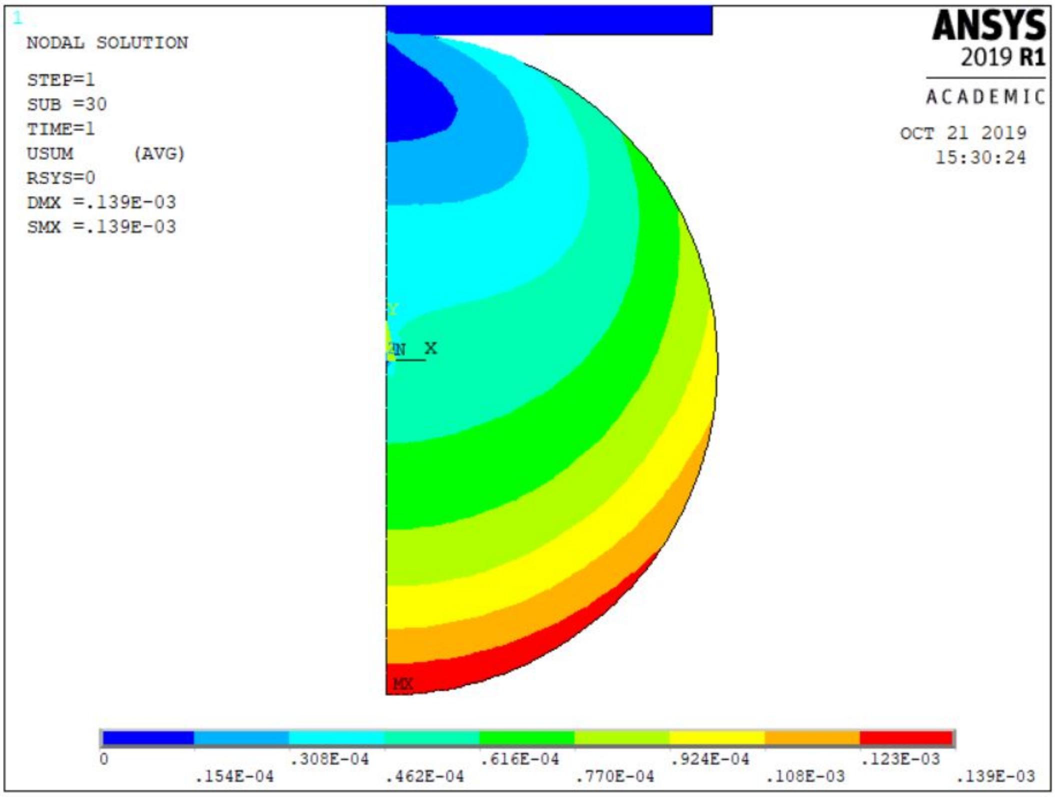

Figure 3.32: Displacement field in lithaition due to the interaction with the current collector

The stresses, reported in figure 3.33-3.34, are subjected to a sharp increment in compression stress in the area really close to the contact, but all over the particle the stress are similar to the unconstrained condition.

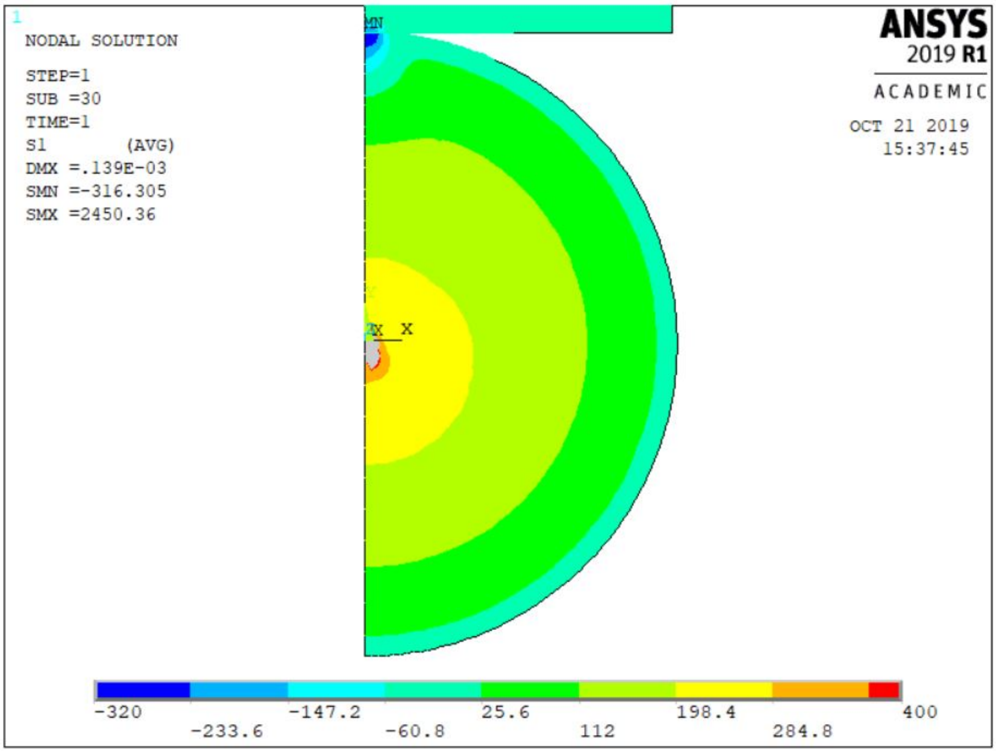

Figure 3.33: Radial stress field in lithaition due to the interaction with the current collector

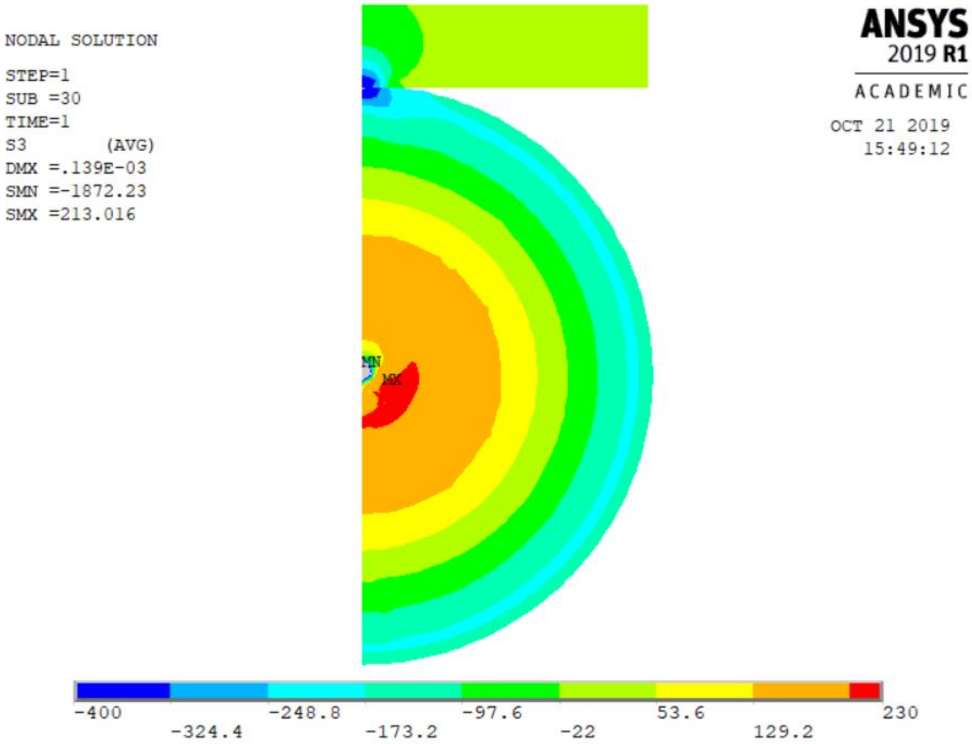

Figure 3.34: Hoop stress field in lithaition due to the interaction with the current collector

A second contact model takes into account the interaction of the particle with its surroundings. The surrounding is simulated with the assumption that the whole negative electrode acts as a bulk material with the same mechanical properties (Young modulus and Poisson ratio) of the graphite, as shown in figure 3.35. Since the anode is composed at 90% by graphite and 5% by black carbon and %5 by binder the mechanical properties of the anode are really close to the one of the graphite. The assumption of bulk material neglects the porous nature of the anode, neglecting the concentrated effects of the interaction between two particles and replacing it with a continuous contact on all over the surface particle. Therefore the problem is discretized so that the particle and the contact zones are characterized by a finer mesh, and the areas far from the contact with a more coarse one. An initial gap of $10^{-5} mm$ is left between the particle and the target surface, and the contact stiffness is set to 2000kN.

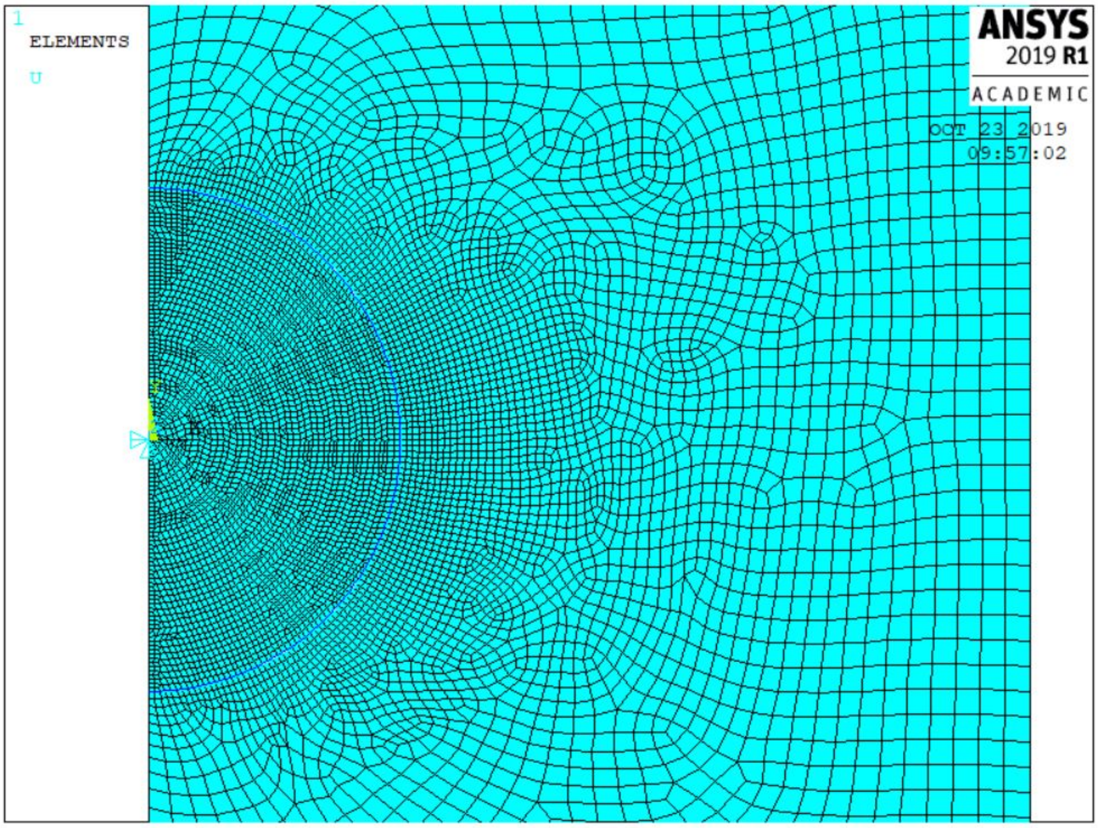

Figure 3.35: Discretization of the geometry

At first insertion condition is simulated. The sphere is divided in 20 concentric areas, and a set of temperature values are assigned to each of the areas in order to replicate the required concentration gradient. As expected, the solution remains axysymmetric. The displacement field is reported in figure 3.36.

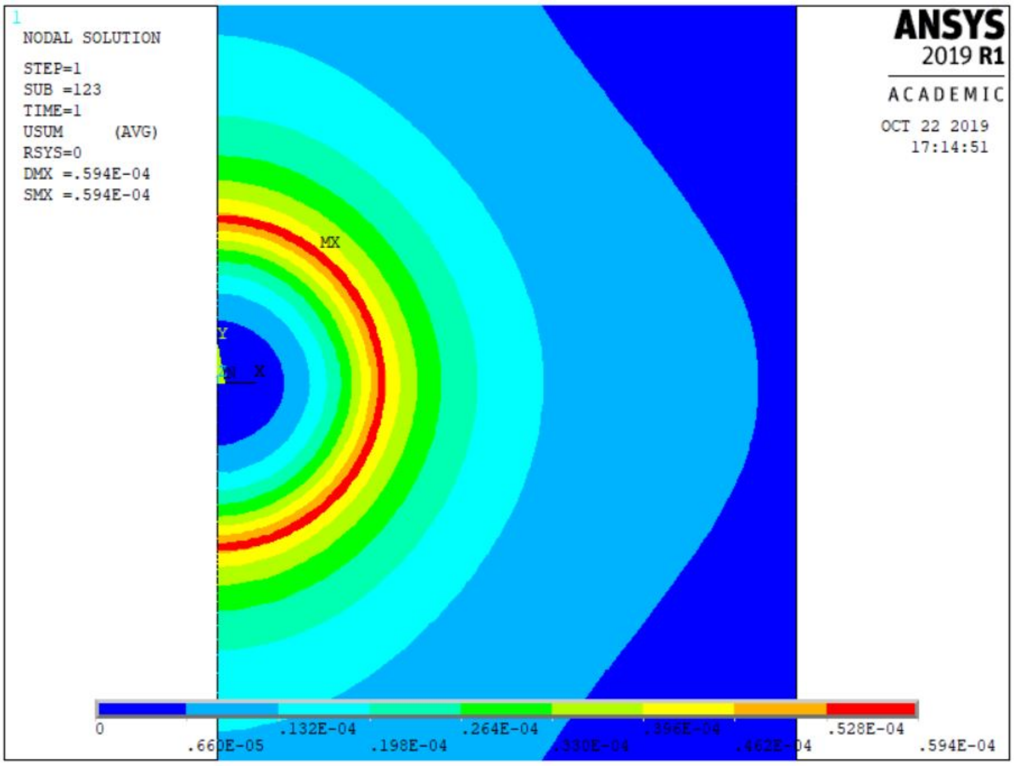

Figure 3.36: Displacement field within the sphere and the deformable constraint in insertion condition

The three different boundary condition, namely "free surface", "constrained surface" and "deformable constraint" defined by this contact model, are compared in figure 3.37. The displacement function derived with this model underlines how it simulates a condition between two extreme cases: totally free and totally constrained.

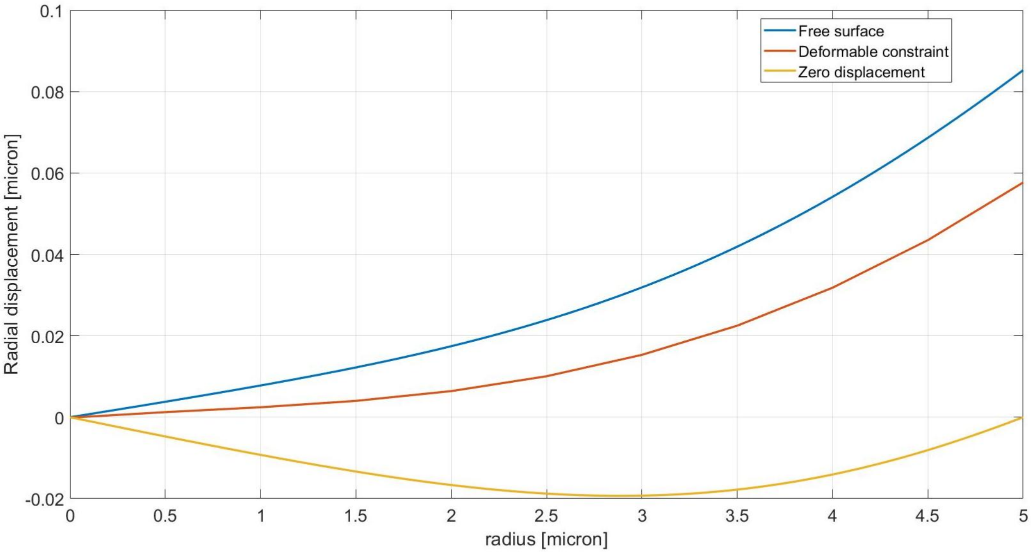

Figure 3.37: Displacement field for "free", "deformable constraint" and "totally constrained" models in insertion condition

The radial and hoop stress fields which result from the "deformable constraint" condition are reported in figure 3.38-3.39.

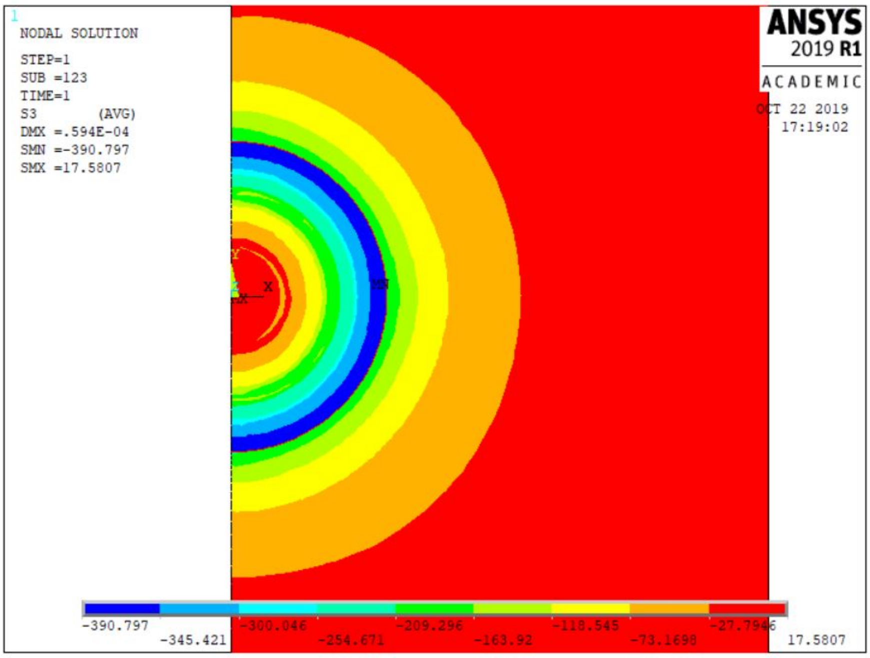

Figure 3.38: Radial stress field within the sphere and the deformable constraint in insertion condition

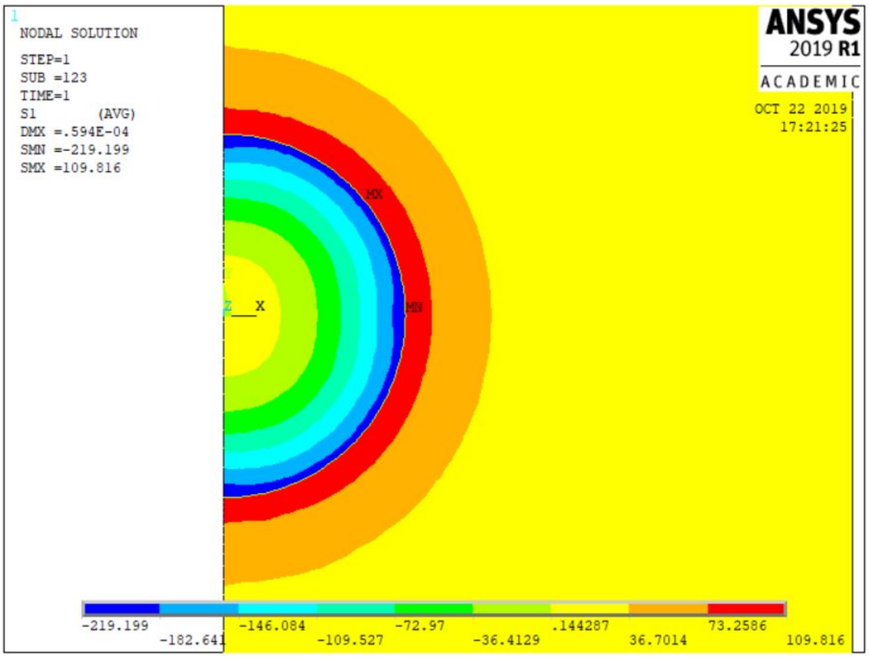

Figure 3.39: Hoop stress field within the sphere and the deformable constraint in insertion condition

It is observed from figure 3.39 that the "bulk" material near the contact zone experiences an high tensile hoop stress, which could potentially lead to mechanical failure.

The comparison between the stresses in the three mentioned conditions is reported in figure 3.40.

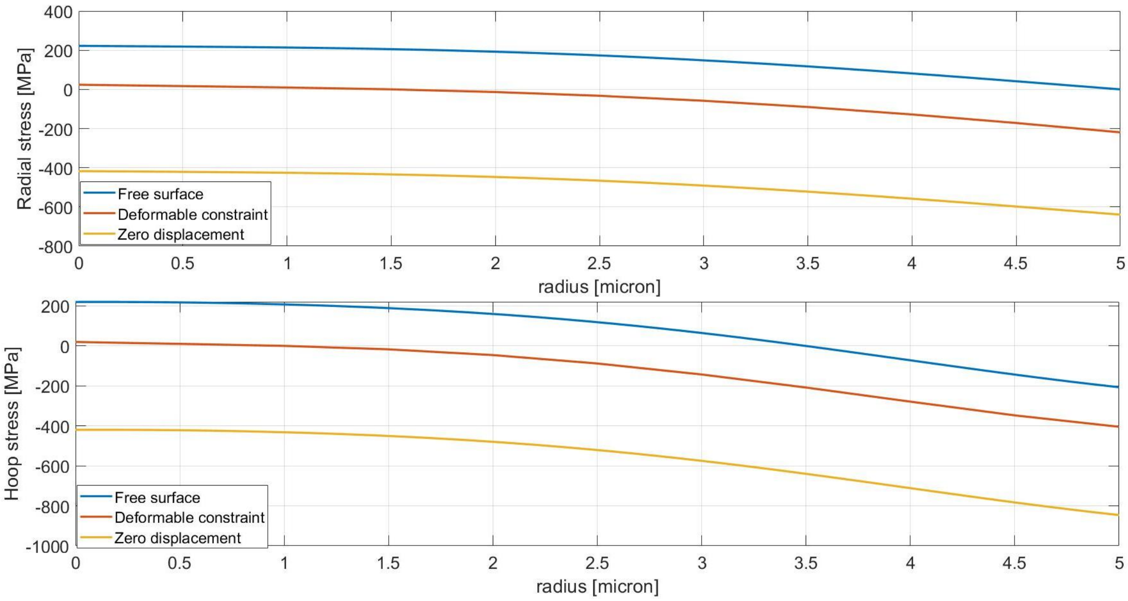

Figure 3.40: Stresses fields for "free", "deformable constraint" and "totally constrained" models in insertion condition

Referring to figure 3.40, it can be concluded that this model results in a stress rate comprised between the "free" and "totally constrained" conditions. So a slight drift towards the compression stress occurs respect to the free condition. This suggests that in real operation the tensile stresses are really prevented by the contact phenomena.
This fact leads, for example, to a reduction of the driving force of crack propagation. Even if the drift towards the compressive stress depends strongly on the young modulus of the constraint. For this reason the stiffness of the constraints has to be studied more extensively.

The same problem is studied in extraction condition, assigning the proper temperature values to each of the areas. The resulting displacement field is reported in figure 3.41.

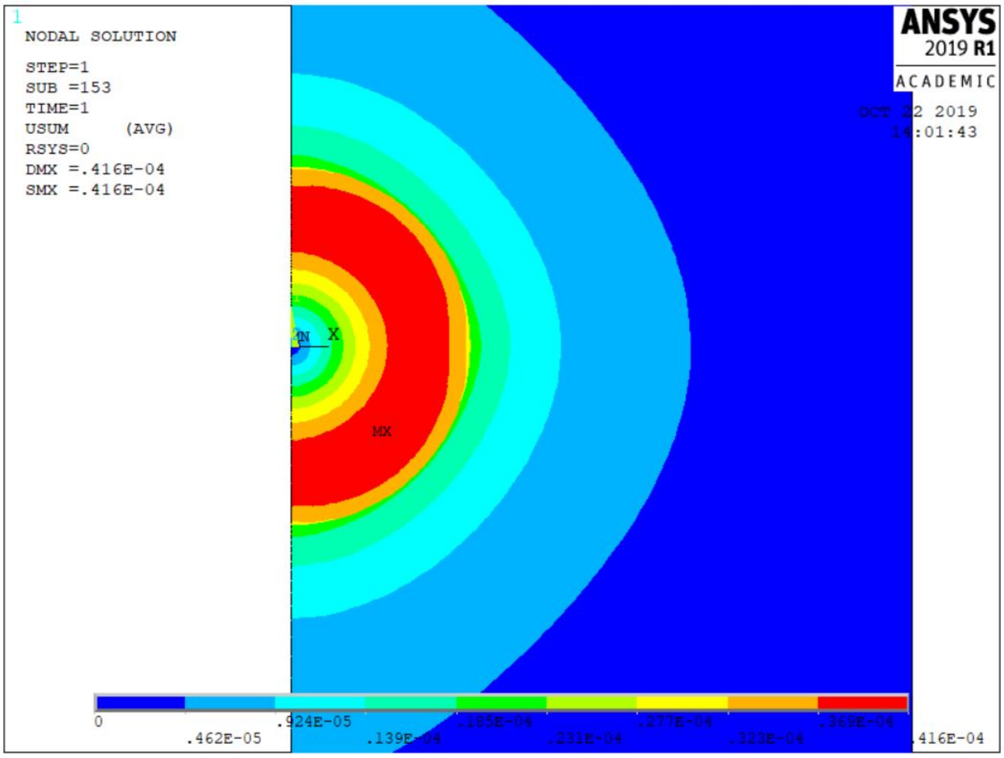

Figure 3.41: Displacement field within the sphere and the deformable constraint in extraction condition

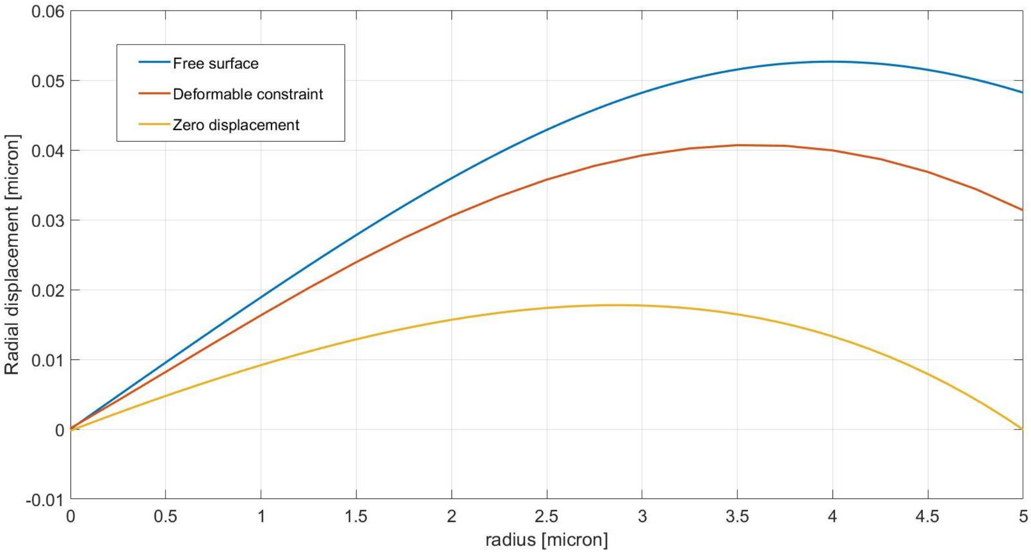

Figure 3.42: Displacement field for "free", "deformable constraint" and "totally constrained" models in extraction condition

The displacement field of this model in figure 3.41 has the same shape of the ones studied with the analytical model in "free" or "totally constrained" surface condition, and is characterized by non null value on the surface, allowed by the deformation of the constrains. The displacement value in the surface of the "deformable constraint" model, as expected, is between the one of the "free" and the "totally constrained" condition.

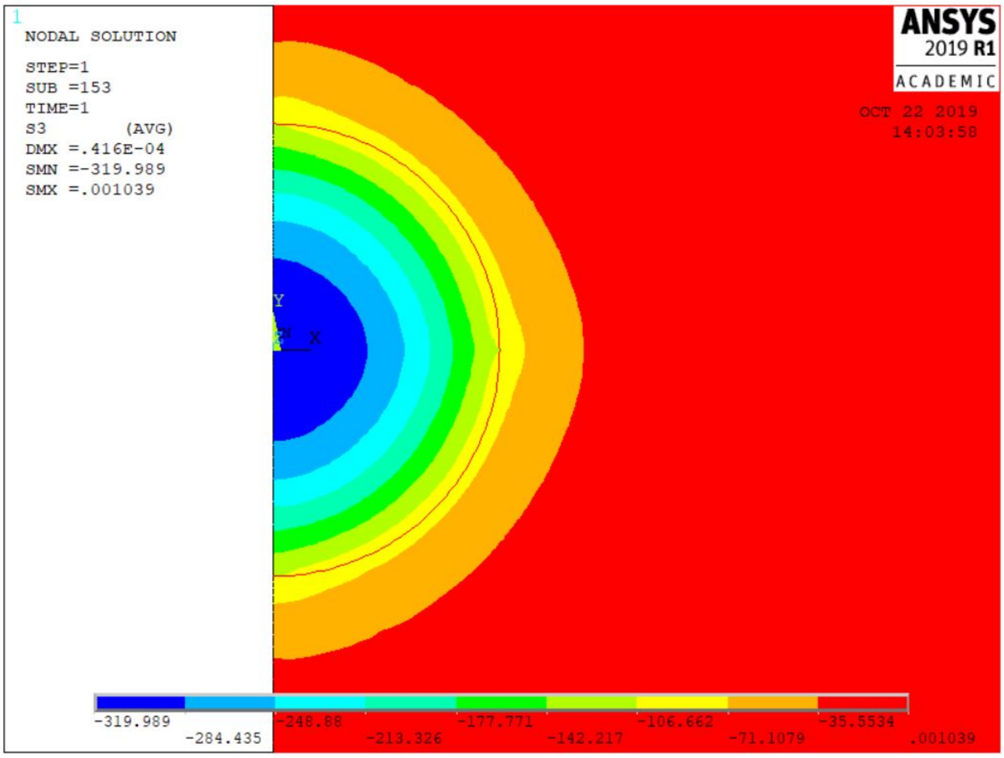

Figure 3.43: Radial stress field within the sphere and the deformable constraint in extraction condition

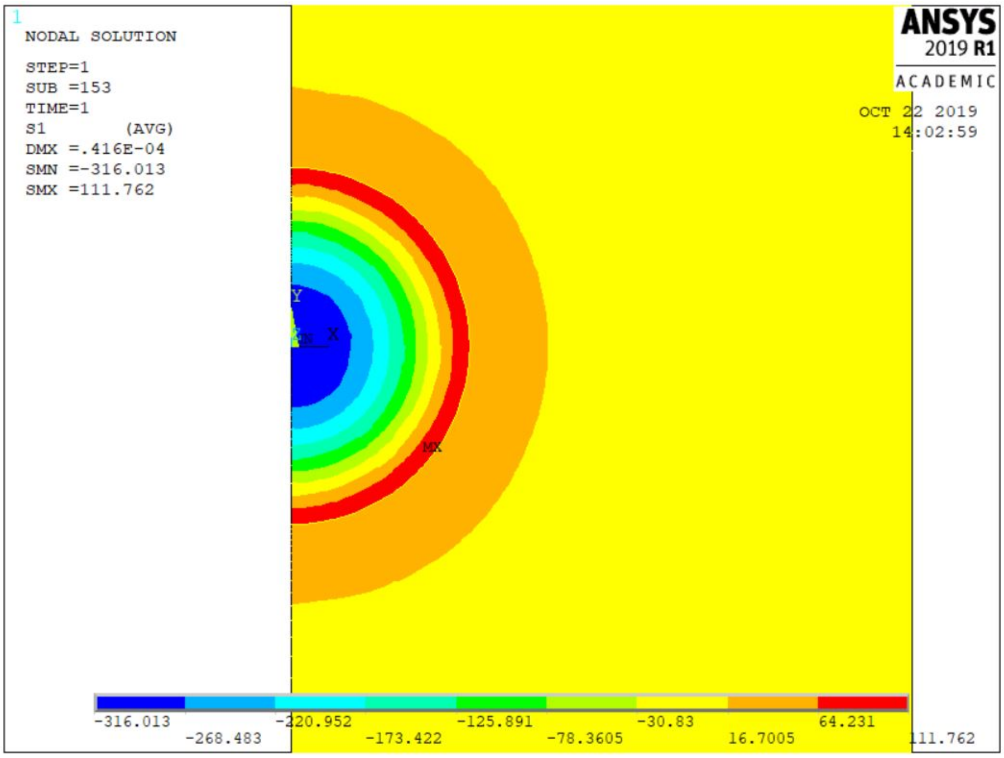

Figure 3.44: Hoop stress field within the sphere and the deformable constraint in extraction condition

Referring to figures 3.43-3.44, the stresses which arises in extraction are slightly translated towards the compressive one. However a tensile hoop stress is still present in the particle surface, even if lower compared to the free surface operation. This could reduce the dirving force for crack propagation, as mentioned before.

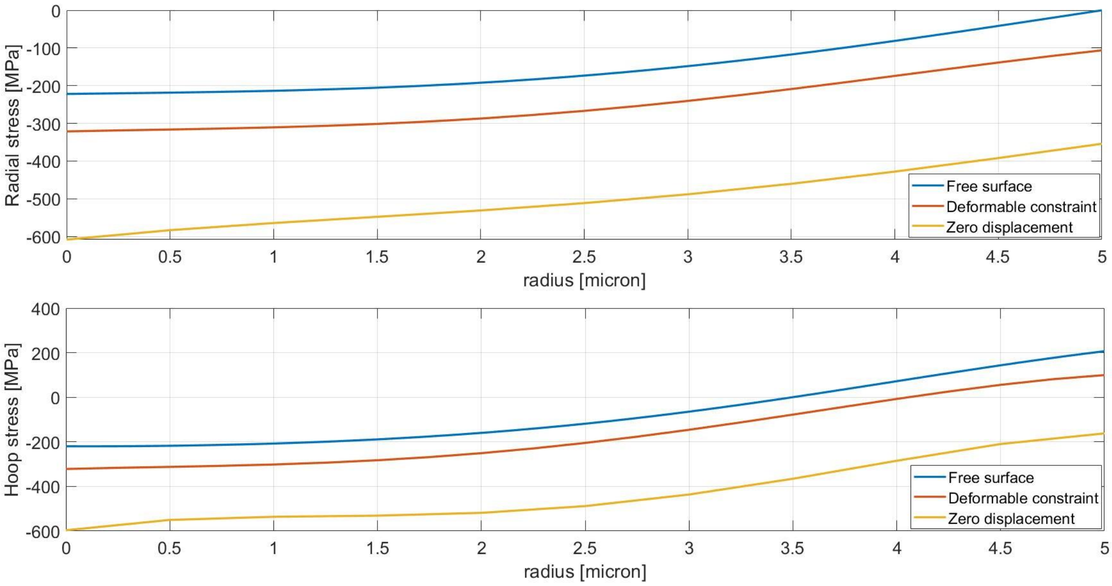

Figure 3.45: Stresses fields for free and deformable constraint totally constrained in extraction condition

figure 3.45 underlines that the "deformable constraint" model simulates a condition between the "free" and "totally constrained" model, and the latter is too strict and does not replicate faithfully the reality. These results are in line with the same model in insertion operation.

3.2.4 Dynamic model

A simple dynamic model is built in order to highlight the possible damaging effect induced by this type of load. The stresses which arise in a single particle subjected to the inertial force are studied. The acceleration used to compute the inertial force is the maximum value experienced by the cell. So, the peak acceleration, namely 2g, in the sinusoidal wave used in the experimental test is chosen as forcing.
The particle is modeled bonded to the current collector, so a reasonable area of contact, based on the previous contact analysis is assumed. This area is characterized by zero displacement in the model.
The sketch of the model is presented in figure 3.46.

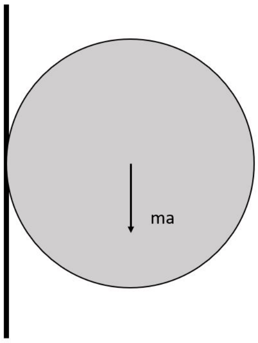

Figure 3.46: Sketch of the dynamic model

At this stage the stresses which arise with this configuration are studied. In figures 3.47 and 3.48 the equivalent and tangential stress are reported. The stresses are localized in the junction point between the particle and the current collector and the value are much lower compared to the stress due to intercalation/deintercalation.
The distribution of the stress suggests, as mentioned in [4], that this type of load could cause the loss contact between the current collector and the active material. Instead, it is less likely that this load concurs in the fracture propagation with the intercalation stresses, because the stress are really concentrated near the current collector.

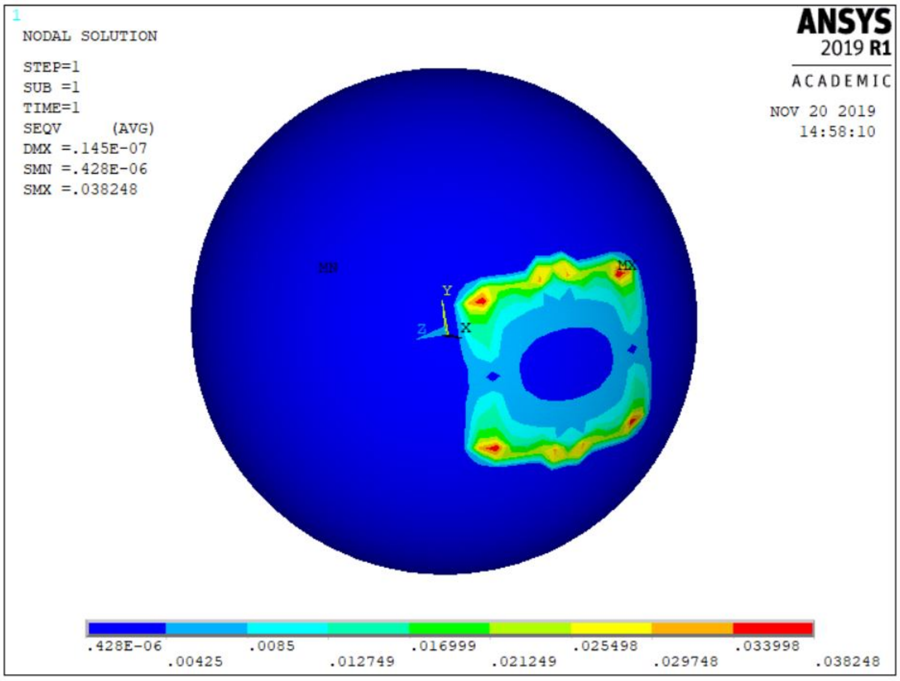

Figure 3.47: Equivalent stress due to dynamic load [MPa]

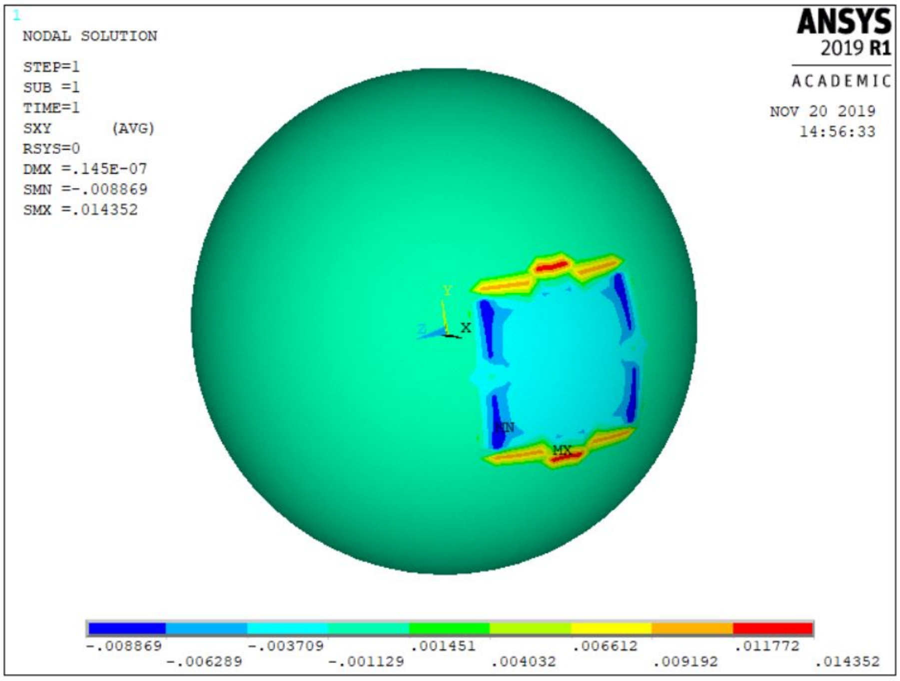

Figure 3.48: Tangential stress due to dynamic load [MPa]

Chapter 4

Experimental method

In this section the experimental method and the results of the dynamic tests carried out are presented.

It has been chosen to set up some experimental tests that could clearly highlight the damaging effects of vibration loads on lithium-ion cells, aware of the results obtained from other researchers [8-12] for what concerns the effects of dynamic load on the performances of lithium-ion batteries.

In particular it has been tried to enhance the knowledge about how the capacity decreases as a function of the number of cycles, since the current published works do not highlight clearly this dependence. In fact all the published researches, as far as the author knows, use a random excitation with variable frequency and intensity, which does not clearly highlight the damaging mechanism. Furthermore inconsistent results were found among the different works.

4.1 Damaging hypothesis

An increasing capacity fade, due to the increase of damage, was expected according to the fatiguing nature of vibration loads. However, there are no evidences about the relationship between capacity and cycles, as reported in figure 4.1 (left), namely if there is a linear trend, a sudden drop after few cycles, asymptotes, etc. If the mentioned phenomenon is verified, a Wöhler type dependence is supposed to be found between the amplitude of the acceleration, expressed in g, and the number of sinusoidal cycles which give the same level of damage, detected by the capacity fade. This concept is explained in figure 4.1 (right). Several test with different acceleration amplitudes should be performed in order to verify this hypothesis.

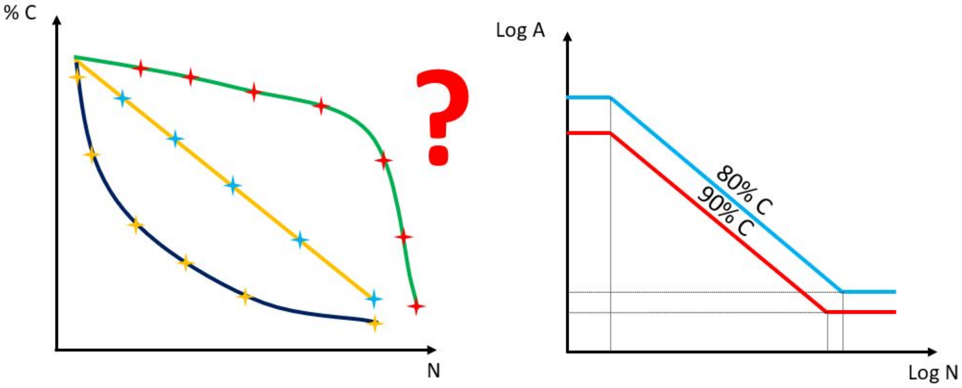

Figure 4.1: SRS and FDS calculation process [19]

4.2 Test parameters

In [9,14] the authors performed a random vibration load which should represent the real shocks which a car should suffer in the whole life. This was made driving a test car over a set of encoded road surfaces and recording the associated acceleration signal. The shock response spectrum (SRS) is extracted from the acceleration signal, plotting the values of maximum acceleration amplitude associated to each frequency, according to the procedure reported in figure 4.2.

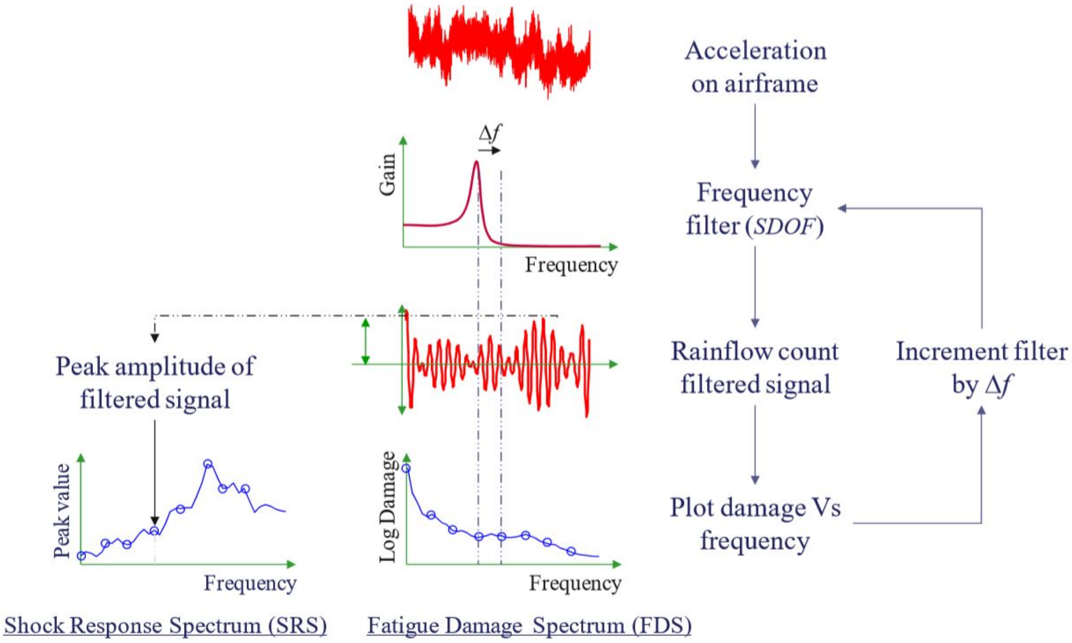

Figure 4.2: SRS and FDS calculation process [19]

The Millbrook standard codes the mean length of the distance traveled over each surfaces in the whole car life, for a mean use of an European citizen. Therefore the acceleration signal experienced by the car through the whole life was assembled repeating the recorded signal several time, in order to accumulate the distance prescribed by the Millbrook durability test framework.

At this stage the fatigue damage spectrum (FDS) relating to the whole car life was derived from the assembled acceleration signal according to figure 4.2.
Then a signal with the same damage level (same FDS) but shortened in time was computed, in order to contract the time required for the test, keeping the same level of damage, without exceeding the peak amplitude of the SRS got from the recorded signal.

Instead, in this work a basic approach is chosen to follow, in order to describe the damaging effects of vibrations, since the interest is focused in describing the damaging mechanisms rather than predicting the reduction of battery parameters at the end of life.
Thus a simple sine excitation and cycle counting was adopted, rather than a random load which pretends to simulate real load condition. In this way damage can be correlate directly with cycles, and a mathematical model which describes this phenomenon can be deduce.

10 and 20 Hz was chosen as vibration frequency, aware of the studies presented in [9,14] which explain that the most damaging frequencies provided by the car are about 5-30 Hz, as showed by the fatigue damage spectrum in figure 4.3-4.4.

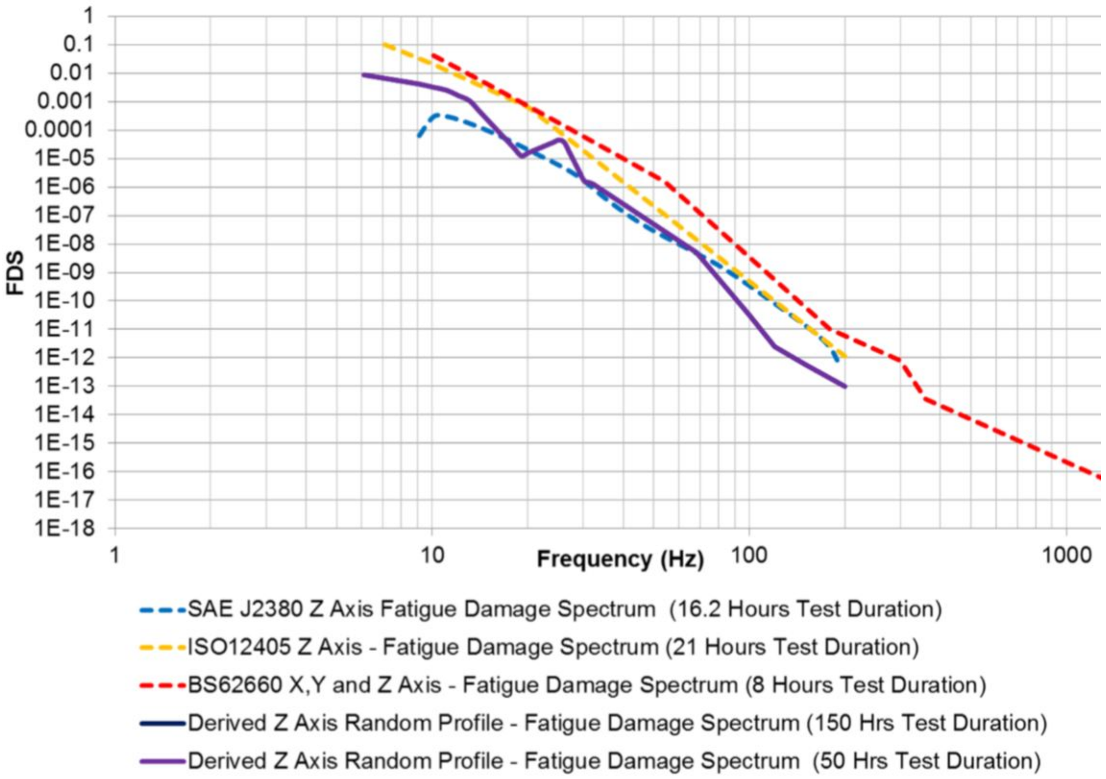

Figure 4.3: Fatigue response spectrum obtained in [9]

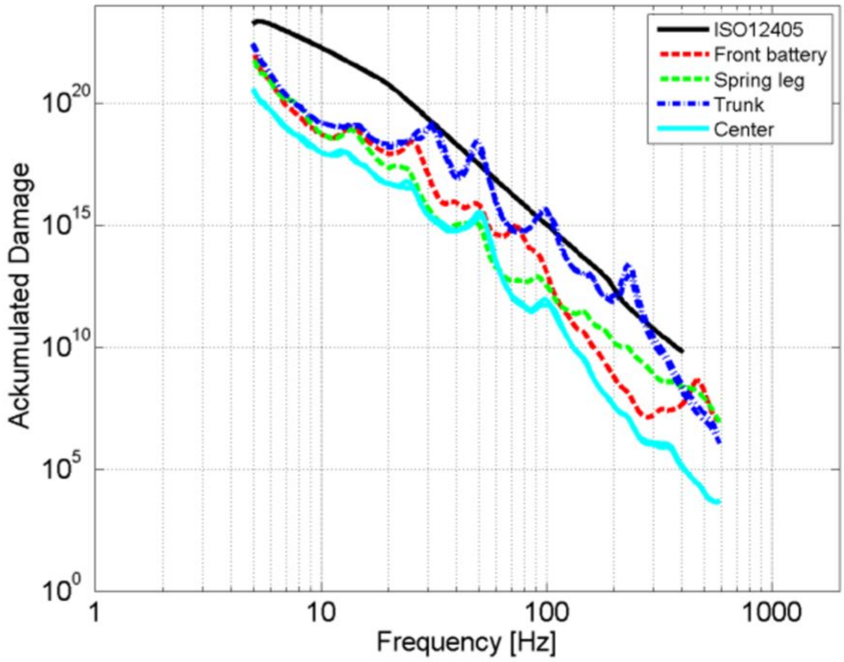

Figure 4.4: Fatigue response spectrum obtained in [14]

The acceleration amplitude of the sinusoidal load is chosen taking into consideration the results of the shock response spectrum (SRS) presented in [9,14] and reported in figure 4.5-4.6 and the acceleration signal recorded on a heavy duty machine during a step test.

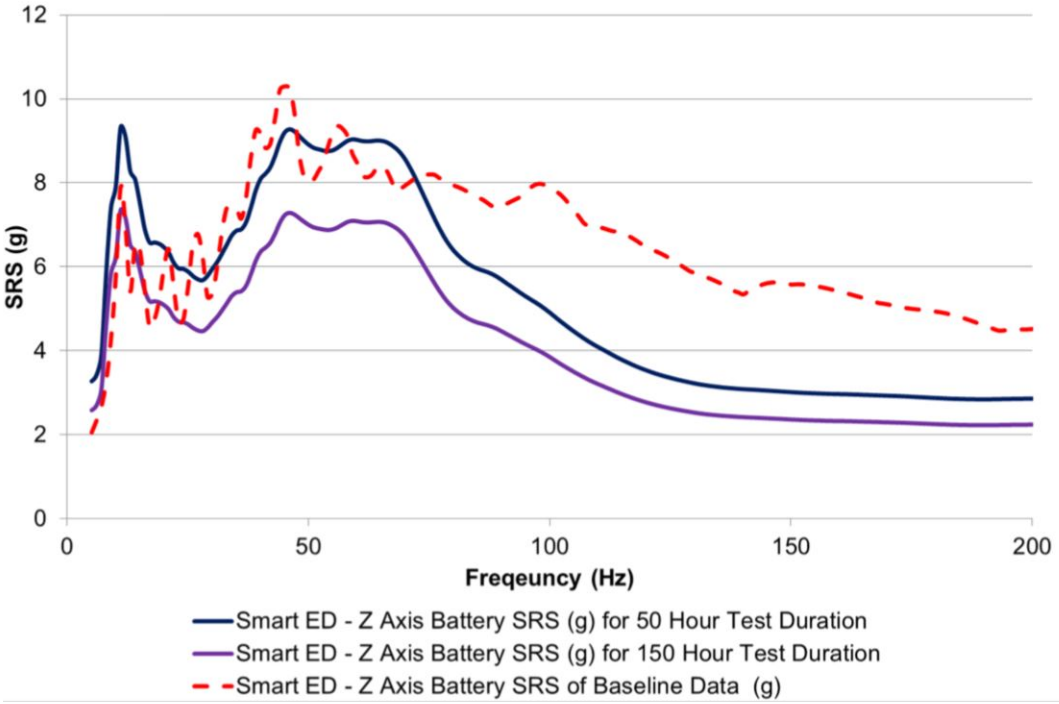

Figure 4.5: Shock response spectrum obtained in [9]

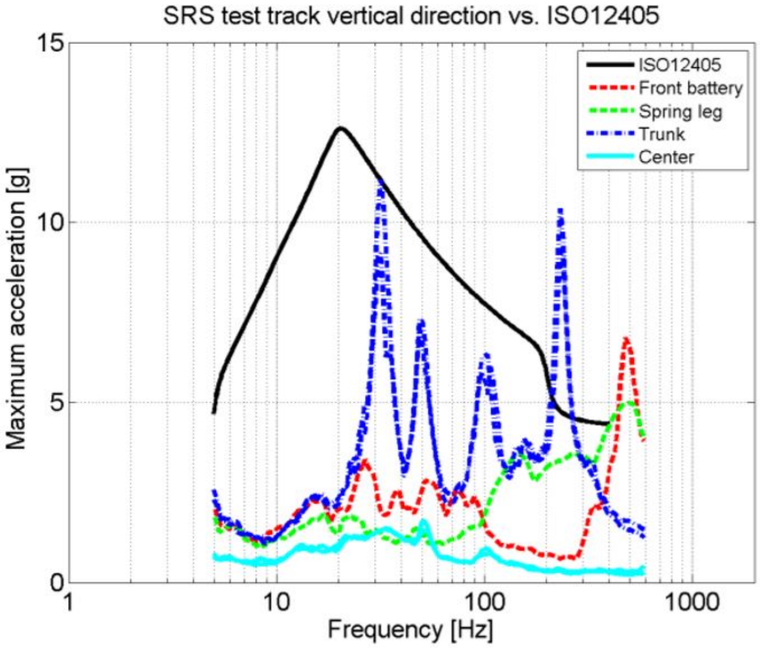

Figure 4.6: Shock response spectrum obtained in [14]

The signal reported in figure 4.7 shows the acceleration amplitude experienced by an heavy duty vehicle during a step test. The vehicle was driven over two step 3 cm high placed at a distant of 10m at 4 different velocities: 10 km/h, 20km/h, 28Km/h and 31 Km/h.
The Psd of the acceleration response to a step is computed in order to analyze the energy contribution at different frequencies. The maximum frequency considered is 25Hz since the signal was sampled at 50Hz.

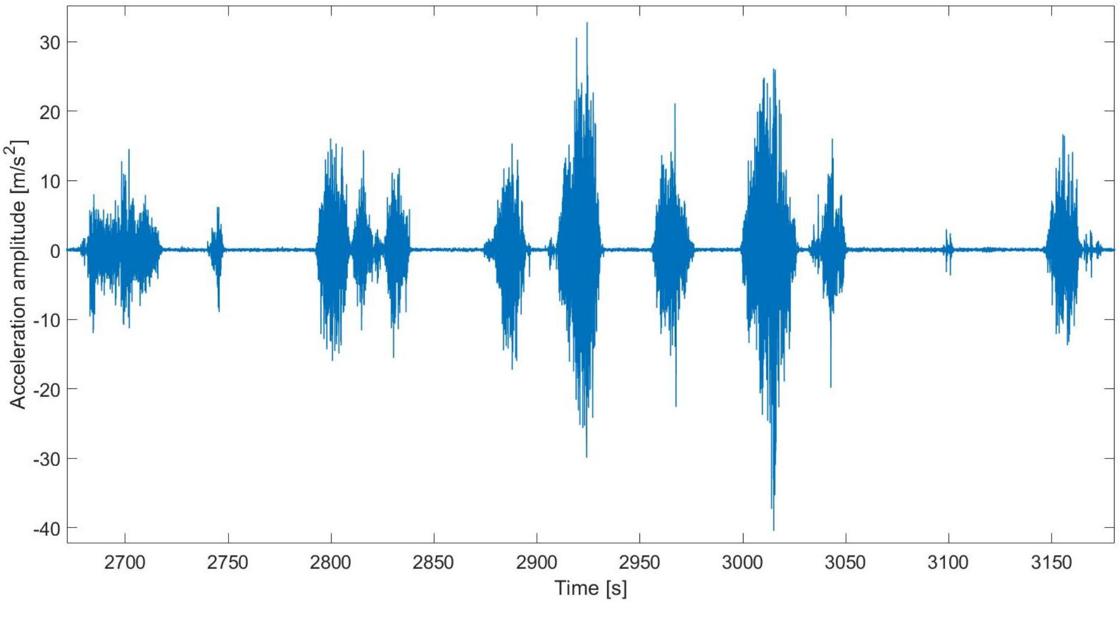

Figure 4.7: Acceleration signal in time domain

The PSD was computed in matlab with *pwelch* command, which computes

the power spectral density of the signal according to the Welch's periodogram method with the desired window, overlap, number of spectral lines and sampling frequency.
The selected signal has 1151 samples and is windowed with an Hanning window length 95 samples. The adopted window length allows to divide the signal in eleven realizations which are overlapped by 50%.

The coherent and noise gain of the window is defined as [28]:

$$\begin{aligned} CG &= \frac{1}{N}\sum_{i=0}^{N-1} w[i] \\ NG &= \frac{1}{N}\sum_{i=0}^{N-1} w[i]^2 \end{aligned} \tag{4.1}$$

Then according to this definition, the amplitude of the PSD expressed in terms of m/s^2 is reported in equation 4.2 [28] and plotted in figure 4.8.

$$A = PSD\frac{NG\Delta f}{CG^2} \tag{4.2}$$

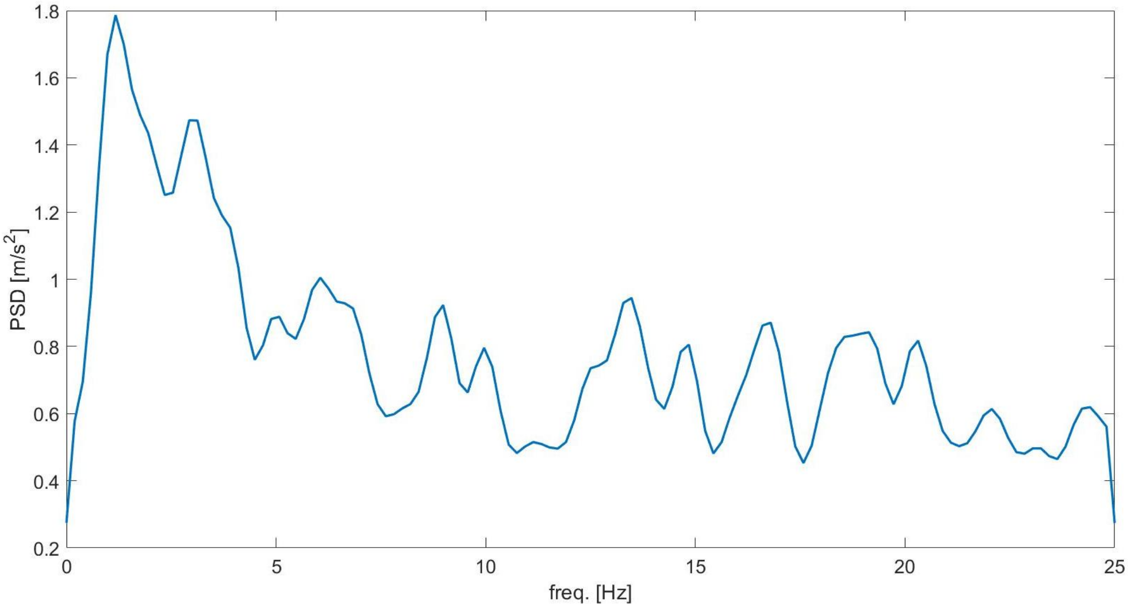

Figure 4.8: Power spectral density of the acceleration response

According to this analysis the amplitude chosen is $2g$, which allows to accumulate a greater damage in shorter time without exceed the acceleration peaks experienced in real life.

It is to highlight that the acceleration and frequency chosen are just first attempt values. For this reason it is necessary to perform other tests to explore the capacity behavior at different acceleration rate. It is expected that the greater the acceleration, the greater the capacity reduction.

For what concerns the frequency, it is expected that as long as the tests are carried out at frequency rate that is much lower than the first natural frequency, it does not influence the result. The frequency is not supposed to be a key factor in this study since the resonance frequency of the cell is related to values at which the car transmits with lower energy, i.e. over 100Hz.
No natural frequency identification of prismatic cell was found in literature, however the first natural frequency of prismatic cell can be assumed greater than 100 Hz from the dynamic studies presented in [10-11,16]. Several tests with variable frequencies should carried out in order to assess this hypothesis.

4.2.1 Test programming

The first set of tests was carried testing the cell on the shaker for 8 hours during the day and performing three capacity tests during the night. The cell was totally discharged during the test on the shaker, since this is the safer condition to carry out the test. Six tests on the shaker were performed, for a total of 2168700 cycles.

A second set of test was carried out on a different cell adding two safety controls on the temperature and on the voltage of the cell. The system shut down if the temperature is over 35 degrees and the voltage is lower than 2.7 V or greater than 3.5 V.
This controls allows to manage the tests over more days and nights, accumulating a greater number of cycles.

The testing method, sketched in figure 4.9, provides the alternation of a test on the shaker and a capacity test, which should detect the damage caused by the dynamic load. This test couple is repeated several times in order to describe how the capacity changes with cycles.

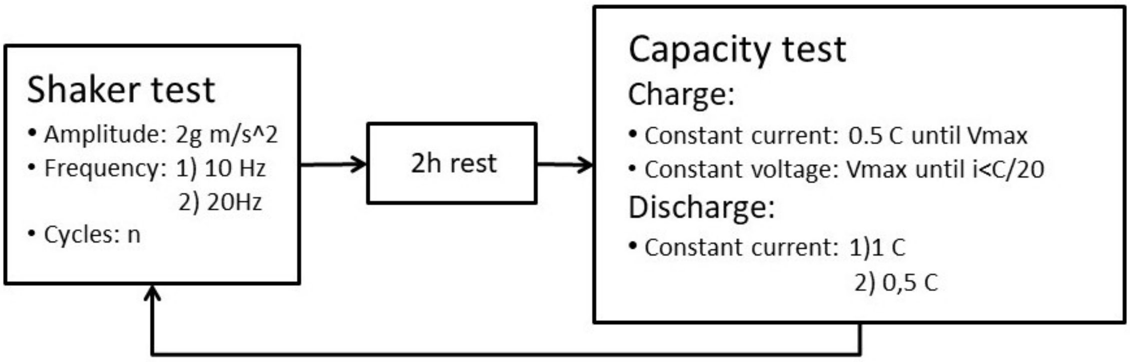

Figure 4.9: Sketch of the test method

4.3 Equipment

The shaker is a TiraVib 52110. The frequency range is 2-7000 Hz, the rated peak force is 100N, the maximum acceleration is 50g and the maximum displacement is 15mm.
The shaker is fed by a signal which is proportional to the voltage, higher the voltage higher the current which flows in the coils inside the shaker. Finally the current is proportional to the force that the shaker can exert on the sample. Then higher the acceleration supposed to be achieved, higher the force required to the shaker. The mass of the sample is the coefficient of proportionality, so the heavier the object the greater the force required.
The amplifier is BAA 120 made by Tira. It has a continuous sine output power of 120 VA. The input voltage has to be lower than 5V, and it can amplify until 22V.
A sketch of the testing equipment is reported in figure 4.11 and the real equipment is shown in figure 4.10.

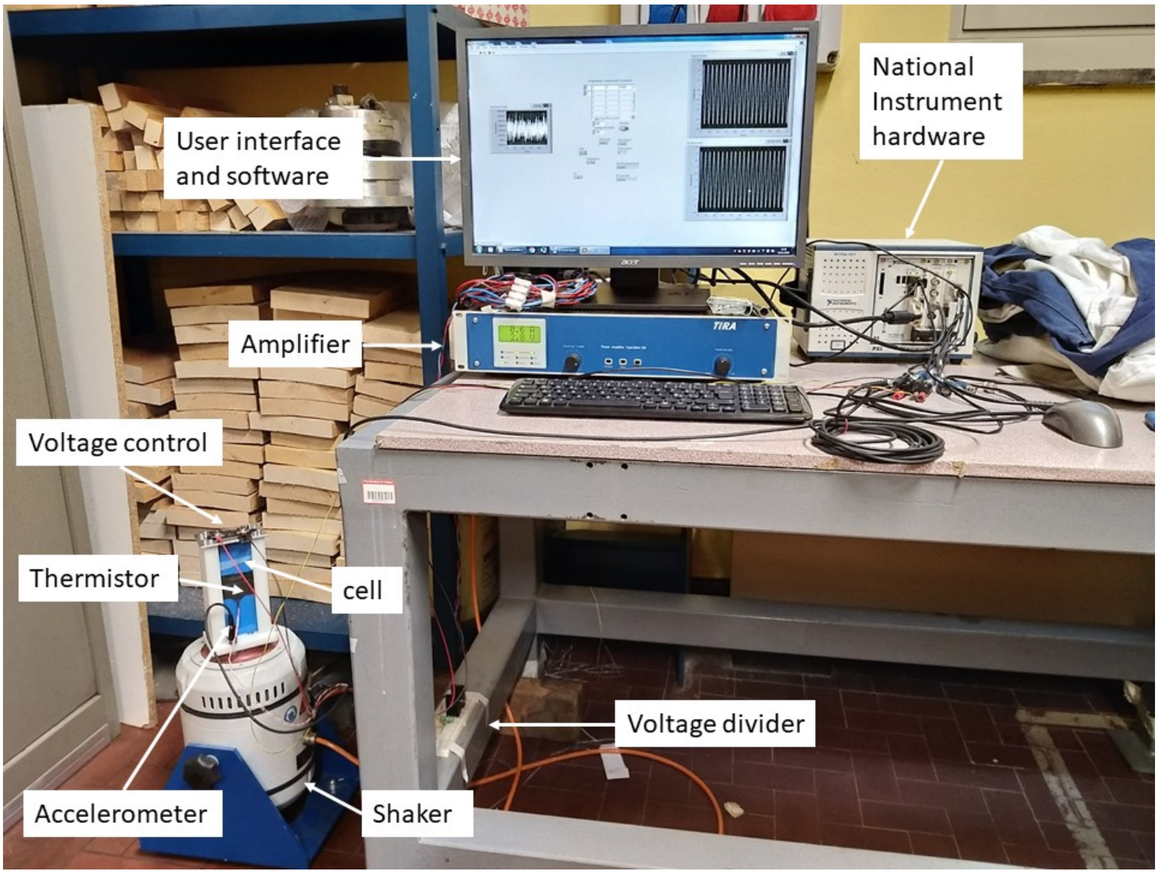

Figure 4.10: Test set up

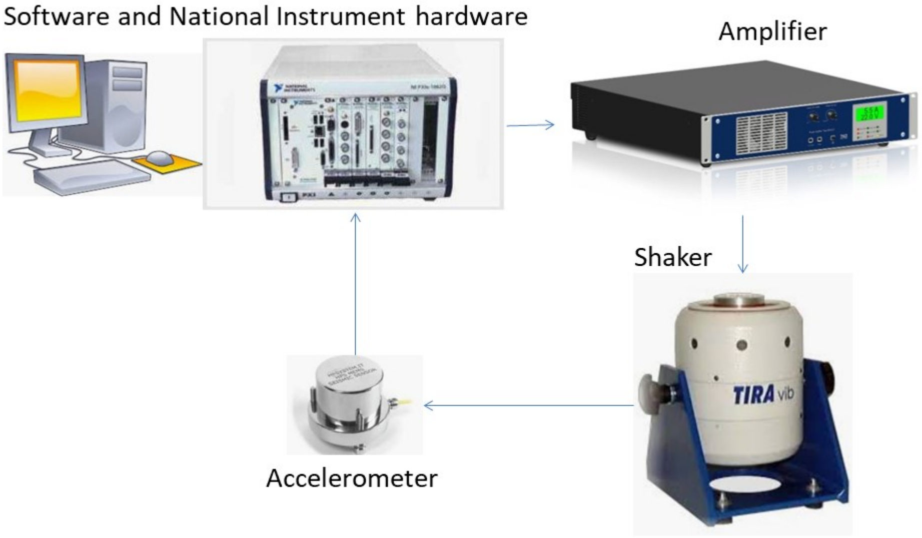

Figure 4.11: Sketch of the control

4.3.1 Shaker control

The system is completely controlled by National Instrument hardware, and the control is implemented in the software LaibView.
The system is controlled with a closed-loop logic, retro-acting the acceleration signal measured by the accelerometer fixed con the cell fixture. The target acceleration value is divided by the current acceleration value, in order to get a proper gain. So the target acceleration value is multiplied by the gain, and this equivalent value is used as maximum amplitude of the sinusoidal digital signal which is sent to the amplifier.
Thus the amplifier converts the digital signal to an analogue one, and sends it to the shaker. Also the amplifier has a gain that was set to one. If the output signal was greater than 5V this gain is set to a value which guarantees to reach the requested amplitude.
Then the accelerometer mounted on the cell holding fixture sends back the real acceleration signal to the National Instrument hardware.
A 5 seconds delay was imposed between every calculation of a new equivalent amplitude of the signal to send to the amplifier in order to get a stable system and to overcome the intrinsic delay of the system. The transitory before the gain calculation is not controlled, just the operating value is tuned.
The sketch of the block diagram implemented in LaibView is reported in figure 4.12.

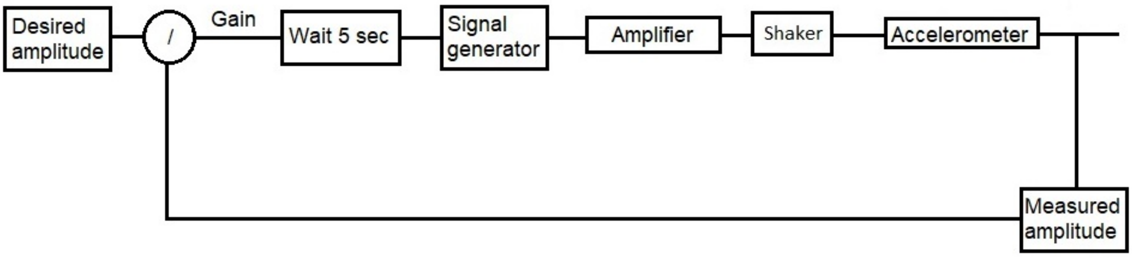

Figure 4.12: Sketch of the shaker block diagram

4.3.2 Capacity test

The capacity measurements are performed by the battery test system described in [27]. This system is equipped with two main power units: a charging unit and an electronic load. The power supply (QPX-600DP from AimTTi) allows to apply a predefined load to the battery according to the following control modes:

- Constant current mode (CC): the current extracted from the cell is kept constant despite the cell voltage varies.

- Constant voltage mode (CV): the terminal voltage is kept equal to the defined set point.

- Constant power mode (CP): A defined power set-point is matched regulating the current so that the product voltage per current is controlled.

- Constant resistance mode (CR): the load is regulated so that the sunk current is proportional to the applied voltage.

The charging process adopted in our tests is the CC-CV technique. This technique is suggested by the cell manufacturers and guarantees better performance in terms of capacity retention, even if requires a long charging time.
This technique consists of two steps: at first the cell is charged with a constant current rate equals to 0.5C until the maximum voltage is reached. In the second step the terminal voltage reached at the end of CC is kept constant until the current drops down below the threshold of C/20. Figure 4.13 shows the current and voltage values during CC/CV charging technique.

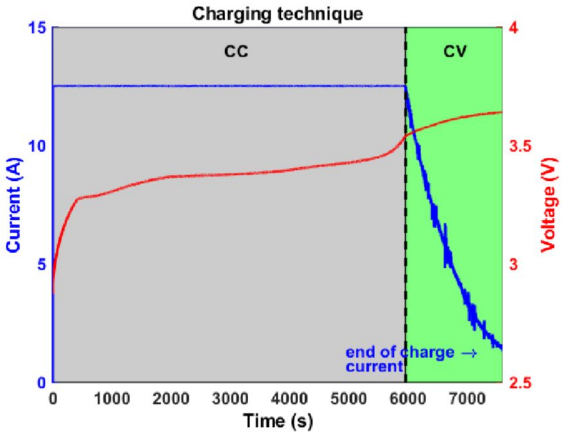

Figure 4.13: Constant current-constant voltage charging technique

The electronic load (Elektro-Automatik) is designed in order to apply a certain discharge profile to the cell, mainly tuning the current value. The discharge technique is simpler than the charging one and consists in just applying the desired sunk current (1C or 0.5 C in our test) until the voltage drops down a specific threshold prescribed by the cell manufacturers.
The amount of charge extracted during discharge gives a good estimate of the cell capacity, and it is assumed as the reference one in our tests.
The layout of the testing system is reported in figure 4.14.

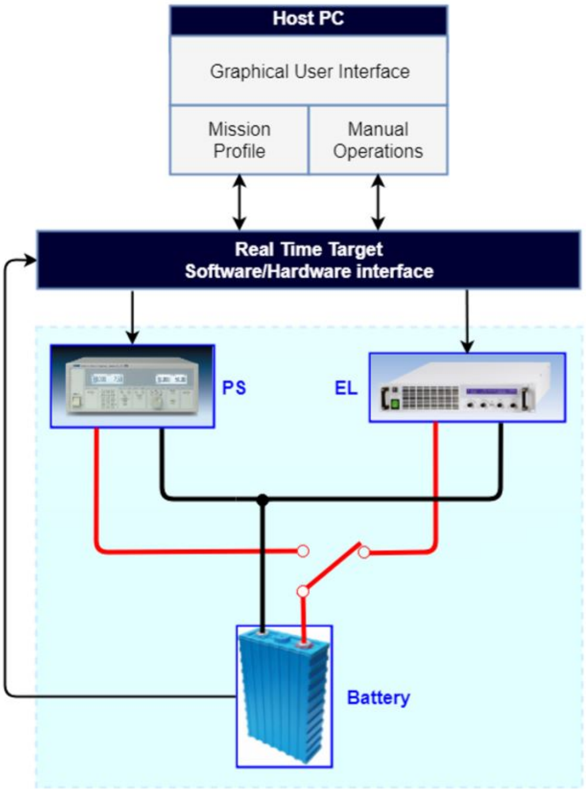

Figure 4.14: Testing system layout

The two power units are controlled by a multifunction I/O module (NI PXIe6363) from National Instruments. A software/hardware interface was developed within the NI LabVIEW environment and dialogue with the power units by means of a real time controller (NI PXIe 8840), which also acquires the data. Thus the user can interact with the system with a graphical user interface running on a personal computer. Voltage and current are continuously acquired and monitored by the data acquisition system, as well as the temperature by means of a thermistor.
The hardware/software interface has to execute some top levels functions such as:

- allow for manual or automatic settings
- import user defined load profile through data tables
- elaborate data to have useful signals for the power units
- execute safety protocols
- assign controls within determined timed intervals
- read measurements and save data on a log file

These functions are implemented in LabVIEW environment with two parallel while loops with different rates and execution priority, the producer loop and the consumer loop.
The first loop is the producer loop, shown in figure 4.15. It has the execution priority since it runs on the controller with deterministic time intervals in order to carry out safety shutdown procedures.

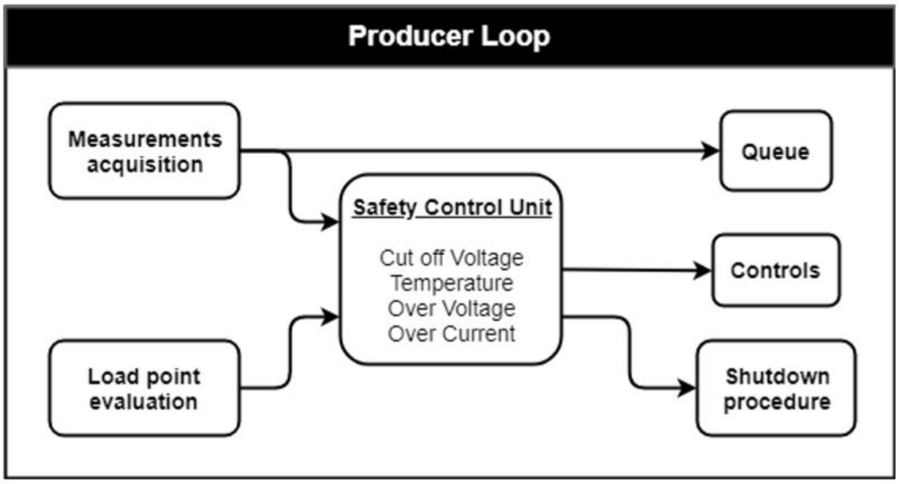

Figure 4.15: Producer loop

A designed module evaluates if the control variables and feedback measurements are in the safe operating range of the cell. A shut down procedure is immediately executed if these conditions are not satisfied. The defined set point values of electronic load and power supply, verified by the safety control unit, are assigned through the output Digital to Analog Converter of the NI PXIe 6363 module. Moreover, the data acquired by the analogue to digital converter of the

same multifunction module are organized and sent to a queque managed by the consumer loop.
The consumer loop mainly reads continuously the data from the queue in order to empty the dedicated memory and to allow further writings. Moreover it carries out an under-sampling of the data sent by the producer loop, since its sampling is too fast for the consumer loop and would create heavy log files.
Finally, a user friendly graphical interface, shown in figure 4.16, was developed in order to execute the following functions:

- upload a predefined load history
- define how many times the cycle must be repeated
- define the number of cycles to be executed
- have the main feedback measurements always available
- stop the running tests whenever needed

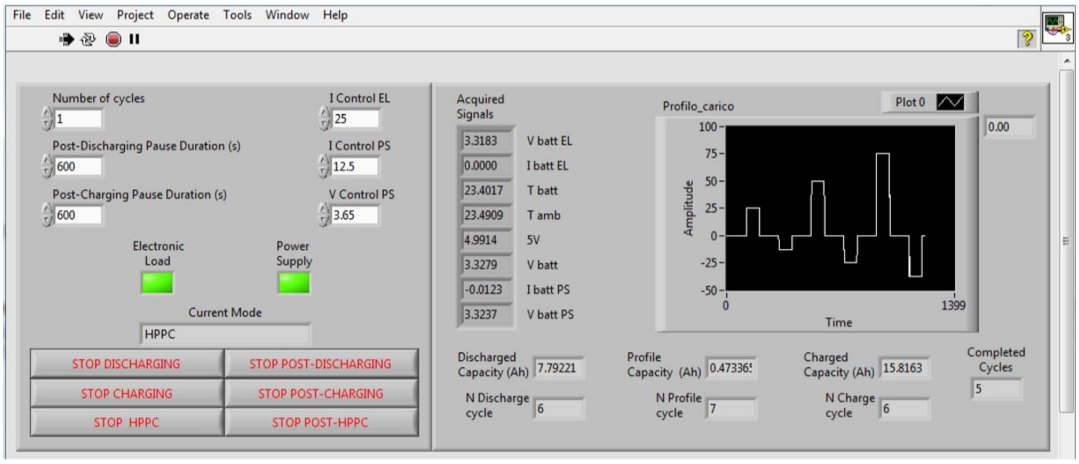

Number of cycles 1
Post-Discharging Pause Duration (s) 600
Post-Charging Pause Duration (s) 600
I Control EL 25
I Control PS 12.5
V Control PS 3.65
Current Mode HPPC
3.3183 V batt EL
0.0000 I batt EL
23.4017 T batt
23.4909 T amb
4.9914 5V
3.3279 V batt
-0.0123 I batt PS
3.3237 V batt PS
0.00
Discharged Capacity (Ah) 7.79221
N Discharge cycle 6
Profile Capacity (Ah) 0.47336
N Profile cycle 7
Charged Capacity (Ah) 15.8163
N Charge cycle 6
Completed Cycles 5

Figure 4.16: Graphical user interface implemented in LaibVIEW

The capacity tests were carried out simply charging and discharging the cell according to the modes described earlier, following the process reported in figure 4.17. The pause between every charge and discharge process allows a complete diffusion of the ions reaching an equilibrium condition. A complete equilibrium condition would require several hours, so a compromise between the quality of the results and the length of the test is adopted, choosing a resting time equal to 20 minutes. At least three capacity test were performed each time in order to have a sufficient statistical representation of the capacity value.

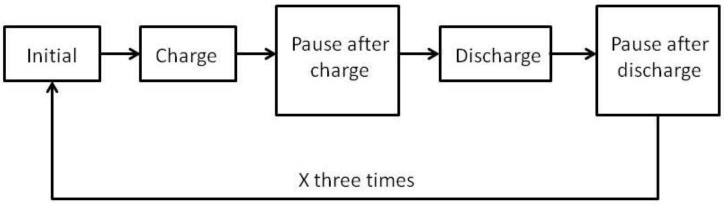

Figure 4.17: Sketch of the capacity test

4.3.3 Safety controls

The voltage was simply controlled acquiring the signal from the cell with one of the channel of the data acquisition. Its value is constantly monitored and a control added in LaibView block diagram makes the system shut down if it goes out from the prescribed range.

The temperature control was realized with a pt1000 thermistor whose resistance is $R_0 = 1000\Omega$ at $T_{ref} = 0°C$. A thermistor is a conductor whose resistance depends on the temperature with a known rule:

$$Pt = R_0[1 + \alpha(T - T_{ref})] \tag{4.3}$$

Where α is a coefficient which describe how the voltage changes with the temperature, and it is an intrinsic property of the material.

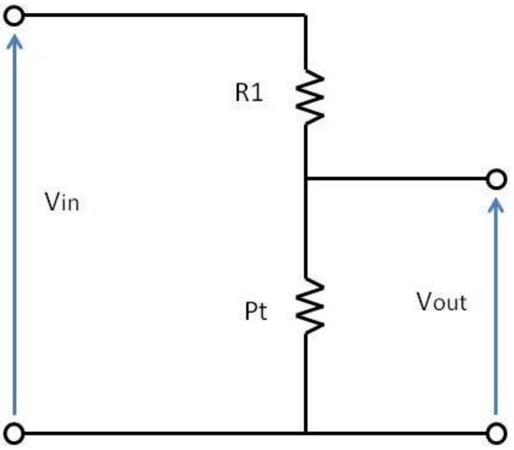

Figure 4.18: Sketch of the voltage divider

The output voltage of the voltage divider sketched in figure 4.18 is given by equation 4.4.

$$V_{out} = V_{in}\frac{Pt}{R_1 + Pt} \tag{4.4}$$

Then equation 4.3 and 4.4 are rearranged and solved for Pt:

$$\begin{cases} Pt = R_0[1 + \alpha(T - T_{ref})] & \text{from equation 4.3} \\ Pt = \frac{V_{out}}{V_{in} - V_{out}}R_1 & \text{from equation 4.4} \end{cases} \tag{4.5}$$

Finally the temperature as a function of the measured voltage is computed in equation 4.6

$$T = T_0 + \frac{1}{\alpha}\left(\frac{V_{out}}{V_{in} - V_{out}}\frac{R_1}{R_0} - 1\right) \tag{4.6}$$

The voltage divider, reported in figure 4.19, is powered by a 15V power supply (red and black wires). A voltage regulator is inserted in the circuit which lower the voltage to 5V, since the Nation Instrument can receive signal up to 10V. Moreover the voltage regulator commutes the AC from the power supply to DC which powers the thermistor. Then from the voltage regulator is extracted just the positive signal, which pass through the R_1 resistance and goes to the thermistor (small red and withe wire). The voltage difference induced by the thermistor is measured by the black and yellow wires, which brings the signal to the acquisition system.

Thus the voltage signal is converted in a temperature value by the software as shown by equation 4.6 and the system shut down if the computed values goes over 35°C.

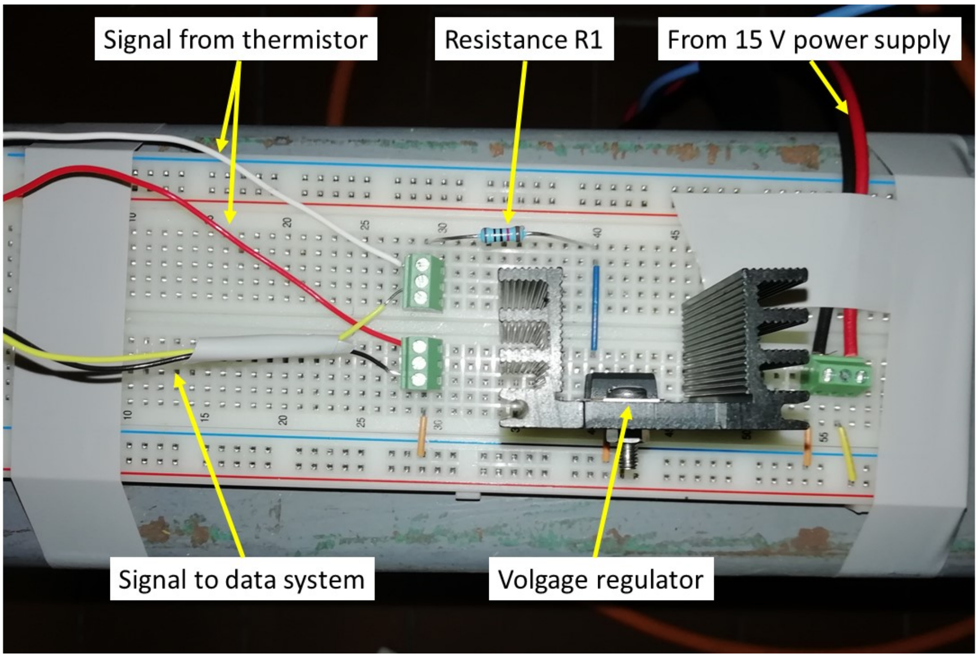

Figure 4.19: Voltage divider

4.4 Cell holding fixture

A cell holding fixture, shown in figure 4.20, was designed in order to support vibration testing. The cell is locked by a plate at the top of the structure, so it is constrained in vertical direction. Lateral displacements are locked by the L-shaped profiles, that however allow the lateral deformation, that could be induced by the discharge. A slot on the plate at the top of the structure allows to connect the electrodes with the National instrument hardware in order to acquire the voltage signal or to discharge/charge the cell.

The base and the L profiles are made of PVC, in order to reduce the weight of the entire structure, which would require a larger force to shaker. The top plate is made of aluminum, since it has to be 3mm thin in order to leave uncovered the electrodes, and quite rigid to ensure a good closure of the system as well. The inner slot is coated with insulating material in order to prevent the contact between positive and negative electrodes.

The holding fixture makes the cell excited in vertical direction. This is the most damaging condition according to several studies [8,11,12] and it corresponds to the real working condition.

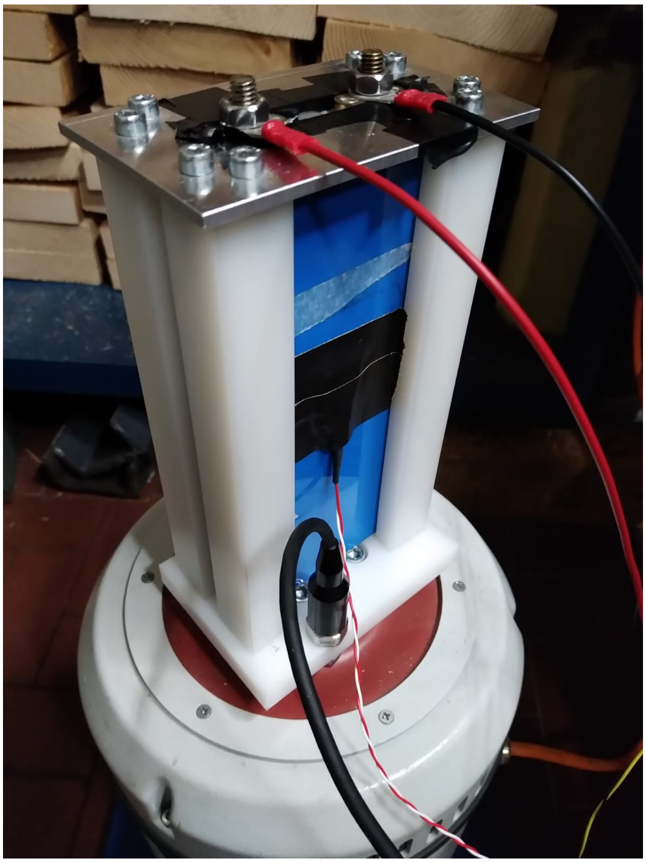

Figure 4.20: Cell holding fixture

Finally the cell characteristics are reported in table 4.1.

Table 4.1: Cell key manufacturer specifications

Specification	
Chemistry	LFP/C
Format	Prismatic
Dimensions	180 mm x 70 mm x 27 mm
Nominal capacity	25 Ah
Cut off voltage	2.0 V
End of charge voltage	3.65V
End of charge current	C/20
Max continuous discharging current	3C

4.5 Result from experimental test

The first test is the was the first ever vibrational test on lithium ion cell carried in the laboratory. For this reason, it was carried out just during the day, in order to supervise the cell, and a low number of cycles was achieved.
Before the vibrational test twelve capacity tests were performed in order to identify a reference capacity value. The capacity value associated to a specific number of cycles is the mean value computed from the several capacity tests performed

after each vibrational test.
The tests were not carried out in a climate chamber, so the influence of the temperature variation on the cell capacity is not negligible. For this reason, the results of the capacity tests, presented in figure 4.21 and 4.22, are correlated with the ambient temperature, in order to justify some sudden variations. It is specified that greater ambient temperature values result in greater capacity measurements.

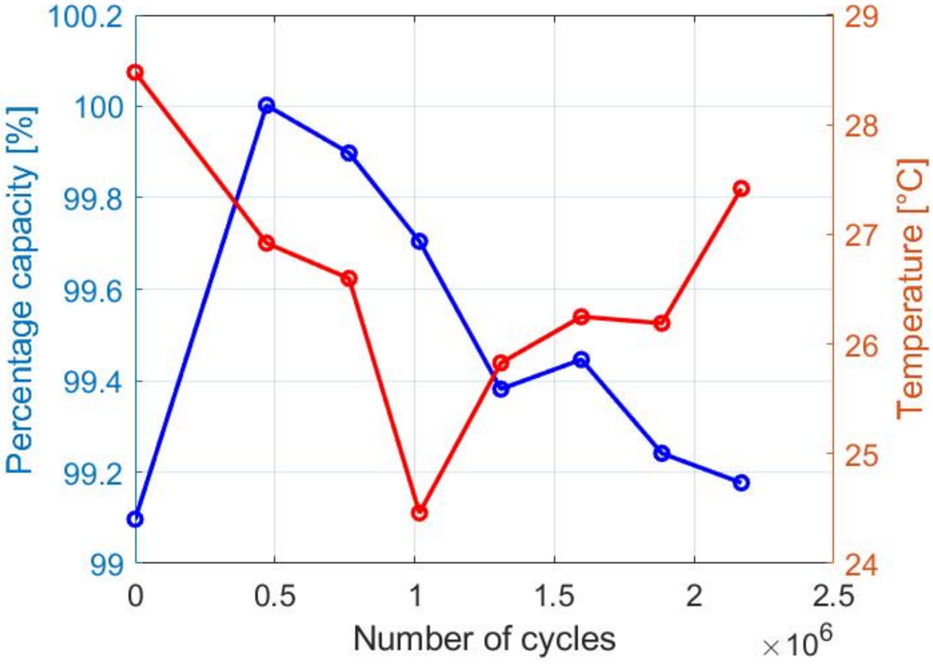

Figure 4.21: Results of the first vibrational test

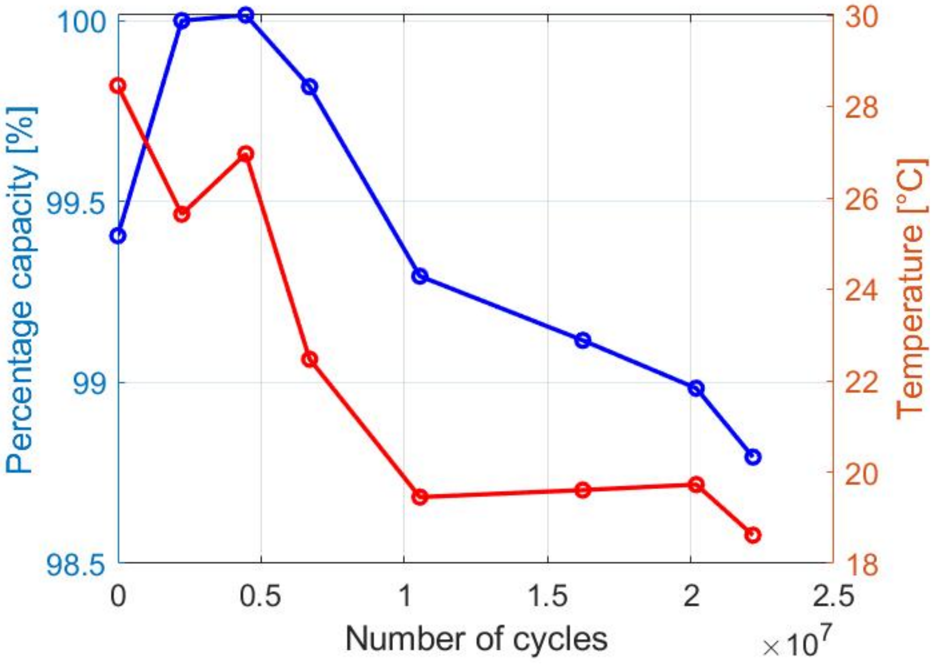

Figure 4.22: Results of the second vibrational test

In both the tests the first capacity measurement records an increase of about 0.6% respect to the capacity measurements carried out before the dynamic test. It was assumed that dynamic load breaks of the passivation layer over the active material, which otherwise should require several charge/discharge cycles to break down.
A slight reduction in the capacity measurements is detected in both the tests, regardless the temperature trend. The safe controls adopted in the second test allows to achieve more than twenty millions of cycles, with a capacity reduction of about 1.5%.
Other tests should be performed in order to explore how the capacity decreases with higher cycles number and different acceleration values.

Chapter 5

Conclusions

In this chapter the conclusions reached at the end of the work are summarized.

First of all the ageing mechanisms are explained through a deep literature review. A particular attention is given to those mechanisms which cause mechanical degradation and capacity fade, namely crack propagation in the particles of active materials and consequent SEI growth, loss of electric contact and loss of active material.

An analytical model which describes the stress in the active material particles due to litiation and delithiation is established. This model is a mechanical-diffusion coupled model, at first the two field are kept separated for sake of simplicity, then the coupled problem is solved. The uncoupled analytical model is derived with two simply boundary condition: totally free or totally constrained surface.
The stress rate computed in delitiation results in a compressive radial stress all over the particle, instead, the hoop stress results in a compressive stress in the core and a tensile stress in the surface. This last condition is the most dangerous for crack propagation. The stress rate in litiation is viceversa.
Finally the coupled model is solved via an iterative computation on the analytical solutions of the uncoupled model. The comparison between the two models shows that the uncoupled model is more severe than the coupled one. Indeed the hydrostatic stress acts as an artificial contribution to the diffusivity coefficient, allowing to reach an higher and flatter concentration profile in the particles. Consequently the concentration gradient is smoother and the stress level is lower.

A numerical model in Ansys APDL was carried out in order to validate the results derived by the uncoupled analytical model. A good agreement was achieved between analytical and numerical results.
Moreover the numerical model allowed to simulate more complex boundary conditions which take into account the interaction of the particle with the surroundings, namely the current collector or other particles.
This results in a drift of all the stress rate toward the compression. Future works should improve the simulation of the constraints of the particles and adopt the computed stress for crack propagation estimation.
For what concerns the dynamic load, a simply numerical model is established in order to highlight the effects of this type of load on the anode microstructure.

The effects of dynamic loads on Li-ion battery are still not clear and not studied enough in literature. The damaging effect of dynamic load is supposed to follow a Wöhler trend. Namely a progressive reduction of the acceleration amplitude with the increasing cycles number is supposed in order to keep the same level of damaging detected by capacity drop.
A set of experimental tests were carried out in order to deepen the knowledge about this topic. The dynamic loads were applied by a shaker according to dedicated studies in literature and to the analysis of experimental acceleration signals recorded by a heavy duty machine.
A sinusoidal mono-frequency acceleration was applied to the cell, and the trend of the capacity value as a function of sinusoidal cycles was studied. The results show a slight reduction in the cell capacity, about 1.5% after 20 milion of cycles. It will be necessary to perform longer tests at different amplitude values, in order to understand properly this topic in future works.

References

[1] Xia, L. Cao e G. Bi, «A review on battery thermal management in electric vehicle application» Journal of Power Sources, pp. 90-105, 2017.

[2] Q. Wang, B. Jiang, B. Li e Y. Yan, «A critical review of thermal management models and solutions of lithium-ion batteries for the development of pure electric vehicles,» Renewable and Sustainable Energy Reviews 64, pp. 106-128, 2016.

[3] M.A. Hannana, M.M. Hoqueb, A. Mohamedb, A. Ayobb, «Review of energy storage systems for electric vehicle applications: Issues and challenges», Renewable and Sustainable Energy Reviews 69 pp. 771–789, 2017.

[4] Christoph R. Birkl, Matthew R. Roberts, Euan McTurk, Peter G. Bruce, David A. Howey, «Degradation diagnostics for lithium ion cells», Journal of power Sources 341, pp. 373-386, 2017.

[5] Xuning Fenga, Minggao Ouyanga, Xiang Liu, Languang Lu, Yong Xia, Xiangming He, «Thermal runaway mechanism of lithium ion battery for electric vehicles: A review», Energy storage materials 10, pp. 246-267, 2018

[6] Pontus Svens, «Methods for Testing and Analyzing Lithium-Ion Battery Cells intended for Heavy-Duty Hybrid Electric Vehicles» Doctoral Thesis, KTH Royal Institute of Technology Applied Electrochemistry Department of Chemical Engineering and Technology,Stockholm, Sweden, 2014.

[7] J.Vetter, P.Novák, M.R.Wagner, C.Veit, K.-C.Möller, J.O.Besenhardb, M.Winterb, M.Wohlfahrt-Mehrens, C.Vogler, A.Hammouched, «Ageing Mechanisms in lithium-ion batteries», Journal of Power Sources, Volume 147, Issues 1–2, Pages 269-281, 9 September 2005.

[8] Lijun Zhang, Zhansheng Ning, Hui Peng, Zhongqiang Mu, Changyan Sun, «Effects of Vibration on the Electrical Performance of Lithium-Ion Cells Based on Mathematical Statistics», Applied sciences, 2017.

[9] J.M. Hooper,J. Marco, «Defining a Representative Vibration Durability Test for Electric Vehicle (EV) Rechargeable Energy Storage Systems (RESS)», World Electric Vehicle Journal Vol. 8

[10] James Michael Hooper, James Marco, Gael Henri Chouchelamane, Christopher Lyness, James Taylor, «Vibration Durability Testing of Nickel Cobalt Aluminum Oxide (NCA) Lithium-Ion 18650 Battery Cells», Energies, 2016.

[11] James Michael Hooper, James Marco, Gael Henri Chouchelamane, Julie Sylvie Chevalier, Darren Williams, «Multi-axis vibration durability testing of lithium ion 18650 NCA cylindrical cells», Journal of Energy storage 15, pp. 103-123, 2018.

[12] Martin j. Brand, Simon F. Schuster, Tobias Bach, Elena Fleder, Manfred Stelz, Simon Glaser, Jana Muller, Gerhard Sextl, Andreas Jossen, «Effects of vibrations and shocks on lithium-ion cells», Journal of power sources 288, pp. 62-69, 2015.

[13] Paweł J. Swornowski, «Destruction mechanism of the internal structure in Lithium-ionbatteries used in aviation industry», Energy 122 (2017) pp.779-786, 2017.

[14] Gunnar Kjell, Jenny Frodelius Lang, «Comparing different vibration tests proposed for li-ion batteries with vibration measurement in an electric vehicle», EVS27 Barcelona, Spain, November 17-20, 2013.

[15] Rutooj Deshpande, Mark Verbrugge, Yang-Tse Cheng, John Wang, and Ping Liuc, «Battery Cycle Life Prediction with Coupled Chemical Degradation and Fatigue Mechanics», Journal of The Electrochemical Society, 159 (10) A1730-A1738, 2012 .

[16] P.K. Ajeet Babu, U.S. Karle, M.R. Saraf, «Material Characterization and Analysis on the Effect of Vibration and Nail Penetration on Lithium ion Battery», 32nd Electric Vehicle Symposium (EVS32) Lyon, France, May 19 - 22, 2019.

[17] Xuning Fenga, Minggao Ouyanga, Xiang Liua, Languang Lua, Yong Xiaa, Xiangming He «Thermal runaway mechanism of lithium ion battery for electric vehicles: A review», Energy storage materials 10 pp. 246-267, 2018.

[18] Naoki Nitta, Feixiang Wu, Jung Tae Lee, Gleb Yushin «Li-ion battery materials: present and future», Materials today 18 pp. 252-264, 2015.

[19] Dr. Andrew Halfpenny, Chief Technologist, Mr. T. C. Walton, «New Techniques for Vibration Qualification of Vibrating Equipment on Aircraft», Aircraft Airworthiness & Sustainment 2010.

[20] Elham Kamali Heidari1, Ata Kamyabi-Gol, Mahmoud Heydarzadeh Sohi, Abolghasem Ataie, «Electrode Materials for Lithium Ion Batteries: A Review», Journal of Ultrafine Grained and Nanostructured Materials, Vol.51 pp1-12, 2018.

[21] Marc Doyle, Pankaj Arora, Ralph E. White «Capacity Fade Mechanisms and Side Reactions in Lithium-Ion Batteries», Faculty Publications, Department of Chemical Engineering, University of South Carolina, 1998.

[22] Yiling Dai, «Studying On Capacity Fade Mechanisms of Li-Ion Batteries Through Modeling», Theses and Dissertations, University of South Carolina, 2013.

[23] Fuqian Yang, «Interaction between diffusion and chemical stresses», Materials Science and Engineering: A, volume 409, p. 153 2005.

[24] Prof. Pietro Zecca, «Problemi al bordo per le Equazioni Differenziali», Note del corso di Analisi 3 UniFi

[25] Xiangchun Zhang, «Numerical simulation of intercalation induced stress in Li-Ion battery electrode particles», Journal of electrochemical society, 154 pp. A910-A916, 2007.

[26] Yang-Tse Cheng, Mark W. Verbrugge «Evolution of stress within a spherical insertion electrode particle under potentiostatic and galvanostatic operation», Journal of power sources 190, pp. 453-460, 2009.

[27] Elena Vergori, Francesco Mocera and Aurelio Somà «Battery Modelling and Simulation Using a Programmable Testing Equipment», Computers, 2018.

[28] W. L. Wang, Sanboh Lee, and J. R. Chen, «Effect of chemical stress on diffusion in a hollow cylinder», Journal of applied physics, 91, 9584, 2002.

[29] John Christensen, John Newman, «Stress generation and fracture in lithium insertion materials», Journal of Solid State Electrochemical, pp. 293-319, 2006.

[30] «Lithiation behavior of graphene-silicon composite as high performance anode for lithium-ion battery: A first principles study», Applied Surface Science 463, pp. 610-615, 2019.

[31] Lili Chai, et al. «Chitosan, a new and environmental benign electrode binder for use with graphite anode in lithium-ion batteries», Electrochimica Acta 105 pp.378–383, 2013.

[32] James Michael Hooper, James Marco, Gael Henri Chouchelamane and Christopher Lyness «Vibration Durability Testing of Nickel Manganese Cobalt Oxide (NMC) Lithium-Ion 18,650 Battery Cells», Energies, 2016.